# Fabrication of Critical-Angle Transmission Gratings for High Efficiency X-ray Spectroscopy

by

Minseung Ahn

Bachelor of Science in Mechanical and Aerospace Engineering
Seoul National University, February 1999

Master of Science in Mechanical Engineering
Massachusetts Institute of Technology, June 2005

Submitted to the Department of Mechanical Engineering
in partial fulfillment of the requirements for the degree of

Doctor of Philosophy in Mechanical Engineering

at the

MASSACHUSETTS INSTITUTE OF TECHNOLOGY



February 2009



Author .....
Department of Mechanical Engineering
January 15, 2009

Certified by .....
Mark L. Schattenburg
Senior Research Scientist
MIT Kavli Institute for Astrophysics and Space Research
Thesis Supervisor

Accepted by ..
David E. Hardt
Chairman, Department Committee on Graduate Students

# Fabrication of Critical-Angle Transmission Gratings for High Efficiency X-ray Spectroscopy

by

Minseung Ahn

Submitted to the Department of Mechanical Engineering
on January 15, 2009, in partial fulfillment of the
requirements for the degree of
Doctor of Philosophy in Mechanical Engineering

## Abstract

Diffraction gratings are fundamental optical elements that separate incident light into its constituent wavelength components. This dispersive feature of diffraction gratings has been broadly utilized in many applications including spectroscopy, microscopy, and interferometry. As high-energy electromagnetic waves, such as extreme ultraviolet (EUV) and x rays, are of interest in various science fields including astrophysics, fine pitch gratings with high diffraction efficiency are required. The critical angle transmission (CAT) grating has been devised to enhance diffraction efficiency of a transmission grating via reflection from the grating sidewalls. The shallow critical angle (1 - 2°) for total external reflection of incident x rays defines the geometry of the CAT grating and a consequent blazing condition. However, the geometrical requirements for the mirror-like grating bars with a very high aspect ratio are challenging to fabricate. The work presented in this thesis is about how to produce the CAT gratings by integrating many micro and nano-fabrication technologies. The fabrication process involves interference lithography for patterning fine pitch gratings and wet anisotropic etching on thin silicon membranes for straight and ultrahigh aspect-ratio ($\sim$ 150) freestanding structures. Potassium hydroxide (KOH) etching of the nanostructure is extensively investigated to improve etch anisotropy, uniformity, and process latitude. A stress-induced grating stiction problem during wet hydrofluoric acid (HF) release is analyzed using finite element modeling (FEM) of a thin grating plane between support structures on top of oxide in compressive stress. I successfully fabricated the CAT gratings with 574 and 200 nm periods, which were tested with synchrotron x rays with wavelengths ranging from 1 to 50 nm. The x-ray diffraction measurement showed the strong blazing effect in a non-zero diffraction order and the normalized diffraction efficiency was consistent with prediction by theory within 70 - 85%.

Thesis Supervisor: Mark L. Schattenburg
Title: Senior Research Scientist
MIT Kavli Institute for Astrophysics and Space Research

# Acknowledgments

First of all, I would like to thank my thesis advisor, Dr. Mark Schattenburg, for his guidance and support throughout my doctoral research. I am grateful to Mark for giving me the opportunity to work in the Space Nanotechnology Laboratory (SNL). When I joined the SNL in June 2005, I had just received my master's degree in a totally different research field, Haptics, which investigates human and machine interaction. The transition from Haptics to the nano-world was possible because Mark believed in my enthusiasm for nano-science and engineering even though I had no previous experience in microfabrication (I had not even seen a silicon wafer before joining the SNL). His experience, insight, and knowledge across diverse research areas were crucial in guiding the project in the right direction. When my research and fabrication processes seemed to come to a dead end, he always encouraged me with invaluable suggestions and discussions. He is an excellent advisor to work with because he closely and tirelessly interacts with his students throughout their projects.

My deepest thanks also go to Dr. Ralf Heilmann who originally devised the concept of the CAT grating. He not only taught me the principle of x-ray diffraction and the CAT grating idea but also conducted x-ray diffraction tests with my gratings providing experimental proof to complete my thesis. I appreciate his commitment to synchrotron measurement and analysis.

I want to thank the staff and students of the SNL as well. Robert Fleming provided technical support and trained me on the ion laser and reactive ion etching system. I remember that Dr. Yong Zhao spent a lot of time resolving a hardware problem in the Nanoruler DSP boards. He also initially trained me on the Nanoruler. Dr. Chih-Hao Chang and Dr. Mireille Akilian were very friendly and cheerful to chat and discuss with. I miss our "snack time" during the group meeting which they perfectly prepared every week. Having them as labmates made my research and life in the SNL a pleasure. I hope to see and meet with them again during commencement in June.

I would also like to thank all the staff and students of the Nanostructures Laboratory (NSL). Jim Daley is an excellent laboratory manager who expertly takes care of

most of the equipment and chemicals in the NSL. I appreciate his technical support and also the many favors that I asked of him. Mark Mandol helped me with the Raith programming for an imaging script to test the semi-automated focusing scheme. I thank the present and past tool adopters including Dr. Euclid Moon (AFM), Dr. Feng Zhang (Spinner), Dr. Will Arora (RIE), Tom O'Reilly (Lloyd's mirror), and Joel Yang (Asher).

Special thanks go out to all the staff of Microsystems Technology Laboratories (MTL) including Dave Terry (Evaporator and photolithography in TRL), Bob Bicchieri (VTR in ICL and RIE in TRL), and Kurt Broderick (Evaporator in EML). Their technical support was helpful in seamlessly integrating the fabrication processes.

I thank all friends and members of the KGSAME at MIT. In particular, I thank the ME fab guys, Dr. Soohyung Kim, Dr. Seok Chung, Wonjae Choi, and Hyun Jin In, for sharing and discussing their failure and success stories of their own fabrication processes. My war buddies in Starcraft, Dr. Jinho Jang, Jaewon Cha, Taeyoon Kim, made my 1500 winnings possible in the Battle.net. Jungik Kim and Hohyun Lee, who came to MIT with me in 2003, were good companions who struggled with me in the first few tough years.

I thank my parents in Korea for their lifetime of love, care, and support. They have always been supportive and proud of me even when I did not tell them exactly what I had been working on. Especially, I deeply thank my mother who ceaseless prays for me every moment of everyday. I cannot begin to express my gratitude to her.

Lastly and most importantly, I want to thank my beautiful wife, Minyoung, and lovely son Daniel for their love, sacrifice, and patience. I would not have accomplished this work without their unconditional support and endless encouragement. Daniel's smiles and cute actions are so adorable that I could forget all of the daily mental and physical fatigue that comes from fabbing.

This work was supported by NASA Grant No. NNX07AG98G, Kavli Instrumentation and Technology Development Fund, and a Samsung Scholarship.

# Contents

# List of Figures

# List of Tables

# Chapter 1

# Introduction

Spectroscopy is the study of the energy or wavelength composition (spectra) of electromagnetic waves. Measurement and analysis of the spectra of radiation provide invaluable information on matter to experimental scientists and engineers. A diffraction grating is a fundamental element in spectroscopy because it is able to separate incident light with multiple wavelengths into its constituent components as a function of wavelength. A diffraction grating is a periodic structure that has a comparable period to the wavelength of the incident light of interest. Ref. [1] is a good reference for diffraction gratings with a brief history. As high-energy electromagnetic waves such as x rays have been researched in various science fields including astrophysics, fine pitch (a few hundreds nanometer or less) gratings are required to disperse the incident lights with short wavelengths ($\sim$ 0.1 to 10 nm). While many types of diffraction gratings with different configurations and mounting schemes have been developed, they are generally classified into transmission gratings and reflection gratings. Motivated by technology goals for next-generation high-efficiency x-ray telescopes that NASA* plans to launch in about 10 years, the MIT Space Nanotechnology Laboratory (SNL) has developed a new type of soft x-ray ($\sim$ 1 to 10 nm wavelengths) diffraction grating combining advantages of the conventional transmission and reflection gratings [2]. This critical-angle transmission (CAT) grating is capable of significantly enhancing the diffraction efficiency while keeping transmission gratings' insensitivity

*National Aeronautics and Space Administration

to misalignment. The CAT grating design, however, requires straight and ultrahigh aspect-ratio free-standing structures with a period of few hundreds of nanometers. This thesis mostly presents microfabrication process development and integration to achieve the challenging geometry of the CAT grating. Successfully fabricated CAT gratings were tested with x rays at a synchrotron to experimentally prove the concept. The experimental results of soft x-ray diffraction through the CAT gratings matched with theory within about 80%. The peak diffraction efficiency also exceeded that of conventional transmission gratings by four to five fold.

## 1.1 Diffraction Gratings

Diffraction gratings are one dimensional (1D) periodic structure dispersing incident light into discrete orders as a function of wavelength ($\lambda$) and grating period ($p$). The diffracted beam directions or orders are given by the grating equation,

$$p\left(\sin\alpha + \sin\beta_m\right) = m\lambda, \tag{1.1}$$

where $m$ is the diffracted order, $\alpha$ is the incident angle, and $\beta$ is the diffraction angle. The sign convention for this equation and general geometry of a grating are shown in Fig. 1-1.

A diffraction efficiency of a grating is defined as the intensity ratio of a diffracted beam to the incident. For an amplitude grating (Fig. 1-2), where the grating bars are opaque, the intensity in the $m^{th}$ order, $I(m)$, can be calculated using scalar diffraction theory [3, 4]. A transmittance function $t(x)$ (Fig. 1-2(b)) of the normally incident beam can be written in a convolution of a rectangular function and delta function,

$$t(x) = \mathrm{rect}\left(\frac{x}{a}\right) \otimes \sum_{m=-\infty}^{\infty} \delta(x - mp), \tag{1.2}$$

where $\mathrm{rect}(x)$ is

$$\mathrm{rect}(x) = \begin{cases} 1 & |x| < 1/2 \\ 0 & \text{otherwise.} \end{cases} \tag{1.3}$$

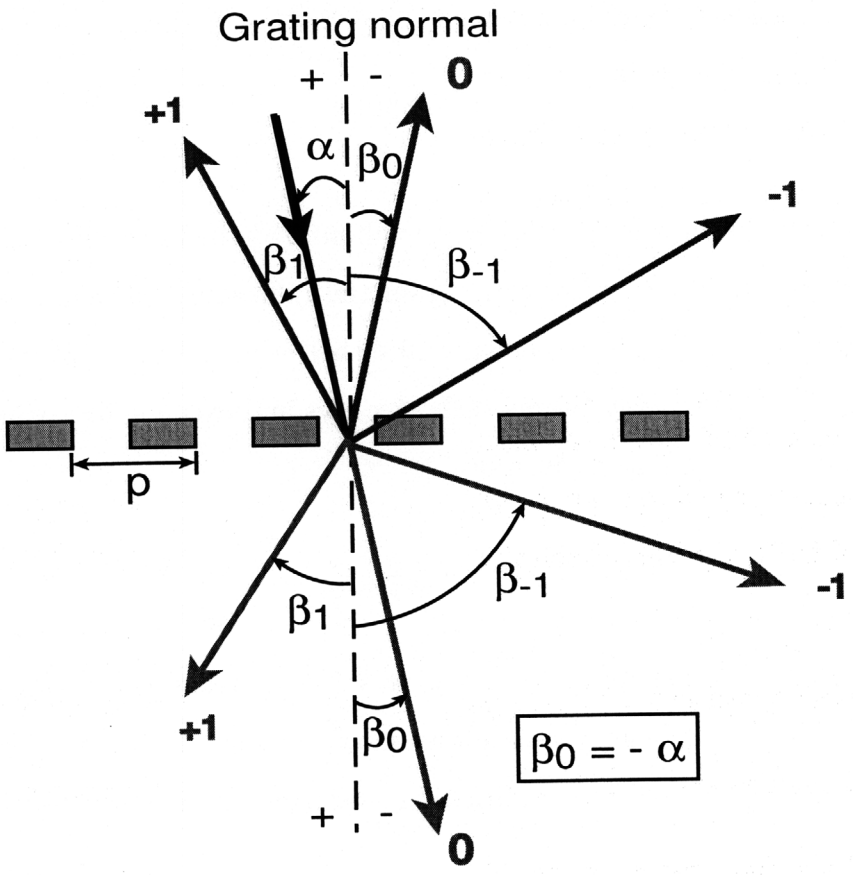


Figure 1-1: Sign convention for Eqn. (1.1). The angles $\alpha$ and $\beta_{\pm 1}$ are measured from the grating normal and the signs of the angle are on either side of the grating normal. The transmitted orders lies on the opposite side of the incident from the grating plane and the reflected order on the same side.

The field diffracted from the grating, $T(f_x)$, can be found by Fourier transform $\mathscr{F}\{\}$ of $t(x)$, and the diffraction intensity of the opaque grating is obtained by taking a square of $T(f_x)$, where $f_x$ is the x-direction spatial frequency.

$$T(f_x) = \mathscr{F}\{t(x)\} = \frac{a}{p}\,\mathrm{sinc}(af_x) \cdot \sum_{m=-\infty}^{\infty} \delta\left(f_x - \frac{m}{p}\right) \tag{1.4}$$

$$\left[\frac{I(m)}{I_0}\right]_{\text{opaque}} = \left(T\left(\frac{m}{p}\right)\right)^2 = \left(\frac{a}{p}\right)^2 \mathrm{sinc}^2\left[(a/p)m\right] = \left(\frac{a}{p}\right)^2 \left[\sin(m\pi a/p)/m\pi\right]^2, \tag{1.5}$$

where $I_0$ is the incident beam intensity and $\mathrm{sinc}(x)$ is

$$\mathrm{sinc}(x) = \frac{\sin(\pi x)}{\pi x}. \tag{1.6}$$

From Eqn. (1.5), the maximum efficiency is about 10% in the $\pm$ first order, when $a = p/2$. In the similar way, we can obtain the diffraction efficiency for a phase grating, where the grating bars partially absorb the incident beam and shift the phase as well. For high-energy beams such as x rays and extreme ultraviolet (EUV), the refractive index is complex, given by

$$n = 1 - \delta + i\beta, \tag{1.7}$$

where $\delta$ and $\beta$ are related to refraction and absorption, respectively. For the phase grating with the same geometry as the one shown in Fig. 1-2(a), thickness $t$, and refractive index $n = 1 - \delta + i\beta$, the diffraction efficiency for the $m^{th}$ order is given by,

$$\left[\frac{I(m)}{I_0}\right]_{\text{phase}} = \left[\frac{I(m)}{I_0}\right]_{\text{opaque}} \cdot \{1 + \exp(-2kt\beta) - 2\exp(-kt\beta)\cos(kt\delta)\}, \tag{1.8}$$

where $k = 2\pi/\lambda$. When $\delta >> \beta$, $t << 1/k\beta$, and $t = \lambda/2\delta$, the theoretical maximum diffraction efficiency of the phase grating reaches ~40% at the $\pm$ first order. However, it is under an unrealistic assumption of zero absorption [4].

Another class of diffraction gratings for x rays is the blazed reflection grating with a saw-tooth profile. A reflection grating with the rectangular profile concentrates most of the incident light into $0^{th}$ order, where all the wavelength components overlap. It is not desirable for spectroscopic purposes. The blazed reflection grating, however, redirects most of diffracted light to a particular non-zero order through specular reflection off of the saw-tooth facets. Figure 1-3 shows the configuration of a blazed reflection grating with the period $p$ and the facet angle $\gamma$. Most of the diffracted light goes to a particular direction (blazed order) satisfying the blazing condition in Eqn. (1.9), instead of spreading the diffracted beams evenly to $\pm$ orders with a central peak at $0^{th}$ order. The blazed order simultaneously satisfies the grating

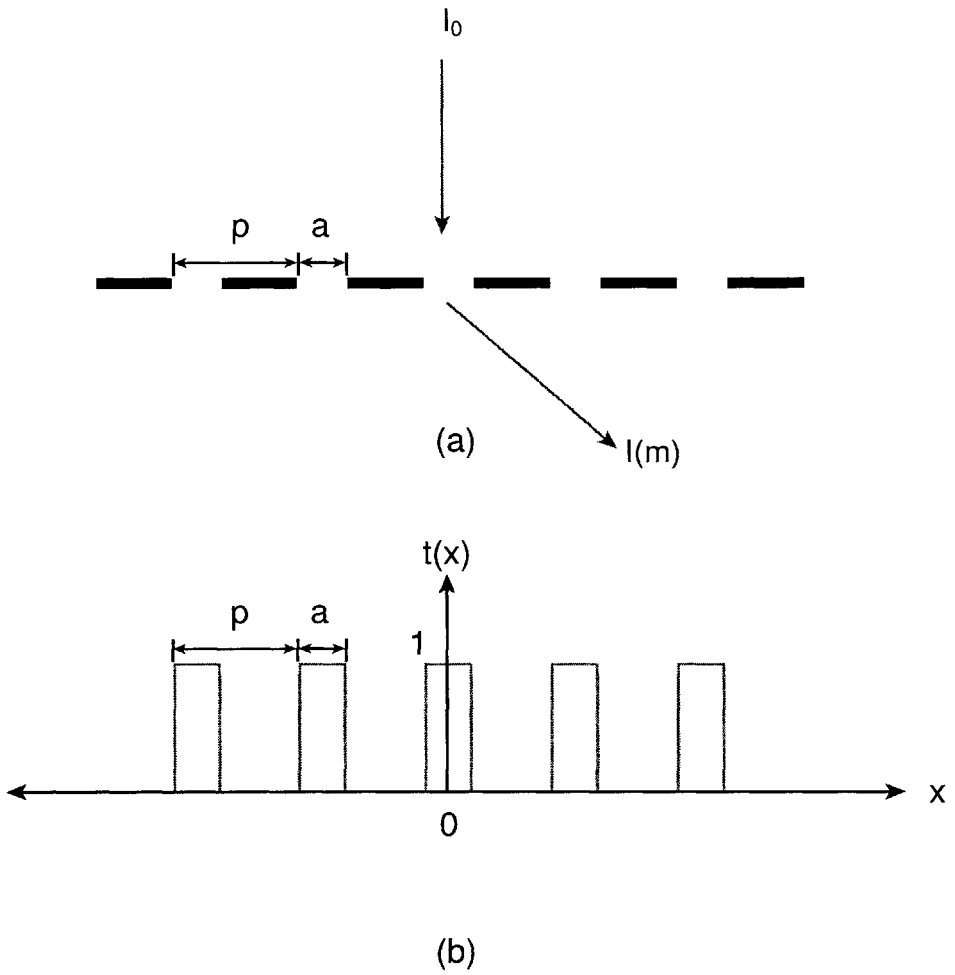


Figure 1-2: (a) An amplitude grating with period $p$ and open space width $a$. (b) Transmittance function $t(x)$ through the grating.

equation, Eqn. (1.1), and blazing condition, Eqn. (1.9). One can design the facet or blaze angle, $\gamma$, for the desired $\lambda$ and $m$. In general, the diffraction efficiency of blazed reflection gratings is higher than that of transmission gratings because most of the incident light is reflected and concentrated in the blazed order without too much absorption in the grating bars. A maximum diffraction efficiency about 70% is predicted for off-plane mounted grazing-incidence reflection gratings [5, 6], and up to 40% efficiency in a single order has been demonstrated [7–11].

$$\beta_{m\_blaze} = \alpha - 2\gamma \tag{1.9}$$

The diffraction efficiency of a blazed reflection grating can be calculated by the same

way as for the transmission grating. For a normal incident plane wave to the blazed grating shown in Fig. 1-3, the reflectance function $r(x)$ is, assuming unrealistic 100% reflectivity, given by

$$r(x) = \left[\text{rect}\left(\frac{x}{p}\right)\exp(-ik\frac{2d}{p}x)\right] \otimes \sum_{m=-\infty}^{\infty}\delta(x-mp), \tag{1.10}$$

where $k = 2\pi/\lambda$ in air. The Fraunhofer diffraction pattern is then found by the Fourier transform of $r(x)$,

$$\begin{aligned} R(f_x) = \mathscr{F}(r(x)) &= \text{sinc}(p(f_x + \frac{kd}{p\pi}))\cdot\sum_{m=-\infty}^{\infty}\delta(f_x - m/p) \\ &= \text{sinc}(m + kd/\pi) \\ &= \frac{\sin(m\pi + kd)}{m\pi + kd} = \frac{\sin kd\cos m\pi}{m\pi + kd}. \end{aligned} \tag{1.11}$$

Therefore, the diffraction efficiency for $m^{th}$ order is given by,

$$\left[\frac{I(m)}{I_0}\right]_{\text{blaze}} = \frac{\sin^2 kd}{(m\pi + kd)^2}. \tag{1.12}$$

When $kd = -m\pi$, the diffraction efficiency at $m^{th}$ order is maximized. In this example, the efficiency reaches 100% due to the unrealistic perfect reflection.

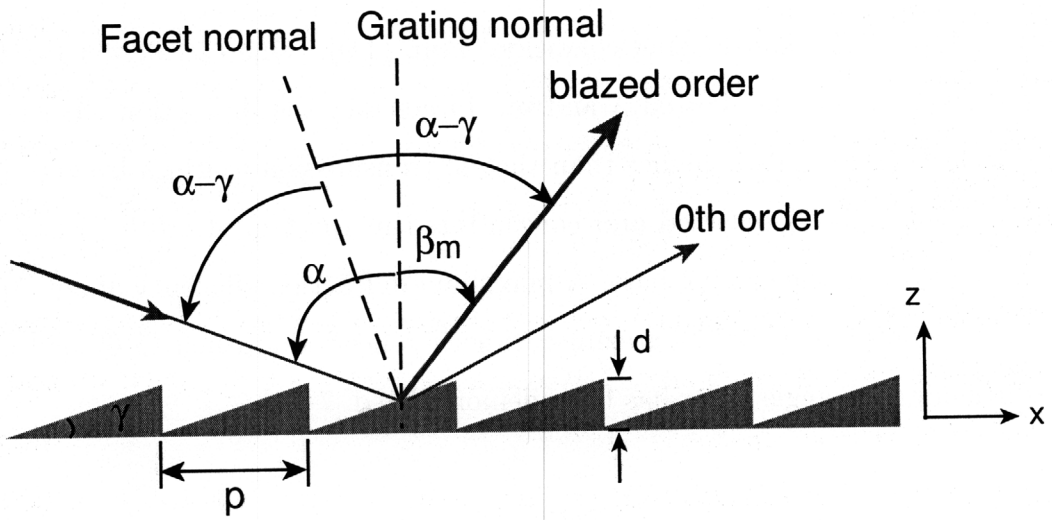


Figure 1-3: (a) An blazed reflection grating with period $p$ and blaze angle $\gamma$. For the right-triangular profile, $\tan\gamma = d/p$

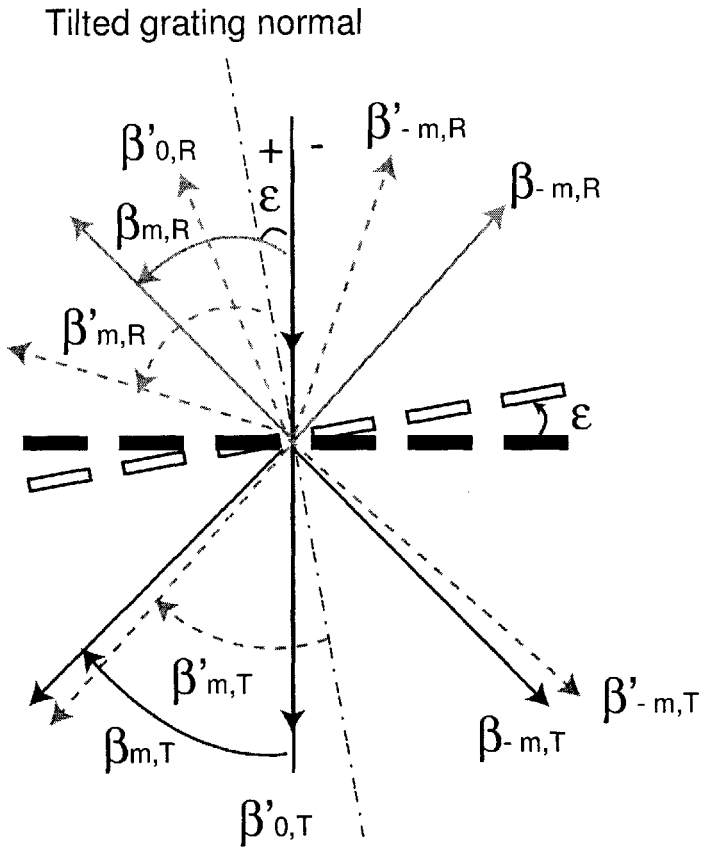


Figure 1-4: Alignment sensitivity of reflected and transmitted orders for the normal incidence case. Solid lines and dotted lines represent diffracted beams without and with misalignment angle $\varepsilon$, respectively.

However, a disadvantage of blazed reflection gratings for instrumentation is that they are much more sensitive to misalignment and grating surface figure errors than transmission gratings. Supposing there is a misalignment angle $\varepsilon$ ($<< 1$) as shown in Fig. 1-4, one can derive the approximate changes of the diffraction angles for the reflected and transmitted orders. For a normal incident case ($\alpha = 0$) without misalignment, the diffraction angle $\beta_m$ is determined by Eqn. (1.13). Similarly, for the grating surface tilted by angle $\varepsilon$, one can find the diffraction angle $\beta'_m$ from Eqn. (1.14).

$$\sin \beta_m = \frac{m\lambda}{p} \tag{1.13}$$

$$\sin\beta'_m = \frac{m\lambda}{p} + \sin\varepsilon \tag{1.14}$$

The Taylor expansion and first-order approximation of Eqns. (1.13) and (1.14) yield

$$\begin{aligned} \beta_m &= \arcsin\frac{m\lambda}{p} \\ &\simeq \frac{m\lambda}{p} + \frac{1}{6}\left(\frac{m\lambda}{p}\right)^3 \end{aligned} \tag{1.15}$$

and

$$\begin{aligned} \beta'_m &= \arcsin\left(\sin\varepsilon + \frac{m\lambda}{p}\right) \\ &\simeq \varepsilon + \frac{m\lambda}{p} + \frac{1}{2}\varepsilon\left(\frac{m\lambda}{p}\right)^2 + \frac{1}{6}\left(\frac{m\lambda}{p}\right)^3. \end{aligned} \tag{1.16}$$

From Eqns. (1.15) and (1.16) and taking the angle offset $\varepsilon$ into account, we obtain the angle changes for transmitted ($\Delta\beta_{m,\mathrm{T}}$) and reflected ($\Delta\beta_{m,\mathrm{R}}$) orders,

$$\begin{aligned} \Delta\beta_{m,\mathrm{T}} &= \left(\beta'_{m,\mathrm{T}} - \varepsilon\right) - \beta_{m,\mathrm{T}} \\ &\simeq \frac{1}{2}\varepsilon\left(\frac{m\lambda}{p}\right)^2, \end{aligned} \tag{1.17}$$

$$\begin{aligned} \Delta\beta_{m,\mathrm{R}} &= \left(\beta'_{m,\mathrm{R}} + \varepsilon\right) - \beta_{m,\mathrm{R}} \\ &\simeq 2\varepsilon + \frac{1}{2}\varepsilon\left(\frac{m\lambda}{p}\right)^2. \end{aligned} \tag{1.18}$$

Since the term $\frac{1}{2}\varepsilon\left(m\lambda/p\right)^2$ in the high-energy band is three to four orders of magnitude less than $2\varepsilon$ [2, 5], the reflected orders approximately rotate by $2\varepsilon$ in proportion to the misalignment angle, while angle shifts of the transmitted orders are negligible. Therefore, one of the advantages of transmission gratings over reflection gratings is the relaxed alignment and flatness tolerance, which is desirable for space instrumentation in terms of the cost and weight [2, 12].

When designing a grating, we also need to consider other factors such as angular dispersion and resolving power. The angular dispersion represents the diffraction angle change due to a small change of wavelength. One can derive the angular dispersion ($\frac{\partial \beta_m}{\partial \lambda}$) by differentiating Eqn. (1.1) [13], and obtain

$$\begin{aligned}
\frac{\partial \beta_m}{\partial \lambda} &= \frac{m}{p \cos \beta_m} \\
&= \frac{m}{p}\left(1 - \left(\frac{m\lambda}{p} - \sin\alpha\right)^2\right)^{-1/2} \\
&\simeq \frac{m}{p}\left(1 + \frac{1}{2}\left(\frac{m\lambda}{p}\right)^2\right) \quad \text{for } \alpha = 0 \\
&\simeq \frac{m}{p}.
\end{aligned} \tag{1.19}$$

In high-energy spectroscopy, a large angular dispersion is preferred to distinguish two different wavelength components close to each other. From Eqn. (1.19), it is obvious that the angular dispersion can be increased by using a fine pitch grating at high diffraction orders.

The resolving power or spectral resolution represents the smallest wavelength or energy that a grating can resolve or distinguish. Based on Rayleigh's criterion, the resolving power is defined as,

$$\begin{aligned}
\frac{\lambda}{\Delta\lambda} &= \frac{mW}{p} = mN \\
&= \frac{p(\sin\alpha + \sin\beta)}{\lambda} N
\end{aligned} \tag{1.20}$$

where $W$ is the size of the grating (or illumination), $N$ is the total number of grooves coherently illuminated, $m$ is the diffraction order, and $p$ is the grating period. Therefore, a fine pitch is essential to increase the resolving power of the grating. Sometimes, the resolving power is equivalently expressed in terms of energy resolution, $E/\Delta E$. In that case, one can convert the wavelength to the corresponding photon energy [14],

using

$$E(\text{keV}) = \frac{12.4}{\lambda(\text{Å})}. \tag{1.21}$$

In this section, I described the basic principles and parameters of the conventional gratings, and advantages and disadvantages of transmission and reflection types. An 'ideal' grating should combine the alignment and figure insensitivity of transmission gratings with high broadband diffraction efficiency, which traditionally has been the domain of blazed reflection gratings.

## 1.2 X-ray Astronomy

The universe contains an immense number of energetic objects such as neutron stars, black holes, supernovas, and merging galaxies. Astronomers have long been studying vast celestial events emanating not only visible light but also much x rays. X-ray spectroscopy has an important role in analyzing the x rays from the celestial objects as the quantitative spectral data provides clues on the material composition and temperature of the objects. For example, Fig. 1-5 compares optical and x-ray images of the gigantic explosion, a supernova remnant, of a star after a supernova. Without the x-ray images, we could not observe or analyze the interesting phenomena. In addition to x-ray images, radiation spectra can provide us with quantitative data on the constituent components of the ejected material expanding from the explosion. Mongrard [14] described a detailed history of x-ray astronomy and x-ray formation and origins.

Diffraction gratings have been used by x-ray astronomers to reveal the mysteries of an invisible universe above the atmosphere which absorbs incoming x rays [4, 15–19]. The Chandra X-ray Observatory, launched in 1999, is equipped with grating-based spectrometers consisting of 200 and 400 nm-period gold transmission gratings [15, 18–20]. Figure 1-6 shows the huge spacecraft of the Chandra X-ray Observatory and the basic configuration of the grating-based spectrometer. The incident x rays, guided by

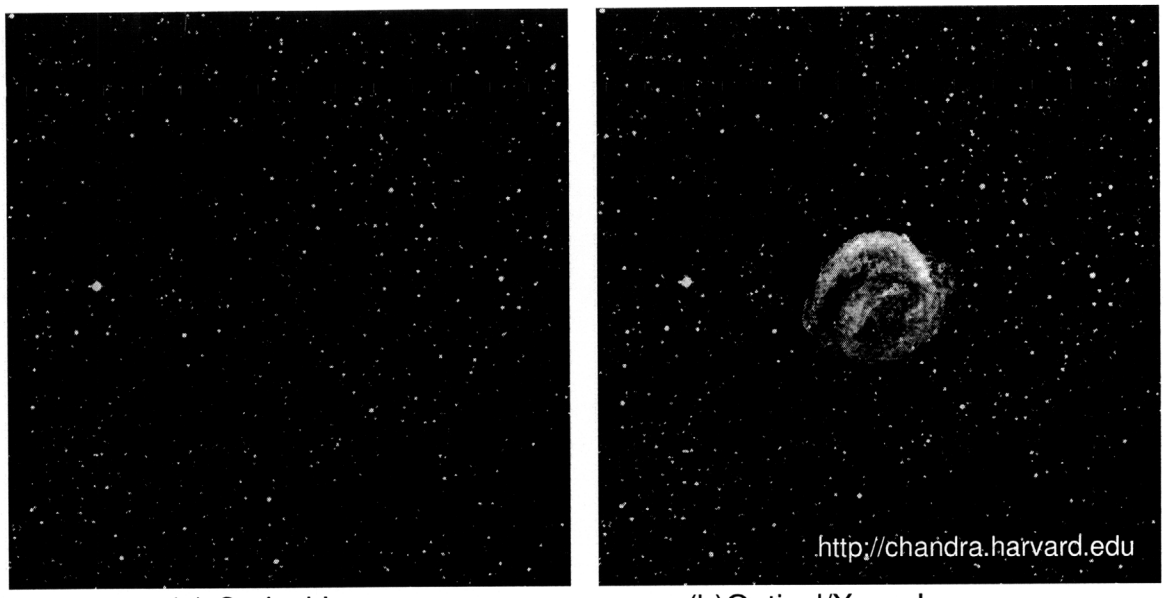


(a) Optical Image (b)Optical/X-ray Image

Figure 1-5: (a) Optical and (b) x-ray/optical views of Kepler's Supernova Remnant

parabolic and hyperbolic thin foil optics, are diffracted by the transmission grating assembly and focused on the CCD* camera. The 200 nm-period gold gratings in the Chandra, High Energy Transmission Grating Spectrometer (HETGS), are phase gratings designed to efficiently work in a soft x-ray range of 0.5 - 10 keV with a spectral resolution ($E/\Delta E$) of 60 - 1000. However, the maximum diffraction efficiency in the first orders was only about 20% even though the theoretical efficiency of an ideal (non-absorbing) phase grating is as high as 40% in each first order [2]. One of the main causes of the efficiency loss is absorption of x rays in the grating bars. This relatively low diffraction efficiency is a major disadvantage of the transmission grating spectrometer.

The *X-ray Multi-Mirror Mission (XMM)-Newton* of the European Space Agency (ESA) is a large effective area x-ray telescope with an in-plane blazed reflection grating spectrometer (RGS) [17]. Compared to the diffraction efficiency of the HETGS, XMM's RGS has a bit higher peak efficiency about 30% with a spectral resolution ($E/\Delta E$) up to 800 at 0.5 - 10 keV. However, the weight of the RGS assembly is about 6 times that of Chandra's grating assembly (10 kg). Weight is a very important factor

*Charge-coupled device

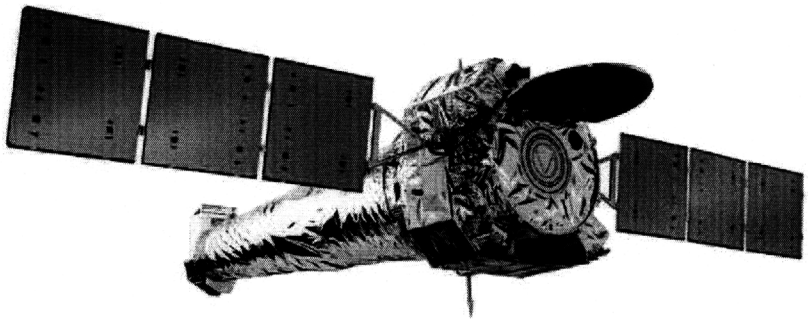

(a) Chandra x-ray Observatory

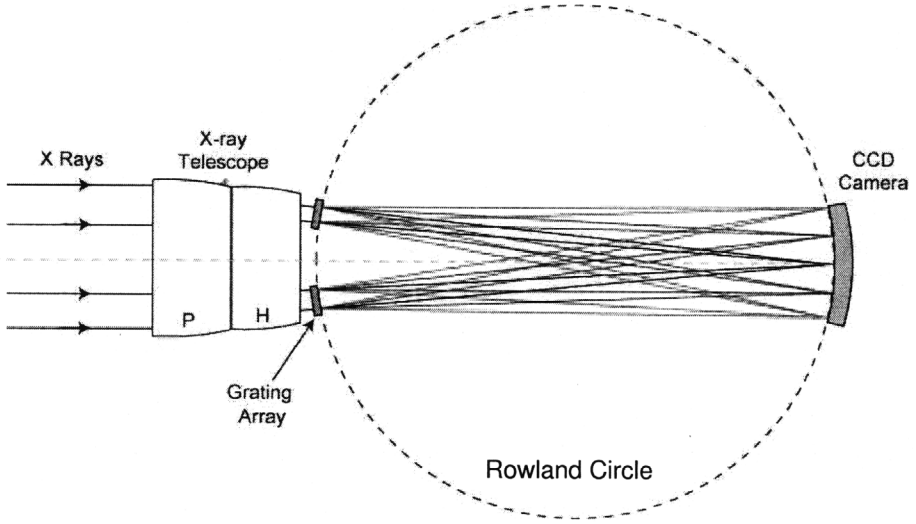


(b) Concept of an x-ray spectrometer with transmission gratings

Figure 1-6: (a) Chandra X-ray Observatory launched in 1999. The length and width are about 10 m and 20 m, respectively. (b) Configuration of a space x-ray telescope with the transmission gratings

in space instrumentation because it directly affects the launching cost.

The Suzaku telescope of the Japan Aerospace Exploration Agency (JAXA) was recently launched in 2005 [21]. It features the first x-ray astronomy mission with an x-ray micro-calorimeter [22]. Since the micro-calorimeter has a fixed minimum energy resolution ($\Delta E = 6$ eV), the energy resolution ($E/\Delta E$) increases with the photon energy. Thus, the micro-calorimeter provides a higher spectral resolution in higher energy bands, while the grating spectrometer with a fixed $\Delta\lambda$ dispersion performs better in lower energy bands.

Table 1.1: Comparison of major recent and future x-ray missions [5, 23]

| | Chandra | XMM-Newton | Suzaku (Astro-E2) | IXO (formerly Con-X) |
|---|---|---|---|---|
| Year | 1999 | 1999 | 2005 | 2017+ |
| Collecting Area ($m^2$ @ 1keV) | 0.1 | 0.15 | 0.04 | 3 |
| Angular Resolution (HPD[a]) | 0.5″ | 15″ | 90″ | 5″ |
| Energy Range (keV) | 0.1 - 10 | 0.1 - 15 | 0.2 - 600 | 0.3 - 40 |
| Spectroscopy technology | Transmission Gratings | Reflection Gratings(In-plane) | Micro-calorimeter | Micro-calorimeter + grating |
| Resolving Power($E/\Delta E$)[b] | 60- 1000 @ 0.5-10 keV | 200-800 @ 0.3-2.5 keV | Fixed $\Delta E$= ~6.5 eV | 3000 @1 keV 2400 @6 keV |

[a] half power diameter (HPD)
[b] The data in the table is shown for a part of the energy range as an example.

The next generation x-ray astronomy mission is an international joint project with NASA, ESA, and JAXA, named the International X-ray Observatory (IXO) and planned for launch around 2017 [23]. Currently, the performance requirements are being defined based on previous mission concepts such as *Constellation-X* of NASA and *XEUS* of ESA. A micro-calorimeter detector with fixed $\Delta E$ ($\sim$ 2.5 eV) would be equipped for spectroscopy for higher energy bands. Since a single spectroscopic technology cannot cover such a large energy range with high resolution, an additional grating-based spectrometer would be mounted to supplement the calorimeter's insufficient performance in the lower energy band. Table 1.1 summarizes the features of major recent and future x-ray missions.

However, as explained above, the conventional transmission and reflection gratings have their own weaknesses. Therefore, the goal of this thesis is to develop a new type of diffraction grating for soft x-ray spectroscopy, combining the advantages of transmission gratings and blazed grazing-incidence reflection gratings. It is also desired that the new grating technology complements the micro-calorimeter for higher

Table 1.2: Comparison of spectroscopy technologies for x-ray space telescopes

| | Transmission grating | Reflection grating | Micro-calorimeter |
|---|---|---|---|
| Advantages | Insensitive to misalignment<br>Low mass | High diffraction efficiency | High resolution @ high energy |
| Disadvantages | Low diffraction efficiency | Tight alignment tolerance<br>High mass | Fixed energy resolution ($\Delta E$) |

energy bands. The CAT grating is a blazed transmission grating with high diffraction efficiencies for lower energy bands and is almost transparent for higher energy bands focusing to the micro-calorimeter. Table 1.2 compares advantages and disadvantages of major spectroscopy technologies for space instrumentation.

## 1.3 Interference Lithography and the MIT Nanoruler

Interference lithography (IL) is a method to efficiently pattern large area gratings in a relatively short time. Figure 1-7 is a typical setup for IL with two mutually coherent plane waves. The two beams produce sinusoidal interference fringes which are recorded in photosensitive material or photoresist on the substrate. The grating period is found from the intensity pattern of the interference. Two mutually coherent beams, $\vec{E_1}$ and $\vec{E_2}$, are incident with an angle $\theta$ from air, and refracted into the recording material with an angle $\theta'$ according to Snell's law,

$$\theta' = \sin^{-1}(\frac{1}{n}\sin\theta), \tag{1.22}$$

where $n$ is the refractive index of the recording material.

The electric fields in the material then are given by,

$$\vec{E_1} = E_1\hat{e_1}\exp i(\vec{k_1}\cdot\vec{r} - wt), \tag{1.23}$$

$$\vec{E_2} = E_2\hat{e_2}\exp i(\vec{k_2}\cdot\vec{r} - wt), \tag{1.24}$$

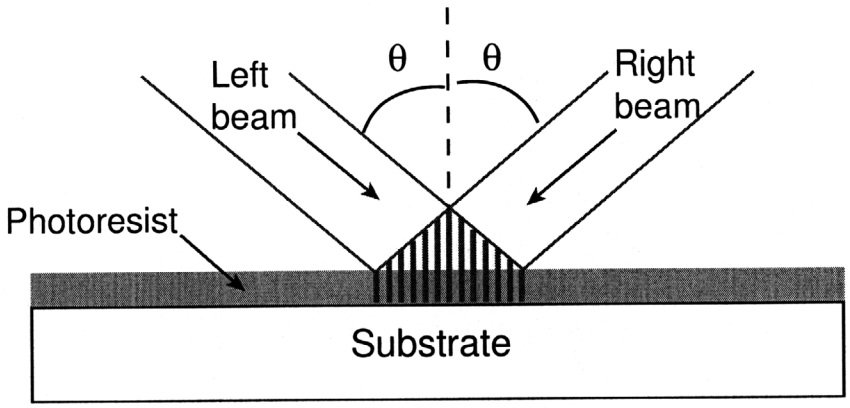


Figure 1-7: The basic concept of interference lithography.

where $E_1$ and $E_2$ are the amplitudes, $\hat{e_1}$ and $\hat{e_2}$ are unit polarization vectors, $\vec{k_1}$ and $\vec{k_2}$ are wave vectors, space vector $\vec{r} = x\hat{x} + z\hat{z}$, and $w$ is the angular frequency. The polarization vectors for the TE (Fig. 1-8) and TM (Fig. 1-9) waves are given by,

$$\begin{aligned} &\text{TE}: \quad \hat{e_1} = \hat{e_2} = \hat{y}, \\ &\text{TM}: \quad \begin{cases} \hat{e_1} &= -\cos\theta'\hat{x} + \sin\theta'\hat{z}, \\ \hat{e_2} &= -\cos\theta'\hat{x} - \sin\theta'\hat{z}. \end{cases} \end{aligned} \tag{1.25}$$

The wave vectors are given by,

$$\vec{k_1} = k\sin\theta'\hat{x} + k\cos\theta'\hat{z}, \tag{1.26}$$

$$\vec{k_2} = -k\sin\theta'\hat{x} + k\cos\theta'\hat{z}. \tag{1.27}$$

where $k$ is the angular wave number in the material ($k = 2n\pi/\lambda$). The intensity pattern is given by,

$$\begin{aligned} I(\vec{r}) &= <|\vec{E_1} + \vec{E_2}|^2> \\ &= \frac{E_1^2}{2} + \frac{E_2^2}{2} + E_1E_2 < (\hat{e_1}\cdot\hat{e_2})\cos((\vec{k_1} - \vec{k_2})\cdot\vec{r}) > . \end{aligned} \tag{1.28}$$

Thus, the intensity for the TE and TM polarizations are given by

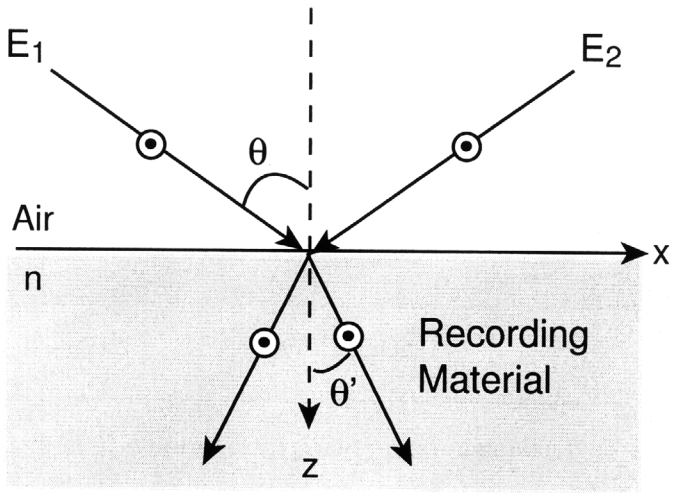


Figure 1-8: Interference of two TE-waves.

$$I(\vec{r})_{\mathrm{TE}} = \frac{E_1^2}{2} + \frac{E_2^2}{2} + E_1 E_2 \cos(-2k(\sin\theta')x), \tag{1.29}$$

$$I(\vec{r})_{\mathrm{TM}} = \frac{E_1^2}{2} + \frac{E_2^2}{2} + \cos 2\theta' E_1 E_2 \cos(-2k(\sin\theta')x). \tag{1.30}$$

For the both of cases, we can find a periodicity ($\Lambda$) in the x direction,

$$\Lambda = \frac{\lambda}{2n\sin\theta'} = \frac{\lambda}{2\sin\theta}. \tag{1.31}$$

The contrast ($\Gamma$) is defined as

$$\begin{aligned} \Gamma &= \frac{I_{max} - I_{min}}{I_{max} + I_{min}} \\ &= \frac{2E_1 E_2(\hat{e_1}\cdot\hat{e_2})}{E_1^2 + E_1^2}. \end{aligned} \tag{1.32}$$

Therefore, the contrast of interference of the TM waves degrades as a function of the incident angle and the refractive index of the recording material because $\hat{e_1}\cdot\hat{e_2} = \cos 2\theta'$ for TM waves. Thus, TE-polarized waves are always used for IL due to $\hat{e_1}\cdot\hat{e_2} = 1$.

Based on the basic concept of IL, our group has developed a scanning beam interference lithography (SBIL) tool, the MIT Nanoruler [8, 24, 25]. While the traditional IL systems suffer from a hyperbolic phase (Fig. 1-10 (a)) and a noise problem

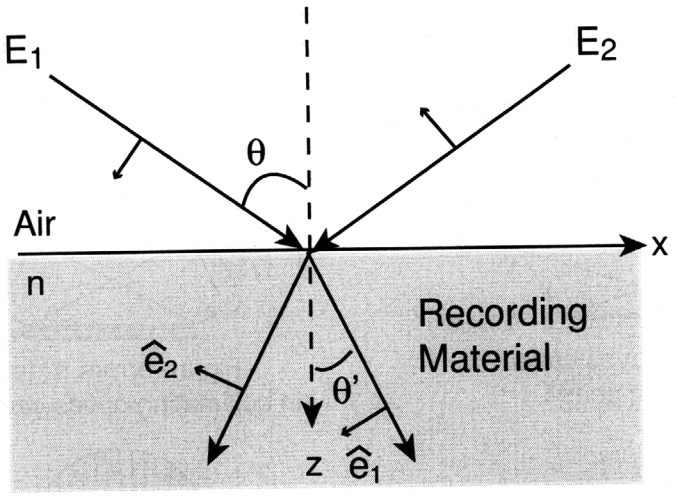


Figure 1-9: Interference of two TM-waves.

due to optics' figure errors (Fig. 1-10 (b)), the Nanoruler has much high phase fidelity over large area because a small ($\sim$ 1 $mm^2$) fringe-locked interference beam is scanned. The overlap scanning scheme also spatially averages high frequency phase distortions, which makes possible to pattern high quality gratings over the whole substrate area. Figure 1-11 shows the basic concept of the SBIL scheme. The patterning area is limited by the interferometer stage movement and the current stage in the MIT Nanoruler can accept a 300 mm wafer. The grating period is determined by the wavelength of the laser and incident angle according to Eqn. (1.31). Since we use an Ar-ion laser with 351.1 nm wavelength, the Nanoruler can pattern down to $\sim$200 nm-period gratings. Recently, our group has demonstrated a possibility to pattern down to 50 nm-period gratings using an overlay technique and a multilevel fabrication process [26, 27]. A tight control of period and duty cycle, phase metrology, and a precise process control made it possible to overlay 200 nm-period gratings four times to produce 50 nm-period ones. Figure 1-12 shows the optical bench, the interferometer stage, and a patterned 300 mm wafer. The wafer has a 400 nm-period grating pattern in the photoresist. One advantage of the Nanoruler is a relatively fast patterning capability due to the high performance stage. Only about 45 minutes was taken to pattern the entire area of 300 mm wafer. The Nanoruler is the lithography tool used for all the grating patterning processes shown in this thesis.

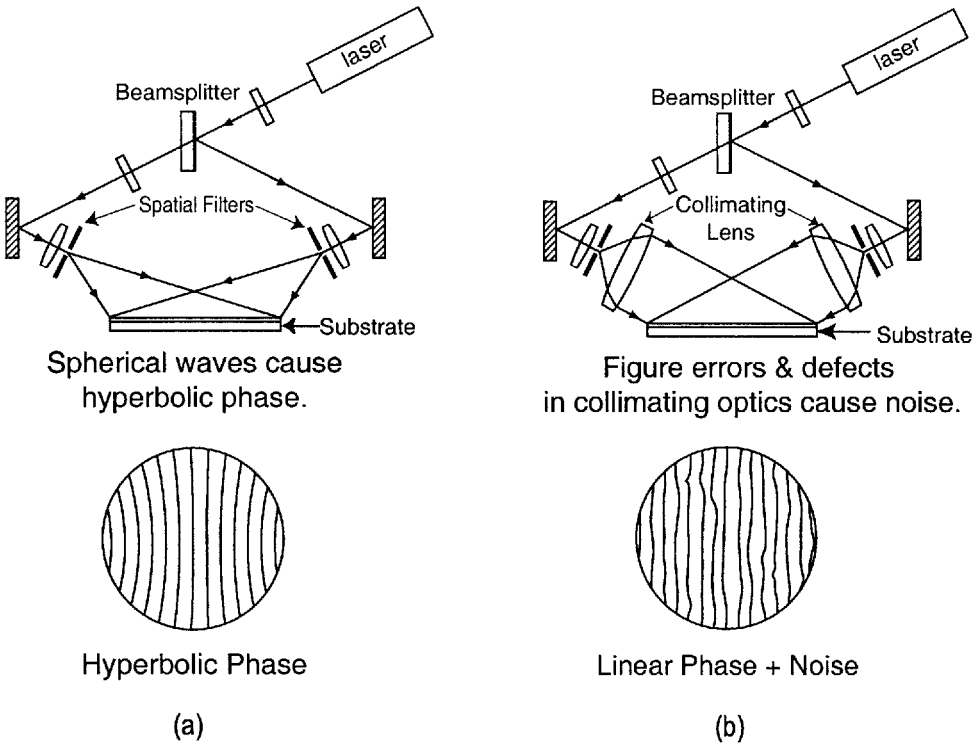


Figure 1-10: Illustration of two different setups for traditional IL and their problems.

## 1.4 Anisotropic Etching

Anisotropic etching is a microfabrication technique used to form desired structures using etchants whose etch rate is sensitive to crystallographic orientation. Compared to isotropic etching, where the etch rate is homogeneous in all directions, anisotropic etching has an advantage in creating nanostructures with a high aspect ratio. Figure 1-13 illustrates the etch profiles of the isotropic and anisotropic etch process. In an ideal anisotropic etching process (Fig. 1-13(b)), the undercut due to lateral etching is zero and the sidewall slope becomes 90°. In reality, there is never a perfect anisotropic etchant or etch process, so we can define an etch anisotropy or etch rate ratio as

$$\mathrm{Ae} = \frac{\mathrm{R_{vertical}}}{\mathrm{R_{lateral}}}, \tag{1.33}$$

where $R_{\mathrm{vertical}}$ and $R_{\mathrm{lateral}}$ are the etch rates for the denoted directions.

The most common anisotropic etchants for silicon etching are tetramethylammonium hydroxide (TMAH) and potassium hydroxide (KOH) [28]. Refs. [28–30]

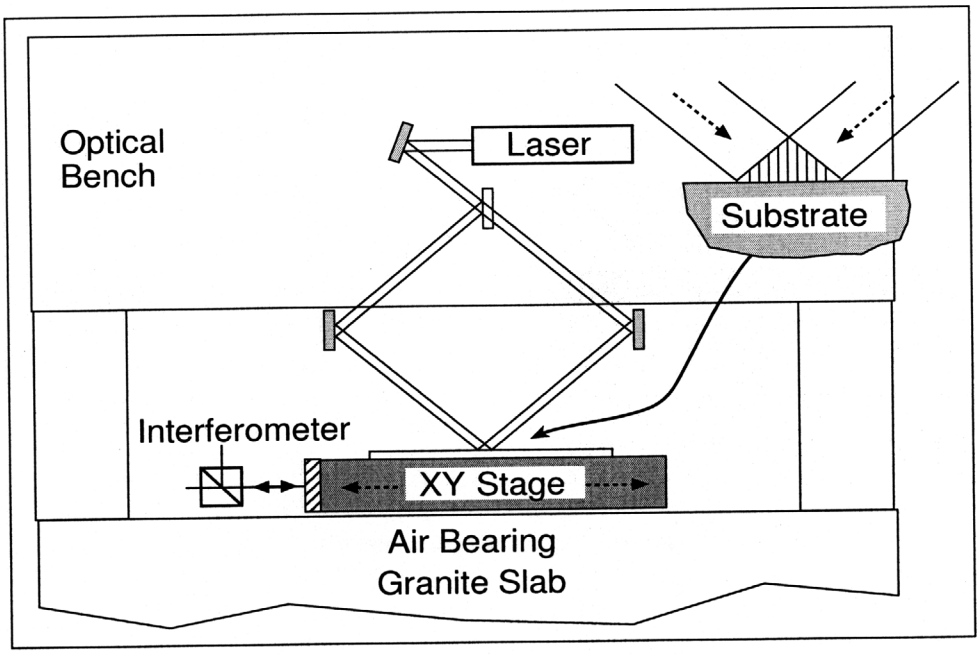


Figure 1-11: The concept of the Nanoruler

describes the different etch characteristics of KOH and TMAH. TMAH is an attractive anisotropic etchant because it has CMOS-compatibility, relatively low toxicity, and a very high selectivity between silicon and silicon dioxide ($SiO_2$). The $SiO_2$ etch rate in TMAH is four orders of magnitude lower than $\langle 100 \rangle$ Si. However, TMAH has lower etch anisotropy between $\langle 110 \rangle$ and $\langle 111 \rangle$ than KOH. Generally speaking, Ae of KOH is an order of magnitude higher than that of TMAH. However, KOH is not compatible with CMOS processing because aluminum is attacked by KOH quickly and alkali metal ions may contaminate the gate oxide [29]. Since KOH etches $SiO_2$ even faster than TMAH does, silicon nitride is often used as a masking material for KOH etch processes instead of $SiO_2$. Table 1.3 summarize silicon etch characteristics of KOH and TMAH solutions.

KOH solutions have been widely used to fabricate various silicon structures which require a high etch rate ratio between crystallographic planes [28, 32–36]. Because of the high etch anisotropy between $\{110\}$ and $\{111\}$ planes, $\langle 110 \rangle$ wafers are utilized to fabricate deep vertical trenches and high aspect ratio structures. In addition, the $\{111\}$ planes are known to be atomically smooth and this property can be used for many optical applications which need mirror-like surfaces. Figure 1-14(a) depicts

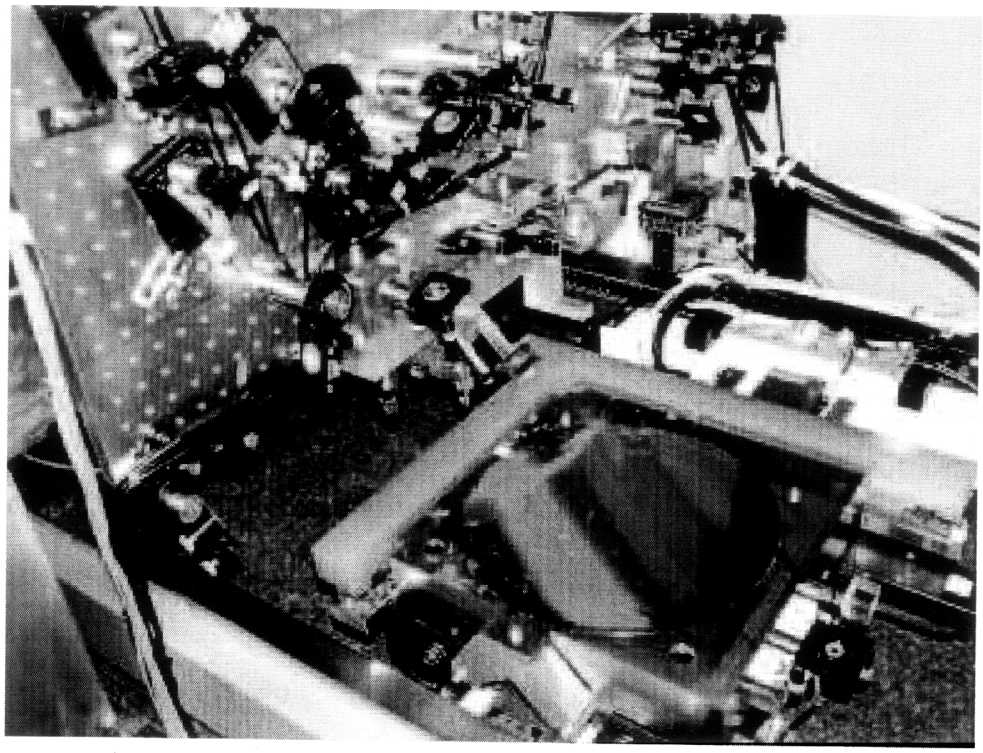

Figure 1-12: Photograph of the Nanoruler and 300 mm wafer with 400 nm-period grating.

a typical $\langle 110 \rangle$ silicon wafer with two flats in the $\langle 111 \rangle$ direction. Along the flat directions, the wafer can be cleaved in a parallelogram shape with a corner angle of 70.5°. With an etch mask with the parallelogram shape, we can expect the etch profile based the etch anisotropy between $\{110\}$ and $\{111\}$ planes (Fig. 1-14(b)). We can produce deep vertical trenches by aligning the mask to a pair of the vertical $\{111\}$ planes, but the etch depth ($D$) is always limited by the mask width ($L$).

Looking at diverse and sometimes conflicting experimental data in the literature, it is unsurprising there is not a mutually agreed model for the anisotropic etching mechanism. Temperature, concentration, crystal direction, feature size, additives, agitation, oxygen contents in silicon, and mask material can all affect anisotropic etching [28, 32, 37]. Kendall [32] tried to explain etch anisotropy based the low available bond density and fast oxidation on the $\{111\}$ surface. However, the available bond density in the silicon crystal follows the sequence 1:0.71:0.58 for the $\{100\}$:$\{110\}$:$\{111\}$ surfaces, respectively, and the oxidation rate is $\{111\}>\{110\}>\{100\}$. Neither of these arguments can simultaneously explain the slow (orders of magnitude) etch rate of

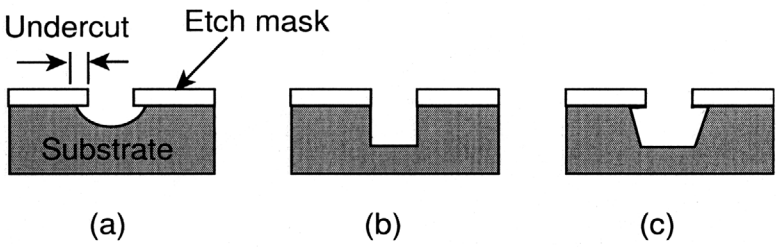


Figure 1-13: Illustration of etch profiles in (a) isotropic and (b) ideal anisotropic cases; (c) shows a common anisotropic etch profile in practice.

Table 1.3: Major characteristics[a] of KOH and TMAH solutions for silicon etching [28,31].

| | KOH | TMAH |
|---|---|---|
| Etch rate ($\mu$m/min) @ 80° | 1-2 | ~1 |
| Anisotropy | ~200 | ~50 |
| Mask (selectivity) | $Si_3N_4$ ($> 10^3$) | $SiO_2$ ($> 10^4$) |
| Roughness | very low | moderate |
| CMOS-compatible | no | yes |
| Toxicity | moderate | low |

[a] Note: Given the many possible variables, the data in the table are only typical examples

the {111} planes and the etch rate sequence {110}>{100}>{111}. Seidel *et al.* [37] proposed a theory based on the difference of backbond geometries (Fig. 1-15) and activation energies in the different surfaces. On {111} planes, three backbonds are below the plane, so the activation energy is relatively higher than on other planes. In that way, they explained the slow {111} etch rate. Ref. [37] describes the electrochemical model in detail and provides lots of experimental data. Another theory by Elwenspoek [38] was inspired by crystal growth theories. A smooth surface has the lowest surface energy and there is a nucleation barrier hindering formation of an island or cavity of atoms. Elwenspoek concluded the atomically smooth {111} surfaces etched much slower than others due to the surface energy and nucleation barrier. Although the history of anisotropic etching is quite long and it has been broadly used in microfabrication, the exact mechanism is still in mystery.

Previous experimental researchers reported the etch characteristics of ⟨110⟩ silicon

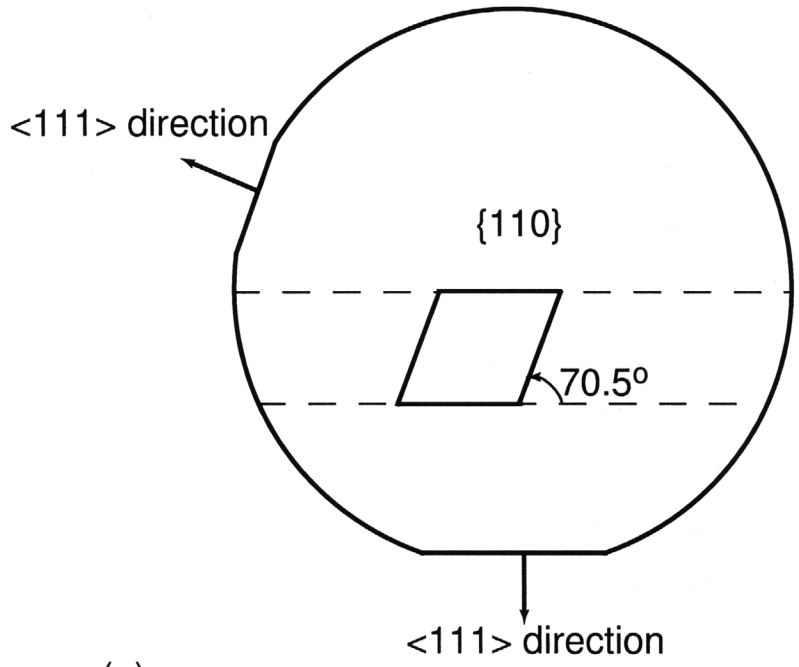


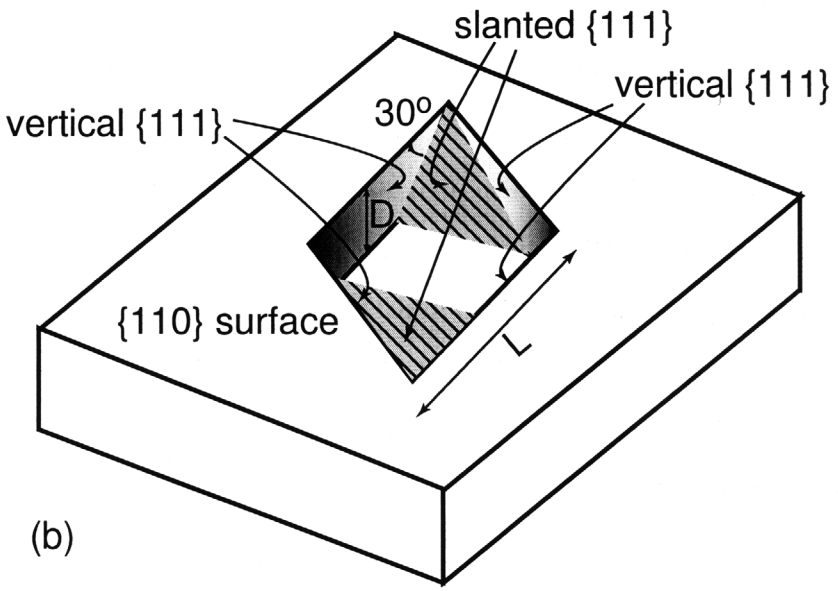


Figure 1-14: (a) A ⟨110⟩ silicon wafer flat orientations and cleavage parallelogram along {111} planes. (b) Anisotropic etch profile of ⟨110⟩ silicon consisting of two pairs of vertical {111} planes and two 35.26° tilted {111} planes from the top ⟨110⟩ surface. The projection of the slanted {111} planes onto the vertical {111} has an angle of 30° from the top ⟨110⟩ surface.

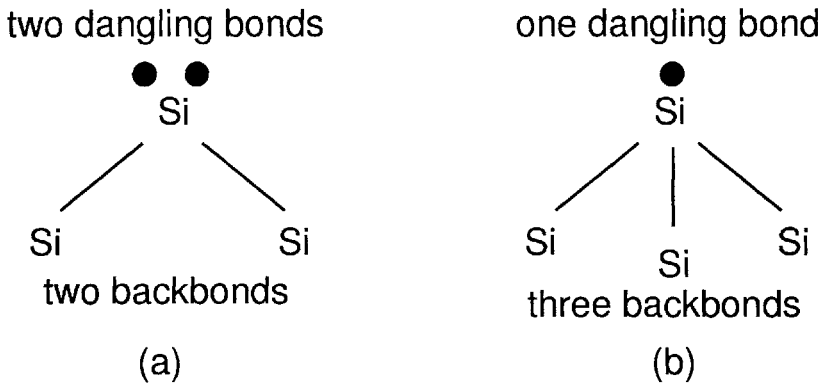


Figure 1-15: Dangling bonds and backbonds of Si atoms on (a) a {100} plane and (b) a {111} plane [28,37].

in certain ranges of temperature and concentration of KOH solution [37,39–41]. The etch rates and their ratios were taken from tens of micrometer size patterns in wafers or from hemispherical bulk silicon specimens, which provided good enough information to fabricate general micro-electro-mechanical systems (MEMS) applications. Sometimes the ⟨111⟩ etch rate was ignored because it is hundreds of times slower than the ⟨110⟩ etch rate, and it was not so critical when fabricating shallow trenches. However, the CAT gratings are difficult to fabricate without an ultra-high etch anisotropy because the grating bars will be in an extreme geometry with a period of 100 - 200 nm and height of 3 - 6 $\mu$m. Therefore, conventional KOH etch processes cannot directly be applied for the CAT grating fabrication, which may cause a large amount of undercut and non-uniform etch profiles. In this thesis, the KOH etch process will be optimized to develop the CAT gratings which require ultra-high-aspect-ratio ($> 100$) free-standing grating bars with smooth sidewalls.

## 1.5 Overview of Thesis

The main goal of this thesis is to present the development of fabrication processes for the CAT gratings. Chapter 2 describes the basic concept and design of the CAT grating which combines advantages of transmission and blazed reflection gratings. Simple ray tracing and phase calculations will be used to explain the blazing effect of the CAT grating. Very high aspect-ratio grating structures are required due to a

shallow critical angle for reflection of x rays.

Based on the challenging design parameters, Chapter 3 will present a silicon-on-insulator (SOI) process to fabricate an initial prototype CAT grating with a relatively large period (574 nm). The fabricated prototype CAT grating has grating bars with an aspect ratio of ~150, as required.

Chapter 4 describes process improvements in an effort to adapt the previous process to 200 nm-period CAT gratings. The KOH anisotropic etching process was optimized to provide a high etch anisotropy and good uniformity over the entire grating area. The highest anisotropy was achieved with a high concentration KOH solution at room temperature. A surfactant and ultrasonic agitation ameliorated the etch uniformity by mitigating micro-making due to hydrogen bubbles. An image reversal process was applied to address a rapid initial undercut problem which had significantly narrowed the process latitude.

Chapter 5 covers mechanical modeling of a stress-induced stiction problem due to buckling. Releasing the thin grating planes by etching the buried oxide of a SOI substrate in hydrofluoric acid caused the random stiction between grating planes. A mechanical model for plate buckling was used to predict the stiction problem of the grating planes with a support structure on a thick oxide layer in a compressive stress. The stiction was eliminated by using much thinner buried oxide, which also proved that the compressive stress in the oxide caused the problem. Finite element modeling was used to determine appropriate support structure opening widths and oxide thickness to avoid buckling of the grating planes.

The KOH etch process in a $\langle 110 \rangle$ wafer produces four vertical and two tilted surfaces. The latter limits the CAT grating area and maximum etch depth, which leads to loss of diffraction efficiency. In order to minimize the support area blocking incident x rays, a vertical etch process without crystallographic dependence should precede the KOH etch process. Chapter 6 examines feasibility of reactive ion etching followed by KOH polishing to engineer the support structure.

Chapter 7 presents results of x-ray diffraction tests of the CAT gratings. The experimental data agreed with the theoretical prediction within 70-85 %. As predicted

by theory, there was the blazed effect and the blazed order had prominent diffraction efficiency enhancement.

# Chapter 2

# The Critical-Angle Transmission Grating

In this chapter, I will introduce the concept of the critical-angle transmission (CAT) grating with a simple model that describes its key principles. As an analogy to a blazed reflection grating, the CAT grating redirects most of diffracted orders toward one side of the zero$^{th}$ order instead of spreading them symmetrically like a traditional transmission grating. A particular diffracted order that satisfies the so-called blaze condition is expected to have a significantly enhanced diffraction efficiency. Although it might be confused with a reflection grating because there is reflection off of the grating sidewalls, it is a true transmission grating where the zero$^{th}$ order passes through the grating surface. This breakthrough invention by our group realizes a blazed "transmission" grating without much efficiency loss due to absorption. Figure 2-1 shows the difference in configuration and the blaze direction of a blazed reflection grating and the CAT grating. Although the simple modeling will give a qualitative prediction of blazing phenomenon with the CAT grating, there are many other factors omitted in the analytical model. For example, the three-dimensional (3D) character of the CAT grating, reflectivity of material, and partial absorption in the grating bars can all affect the diffraction efficiency. Therefore, more detailed performance will be predicted using the rigorous coupled-wave analysis (RCWA), which provides exact solutions of Maxwell's equations for the diffraction of electromagnetic

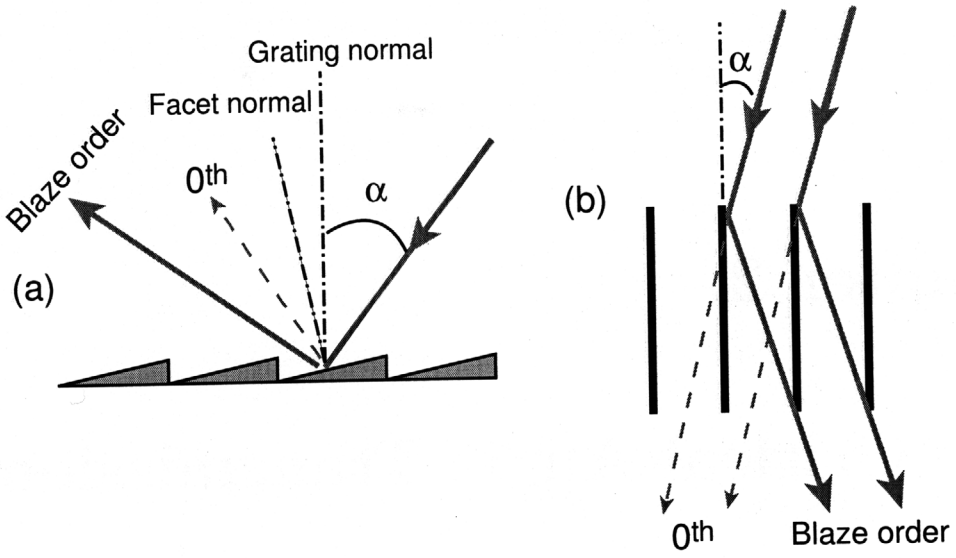


Figure 2-1: Cross-section schematic of a blazed reflection and CAT grating. The incident beams have an angle $\alpha$ to the grating surface normal. (a) For a blazed reflection grating, the blaze order accords with the direction of specular reflection off of the grating facet. (b) In the CAT grating configuration, the blaze direction coincides with the specular reflection off of the grating sidewalls, while the zero$^{th}$ order passes through the grating bars.

waves from various 3D grating structures [2, 42, 43].

In spite of the clever invention of the CAT grating, the CAT grating geometry is challenging to realize for diffraction of soft x-rays because the angle for total external reflection is only a few degrees in that energy range [44, 45]. For example, the grating bars are required to have a very high aspect ratio ($> 100$). In this chapter, I will go over the geometric design parameters for the CAT gratings and the consequent fabrication challenges.

## 2.1 Principle of the CAT grating

Intensity distribution from a general grating can be formulated using the Fraunhofer diffraction pattern of multiple slits [46, 47]. For a monochromatic plane wave incident with an angle $\alpha$ with respect to the grating normal, the resultant complex amplitude

through $N$ slits with a period $p$, is the sum of the series,

$$\begin{aligned} Ee^{i\phi} &= E_s\left(1+e^{i\delta}+e^{i2\delta}+e^{i3\delta}+...+e^{i(N-1)\delta}\right) \\ &= E_s\frac{1-e^{iN\delta}}{1-e^{i\delta}}, \end{aligned} \tag{2.1}$$

where $E$ and $\phi$ are the resultant amplitude and phase, respectively, $E_s$ represents the equal amplitude contribution by the individual slits, $\delta$ is the phase change from one slit to the next. From the geometry in Fig. 2-2 and sign convention ($\alpha > 0$ and $\beta < 0$), the phase change $\delta$ is given by

$$\begin{aligned} \delta &= \frac{2\pi}{\lambda}(\overline{AA'}-\overline{BB'}) \\ &= \frac{2\pi}{\lambda}p(\sin\alpha+\sin\beta). \end{aligned} \tag{2.2}$$

The intensity is then found by multiplying $Ee^{i\phi}$ by its complex conjugate, giving

$$\begin{aligned} E^2 &= {E_s}^2\frac{(1-e^{iN\delta})(1-e^{-iN\delta})}{(1-e^{i\delta})(1-e^{-i\delta})} \\ &= {E_s}^2\frac{2-2\cos N\delta}{2-2\cos\delta} \\ &= {E_s}^2\frac{\sin^2 Ng}{\sin^2 g}, \end{aligned} \tag{2.3}$$

where $g = \delta/2$ signifies one-half the phase difference from one slit to the next. The intensity ${E_s}^2$ of the individual slits is given by a sinc function,

$${E_s}^2 = \left(\frac{E_0}{N}\right)^2\left[\frac{\sin f}{f}\right]^2, \tag{2.4}$$

where $(E_0/N)^2$ is the normalized intensity of any one of the silts and $f$ represents one-half the phase difference between the contributions coming from opposite edges of the slit. Thus $f$ can be found from the geometry shown in Fig. 2-3, given by

$$\begin{aligned} f &= \frac{1}{2}\left(\frac{2\pi}{\lambda}(\overline{CC'}-\overline{DD'})\right) \\ &= \frac{\pi}{\lambda}a(\sin\alpha+\sin\beta). \end{aligned} \tag{2.5}$$

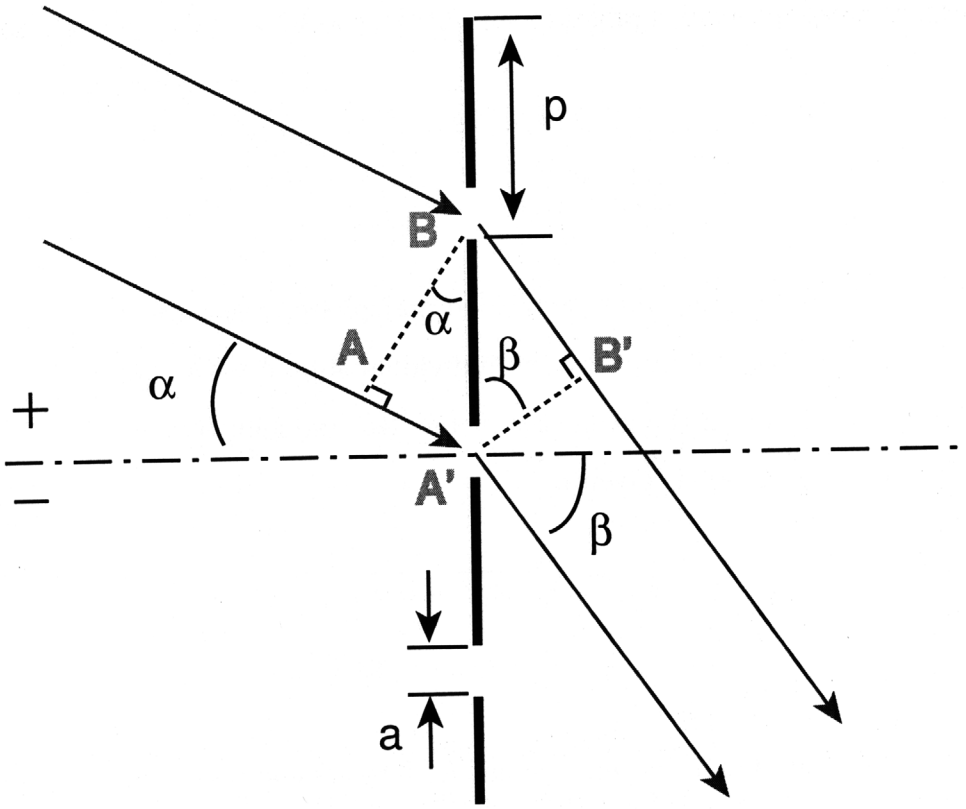


Figure 2-2: Illustrating the diffraction of a plane wave by multiple slits with a period $p$. The phase changes by equal amount from one slit to the next.

Note that $\alpha > 0$ and $\beta < 0$. Therefore, the normalized diffraction intensity distribution from $N$ slits can be expressed as

$$I_{tot} = I_g \cdot I_s = \left[\frac{\sin Ng}{N \sin g}\right]^2 \left[\frac{\sin f}{f}\right]^2, \tag{2.6}$$

where

$$g = \frac{p\pi}{\lambda}(\sin\alpha + \sin\beta) \tag{2.7}$$

and

$$f = \frac{a\pi}{\lambda}(\sin\alpha + \sin\beta). \tag{2.8}$$

Figure 2-4 shows an example of Fraunhofer diffraction by a grating of ten slits. Based on the simple model above, the overall diffraction pattern (Fig. 2-4(c)) can be expressed by the normalized grating interference ($I_g$) and single slit diffraction ($I_s$), which define the peak locations and form the intensity envelope, respectively.

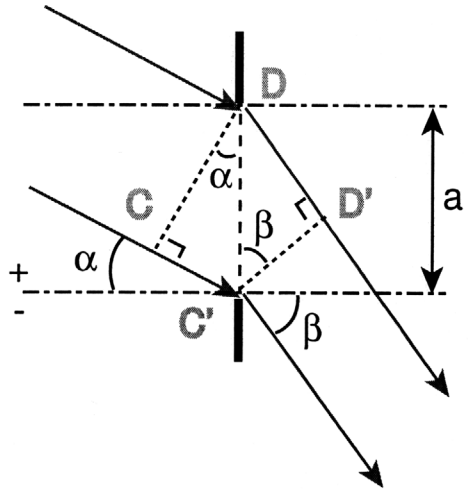


Figure 2-3: Fraunhofer diffraction by a single slit with an open width $a$.

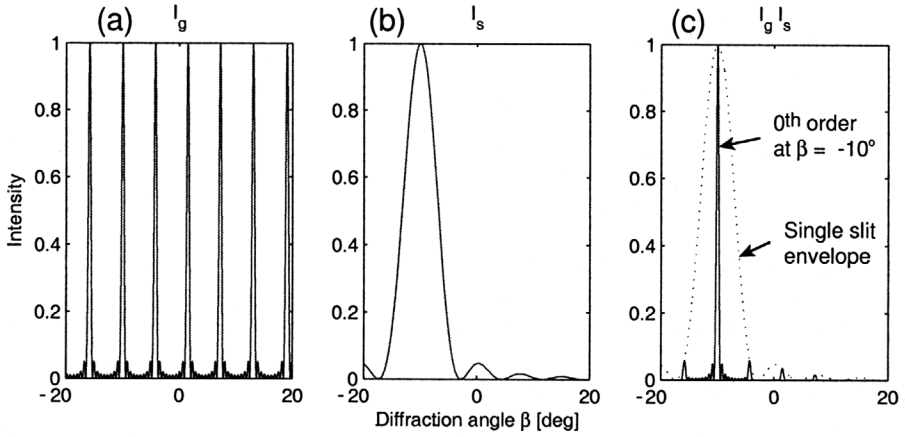


Figure 2-4: Example of the Fraunhofer diffraction from a traditional transmission grating with $N = 10$, $\alpha = 10°$, $p = 100$ nm, $a = 80$ nm, and $\lambda = 10$ nm. (a) Grating interference function ($I_g$), (b) single slit diffraction function ($I_s$), and (c) overall diffraction pattern of the slits as a product of $I_g$ and $I_s$.

The incident angle $\alpha$ is 10° and we can find the maximum intensity at the zero$^{th}$ order passing through the grating, where the diffraction angle $\beta$ is defined as $-10°$. Therefore, in the conventional transmission grating configuration, most of diffracted power goes to the zero$^{th}$ order, which is undesirable at least for spectroscopic purposes.

Now let us look at the CAT grating geometry. How do we adapt these equations to a CAT grating model? We need to accordingly modify the phase change terms, $g$ and $f$, considering the geometry shown in Fig. 2-5. The incident beams are reflected off at the grating planes or sidewalls.

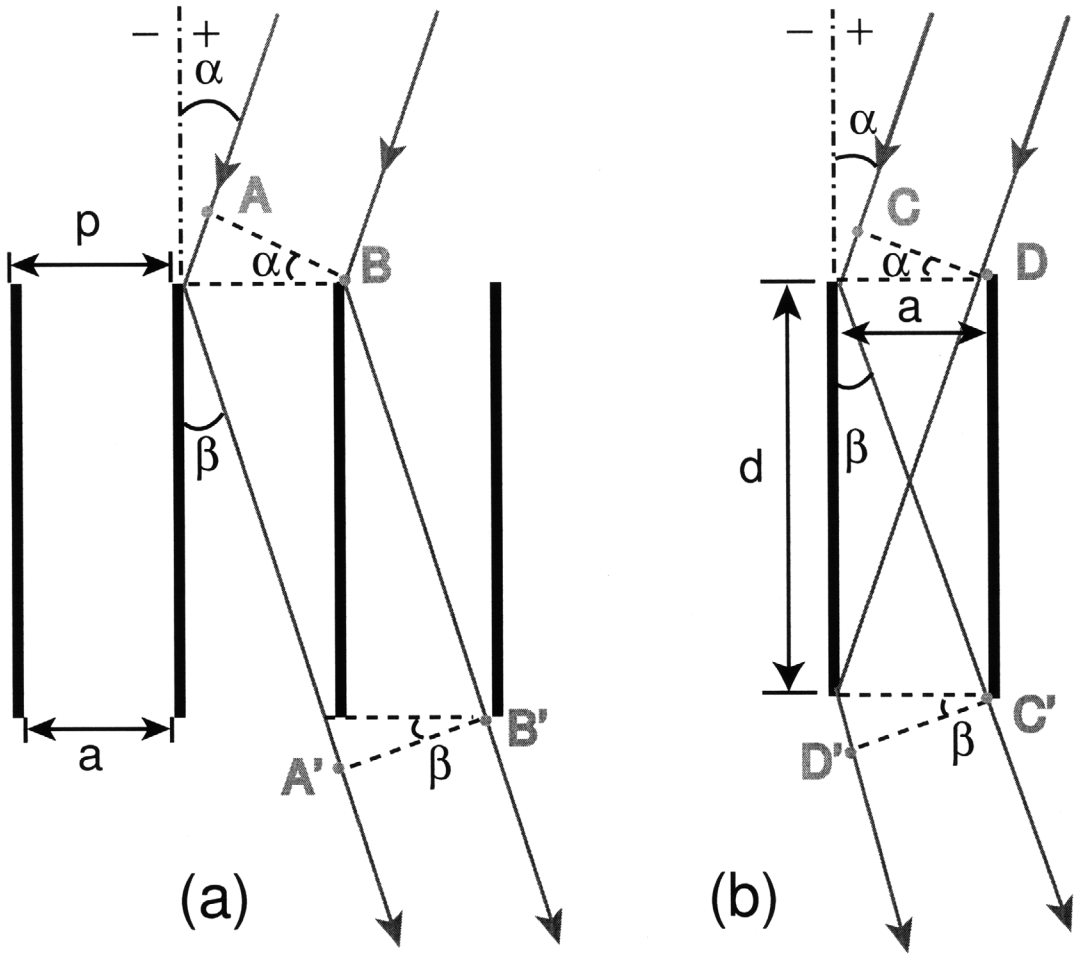


Figure 2-5: Illustrating the CAT grating geometry. (a) Ray tracing between a slit to the next. (b) Ray tracing in a long single slit. Note $\alpha > 0$ and $\beta > 0$.

Based on the sign convention shown in Fig. 2-5, the phase terms, $g$ and $f$ in Eqns. (2.7) and (2.8), should be accordingly changed to,

$$\begin{aligned} g_c &= \frac{1}{2}\left[\frac{2\pi}{\lambda}(\overline{AA'} - \overline{BB'})\right] \\ &= \frac{p\pi}{\lambda}(\sin\alpha + \sin\beta) \end{aligned} \tag{2.9}$$

and

$$\begin{aligned} f_c &= \frac{1}{2}\left[\frac{2\pi}{\lambda}(\overline{CC'} - \overline{DD'})\right] \\ &= \frac{a\pi}{\lambda}(\sin\alpha - \sin\beta), \end{aligned} \tag{2.10}$$

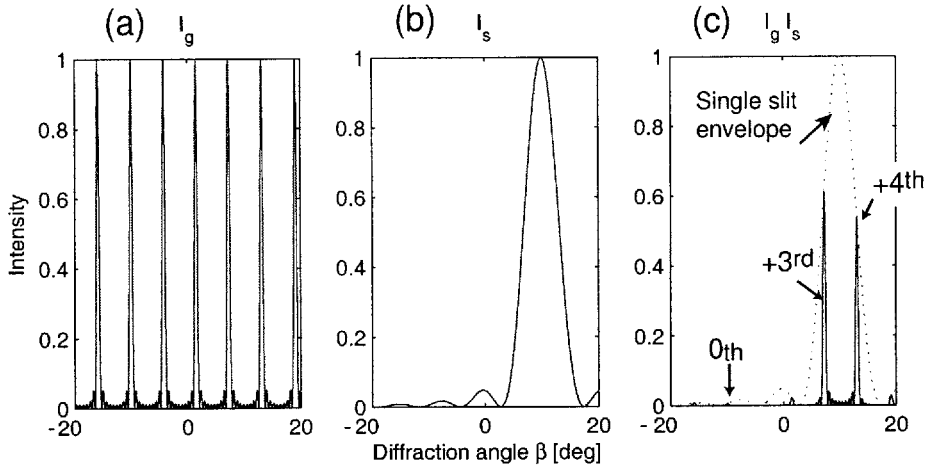


Figure 2-6: Example of the Fraunhofer diffraction from a CAT grating with $N = 10$, $\alpha = 10°$, $p = 100$ nm, $a = 80$ nm, $d = a/\tan\alpha = 0.45$ $\mu m$, and $\lambda = 10$ nm. (a) Grating interference function ($I_g$), (b) single slit diffraction function ($I_s$), and (c) overall diffraction pattern of the slits as a product of $I_g$ and $I_s$. Note the incident and diffracted beams are off of the blaze direction.

where I assume the photons undergo only one specular reflection, giving

$$d|\tan\alpha| = a, \tag{2.11}$$

where $\alpha \neq 0$. The intensity pattern then can be found by putting the new $g_c$ and $f_c$, obtained by Eqns. (2.9) and (2.10), into Eqn. (2.6). Let us then compare the diffraction pattern using the same parameters used in the previous example shown in Fig. 2-4. As we can notice in Fig. 2-6 (c), the peak is redirected from the $0^{th}$ order ($\beta = -10°$) to $3^{rd}$ and $4^{th}$ orders due to the reflection off of the grating sidewalls, although the incident and diffracted angles are not at a blaze direction.

Now let us think of a blaze condition for a CAT grating. The blaze order or direction is a particular order at which most of diffracted light is concentrated. In Eqn. (2.6), we know that the diffraction peak occurs when $f = 0$. Thus, for a CAT grating, it corresponds to when $\alpha = \beta$ from Eqn. (2.10). We then obtain the blaze condition using the grating equation, given by

$$m\lambda = 2p\sin\alpha. \tag{2.12}$$

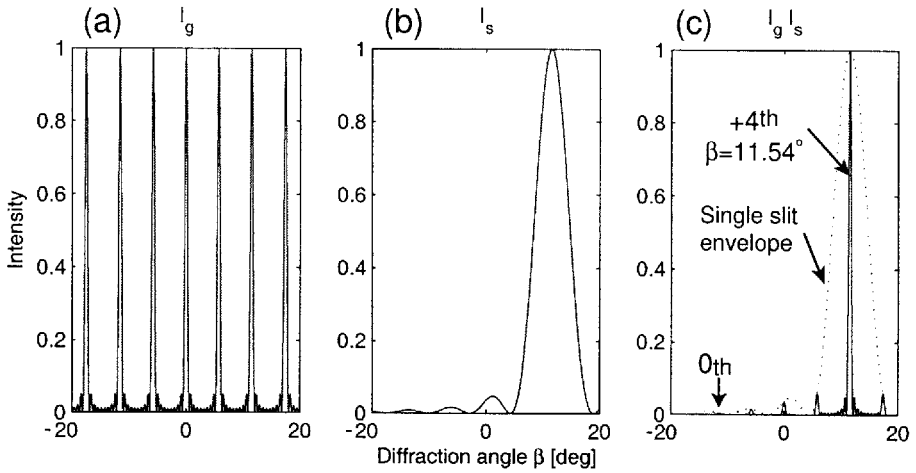


Figure 2-7: Example of the diffraction pattern from a CAT grating when the **blaze condition** is satisfied. The other parameters are the same as Fig. 2-6 except for $\alpha = 11.54°$. (a) Grating interference function ($I_g$), (b) single slit diffraction function ($I_s$), and (c) overall diffraction pattern of the slits as a product of $I_g$ and $I_s$. Note that the diffraction is enhanced only at the fourth order by blazing.

Physically thinking, the blaze condition is satisfied when the diffracted order coincides with the specular reflection off of the grating sidewall. Therefore, high diffraction efficiency is achieved at that particular direction. Let us consider the previous example again with the blaze condition

$$\alpha = \beta = \sin^{-1} \frac{m\lambda}{2p}. \tag{2.13}$$

Putting in $p = 100$ nm and $\lambda = 10$ nm, we get a blaze angle $\alpha \simeq 11.54°$ when the fourth order is to be blazed. Figure 2-7 shows the diffraction pattern when the blaze condition is satisfied at the fourth order. Suppose we want other orders to be blazed, we can find the corresponding incident angles as long as $|m\lambda/2p| < 1$.

Since the simple model for the CAT grating diffraction neglected any absorption due to the grating bars and reflectivity of the grating sidewall, we may scale the intensity distribution Eqn. (2.6) and rewrite the result as

$$I(\lambda, p, \alpha, \beta, N, a, R) = I_g I_s R(\alpha, \lambda)(a/p)^2, \tag{2.14}$$

where $R(\alpha, \lambda)$ is the specular reflectivity of silicon [2].

## 2.2 Performance Prediction

In the previous section, we examined the diffraction pattern from a CAT grating using a simple analytical model that clearly showed the blazing effect. In this section, I present more accurate simulation results using a commercial software for CAT grating efficiency analysis based on the RCWA including 3D features of a CAT gratings, material optical properties, and broadband x-ray incident beams [2,5]. The software, *Gsolver* [43], solves Maxwell equations for the diffraction of electromagnetic waves from 3D periodic grating structures. We can also design gratings based on the simulation results by changing various parameters such as the incident angle, geometry, wavelength, and material.

Recalling our target application of the CAT grating for soft x-ray spectroscopy, we performed simulations for the diffraction of x rays with 0.1 - 5 nm wavelengths from a silicon CAT grating with a period of 100 nm and an open space of 80 nm. The incident angle $\alpha$ of the x rays was set at 1.5° for high reflectivity via total external reflection on the grating sidewalls [44]. Figure 2-8 shows the simulation results of the diffraction efficiency as a function of wavelength [5]. As we can expect from the blaze condition, when $m\lambda = 2\sin\alpha$, longer wavelengths are blazed at smaller orders at a given incident angle. For much higher energies ($\lambda < 1\ nm$), where the critical angle $\theta_c$ for total external reflection is smaller than the incident angle 1.5°, the CAT grating acts as a transparent element. Thus the zero$^{th}$ order beam passes through the grating and arrives at detectors in the focal plane without very much energy loss. This feature of a CAT grating is another advantage for the next x-ray mission, IXO, with a microcalorimeter system at the focus. The transmitted $0^{th}$ order beam for higher energy photons can contribute to the microcalorimeter effective area. On the other hand, the diffracted orders from a reflection grating cannot reach the calorimeter.

In Fig. 2-9, the estimated diffraction efficiency of a CAT grating is compared to the actual efficiency of the gratings in the Chandra Observatory. For the wavelengths between ~1 - 5 nm, diffraction efficiency of the CAT grating is predicted to be higher at least four or five-fold than that of HETG and LETG. Even though the efficiency

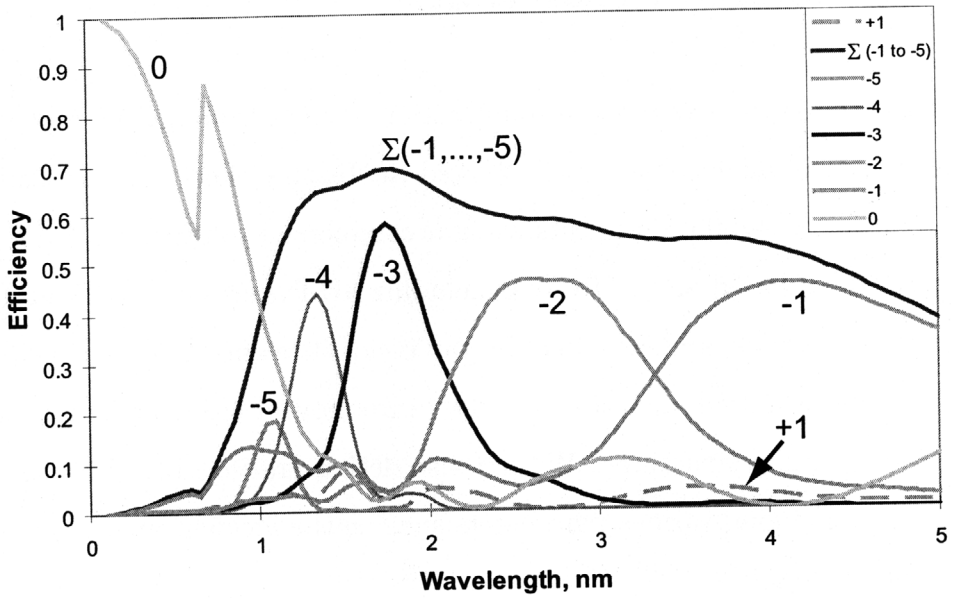


Figure 2-8: Diffraction efficiency predictions for a silicon CAT grating with $p$ = 100 nm, $d$ = 3055 nm, $a$ = 80 nm, and $\alpha$ = 1.5 nm [5]. Note that the signs of the diffracted orders are the opposite due to a different sign convention used in the software.

drops for higher energies (> 1 keV), a microcalorimeter can take over the spectroscopy function at those energy ranges because the resolving power of a calorimeter is increasing with the photon energy. Figure 2-10 shows the resolving power of various grating spectrometers and a microcalorimeter as a function of the photon energy. We can expect the best performance in spectroscopy over broadband x rays when a CAT grating spectrometer is equipped together with the microcalorimeter in the next x-ray space telescope.

## 2.3 Design Parameters and Fabrication Challenges

Based on performance requirements for spectroscopy in the IXO mission, we designed parameters for a CAT grating including general aspects of a grating such as periodicity, a duty cycle, and material, but most importantly we carefully determined the incident angle and corresponding grating height to satisfy the CAT grating geometry. Figure 2-11 shows the geometric parameters that we need to design. The grating

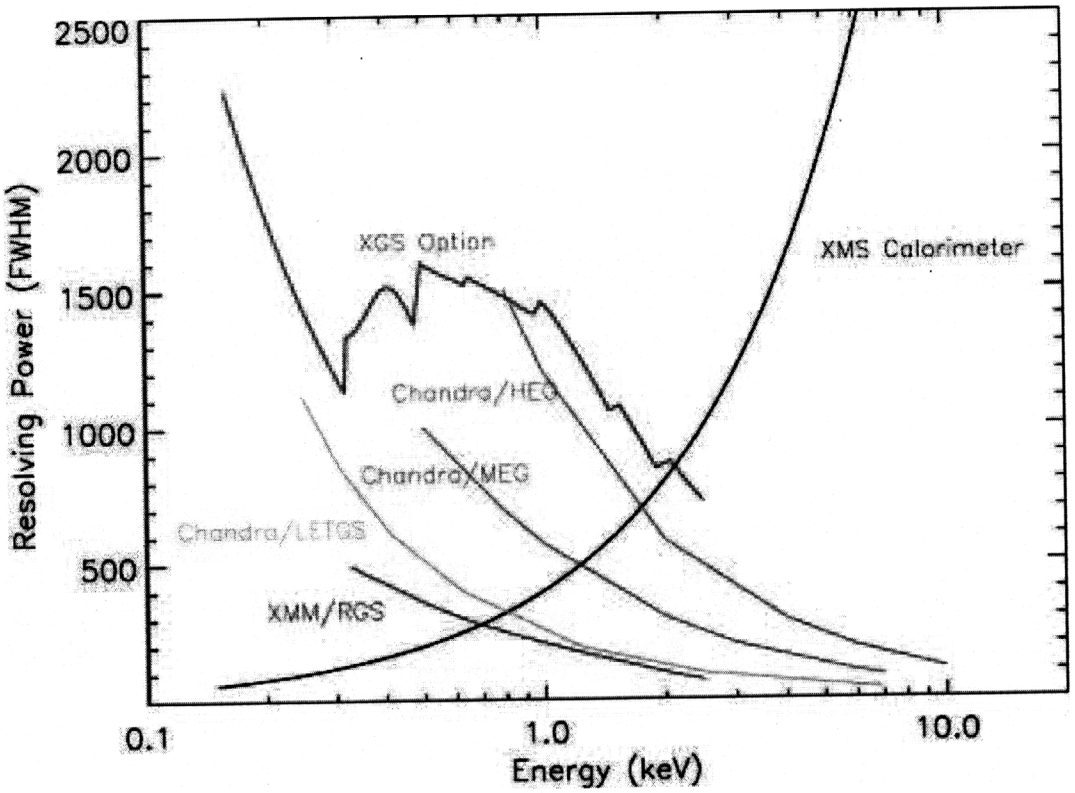


Figure 2-10: Comparison of the resolving power of the previous gratings (XMM and Chandra), a CAT grating (XGS), and a microcalorimeter (XMS) as a function of photon energy. The XGS works better in lower energies because it has a fixed $\Delta\lambda$, while XMS microcalorimeter performs better in higher energies due to a fixed $\Delta E$.

we then obtain

$$R_{TE} = \left| \frac{\cos\varphi_i - \sqrt{n^2 - \sin^2\varphi_i}}{\cos\varphi_i + \sqrt{n^2 - \sin^2\varphi_i}} \right|^2 . \tag{2.17}$$

For x-ray physics, the incident angle is often expressed with respect to the interface instead of the surface normal.

$$\theta = \pi/2 - \varphi \tag{2.18}$$

Assuming $\theta$ is very small, we can write the reflectivity as

$$\begin{aligned} R_{TE} &= \left| \frac{\sin\theta - \sqrt{(1-\delta+i\beta)^2 - \cos^2\theta}}{\sin\theta + \sqrt{(1-\delta+i\beta)^2 - \cos^2\theta}} \right|^2 \\ &\cong \left| \frac{\theta - \sqrt{(1-\delta+i\beta)^2 - (1-\theta^2)}}{\theta + \sqrt{(1-\delta+i\beta)^2 - (1-\theta^2)}} \right|^2 \end{aligned} \tag{2.19}$$

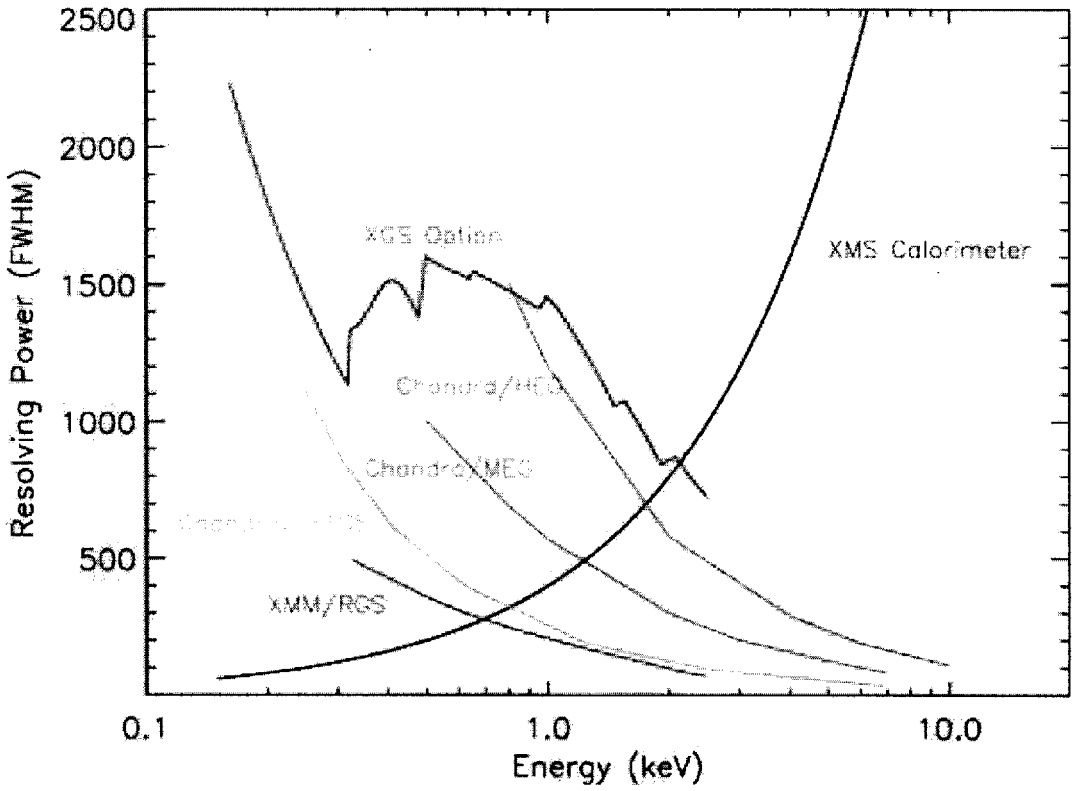


Figure 2-10: Comparison of the resolving power of the previous gratings (XMM and Chandra), a CAT grating (XGS), and a microcalorimeter (XMS) as a function of photon energy. The XGS works better in lower energies because it has a fixed $\Delta\lambda$, while XMS microcalorimeter performs better in higher energies due to a fixed $\Delta E$.

we then obtain

$$R_{TE} = \left| \frac{\cos\varphi_i - \sqrt{n^2 - \sin^2\varphi_i}}{\cos\varphi_i + \sqrt{n^2 - \sin^2\varphi_i}} \right|^2 . \tag{2.17}$$

For x-ray physics, the incident angle is often expressed with respect to the interface instead of the surface normal.

$$\theta = \pi/2 - \varphi \tag{2.18}$$

Assuming $\theta$ is very small, we can write the reflectivity as

$$\begin{aligned} R_{TE} &= \left| \frac{\sin\theta - \sqrt{(1-\delta+i\beta)^2 - \cos^2\theta}}{\sin\theta + \sqrt{(1-\delta+i\beta)^2 - \cos^2\theta}} \right|^2 \\ &\cong \left| \frac{\theta - \sqrt{(1-\delta+i\beta)^2 - (1-\theta^2)}}{\theta + \sqrt{(1-\delta+i\beta)^2 - (1-\theta^2)}} \right|^2 \end{aligned} \tag{2.19}$$

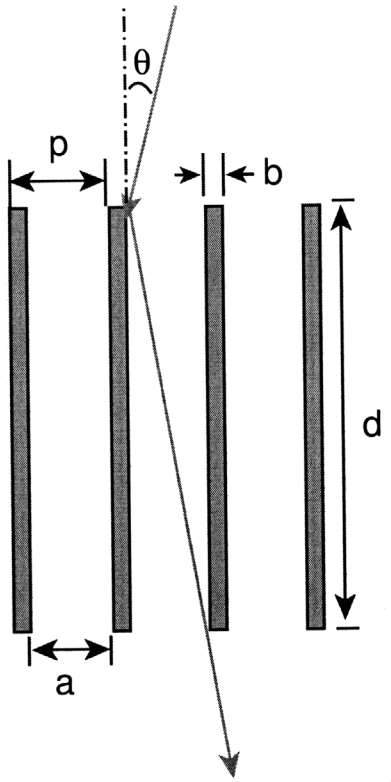


Figure 2-11: Design parameters for a CAT grating.

Since $\delta$ and $\beta \ll 1$ for x rays, we get

$$R_{TE} \cong \left| \frac{\theta - \sqrt{\theta^2 - 2\delta + 2i\beta}}{\theta + \sqrt{\theta^2 - 2\delta + 2i\beta}} \right|^2 . \tag{2.20}$$

More detailed calculations and a TM-wave example can be found in Ref. [45]. When $\theta^2 \cong 2\delta$, the reflectivity approaches 1, which means the incident beam is reflected from the surface without much transmission or absorption. This phenomenon in x-ray physics is called total 'external' reflection. A critical angle $\theta_c$ for total external reflection is defined as

$$\theta_c \equiv 2\delta. \tag{2.21}$$

For example, silicon at 1 keV photons has $\delta = 4.47 \times 10^{-4}$ [49] and the critical angle is only about 1.7°. Because $\delta$ decreases as the x-ray energy increases, we need shallower incident angles for higher energy photons for a high reflectivity. In this thesis, I will use a grazing incidence angle of $\theta = 1.5°$ that is in the typical range of the critical

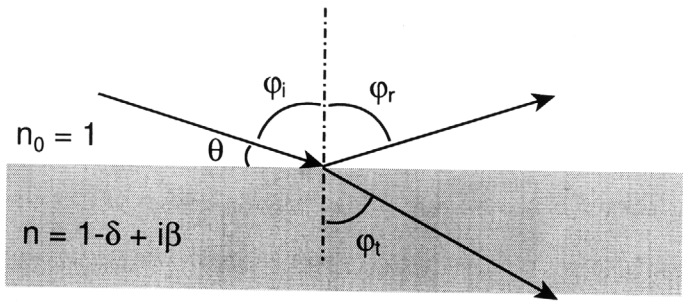


Figure 2-12: Reflection and transmission at an interface between vacuum and a medium with $n = 1 - \delta + i\beta$.

angle ($\theta_c \sim 1 - 2°$) for the soft x rays of interest.

A grating period is determined based on the required dispersion angle and resolving power for the target energy or wavelength ranges. We also need a large grating area because the resolving power depends on the grating area as well. For the soft x rays with wavelength of 0.1 - 10 nm, 100 to 200 nm-period gratings are preferred to provide a sufficient dispersion angle at the detector at a distance of $\sim 10 - 20$ m. In order to pattern the required grating with a fine pitch, I have used the Nanoruler operating with an Ar-ion laser with 351.1 nm wavelength. As explained in the previous chapter, there is a limit for the minimum period at one-half of the laser wavelength unless special tricks are used. Chang [27] recently has demonstrated an overlay technique for spatial frequency multiplication. If required, 100 nm-period CAT gratings would be possible to fabricate using the process Chang has developed.

The duty cycle (DC) -the ratio of a grating bar width with respect to the period- should be minimized for a high throughput of diffracted beams as long as the structure is stable. As we can see from Eqn. (2.14), the diffraction efficiency is scaled by a square of (1 - DC). Although I have not done any structural analysis, a duty cycle of 20% would be a practical starting point.

Assuming $p = 100$ nm, $\theta = 1.5°$, and $b/p = 0.2$, we obtain the grating height

$$d = a/\tan\theta \cong 3\ \mu\text{m}. \tag{2.22}$$

Then the aspect ratio of a grating bar ($d/b$) is required to be 150. It is very challenging to fabricate such a high aspect-ratio nano-scale structure using conventional

Table 2.1: Design parameters for CAT gratings.

| period (nm) | 100 | 200 |
|---|---|---|
| Incident angle, $\theta$ | 1.5° | 1.5° |
| Duty cycle | 0.2 | 0.2 |
| Bar width, b (nm) | 20 | 40 |
| Bar Height, d ($\mu$m) | 3 | 6 |
| Aspect ratio, d/b | 150 | 150 |
| Sidewall roughness (nm) | 2 | 2 |

microfabrication techniques. Moreover, the grating sidewall has to be very smooth (on the order of a nanometer) for the sake of high reflectivity. Another challenging requirement for the CAT grating fabrication is a free-standing structure in order to avoid any absorption which leads to attenuated diffraction. Table 2.1 summarizes the geometric design parameters for CAT gratings with 100 nm and 200 nm periods.

Lastly, let us consider material selection for the CAT gratings. Silicon has excellent mechanical properties for microstructures [50] and processing techniques have been developed relatively well for various applications. In particular, silicon has a very large etch anisotropy between different crystallographic planes [28], which enables us to form ultra-high aspect-ratio structures. As shown in the previous section, performance prediction for a silicon CAT grating with 100 nm period also met or exceeded the requirements for the next x-ray mission. Therefore, I have used silicon for the CAT grating fabrication.

# Chapter 3

# Fabrication Process Development for CAT Grating Prototypes

In this chapter I will present a fabrication process for an initial prototype CAT grating with a relatively large period of 574 nm. This initial prototype provides us with not only fabrication feasibility but also proof of the concept for the CAT grating via x-ray tests. The CAT grating has to be in a thin membrane and the individual grating bars have a high aspect ratio of 150 for the CAT grating geometry. The required straight and ultra-high aspect ratio free-standing structures were achieved by anisotropic etching of ⟨110⟩ SOI wafers in potassium hydroxide (KOH) solution. To overcome structural weakness, chromium was patterned as a reactive-ion etch (RIE) mask to form a support mesh. The grating with a period of 574 nm was written by scanning-beam interference lithography (SBIL) which is based on the interference of phase-locked laser beams. Free-standing structures were accomplished by etching the handle and device layers in tetramethylammonium hydroxide (TMAH) and KOH solution, respectively, followed by hydrofluoric acid (HF) etching of the buried oxide. To prevent collapse of the high aspect ratio structures caused by water surface tension during drying, the devices were dried in a critical point dryer after dehydration of the sample in pure ethanol. I have successfully fabricated 574 nm-period free-standing gratings with support mesh periods of 70, 90 and 120 $\mu$m in a 10 $\mu$m-thick membrane on ⟨110⟩ SOI wafers. The size of a single die is 10 $\times$ 12 mm$^2$ divided into four

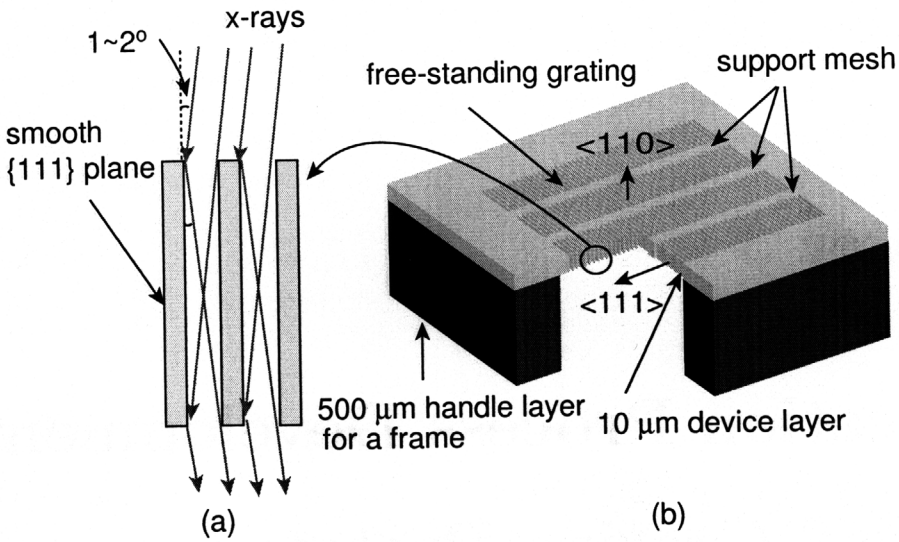


Figure 3-1: (a) Concept of the critical angle transmission (CAT) grating. The incoming x rays have a small graze angle so that they will be strongly diffracted in the specular reflection direction due to total external reflection on the smooth sidewalls. (b) Schematic design for the CAT grating prototype utilizing ⟨110⟩ single crystal silicon, which can be etched with vertical and atomically smooth {111} sidewalls.

$3 \times 3.25$ mm$^2$ windows. The aspect ratio of a single grating bar achieved is about 150, as required for the CAT grating configuration.

## 3.1 Prototype Design and Fabrication Methods

Based on the CAT grating configuration discussed in Chapter 2, I designed geometric parameters for a prototype CAT grating with a period of 574 nm. With a 10 $\mu$m thick device layer, the grating bar width was determined to be 67 nm in order to satisfy the requirement for the aspect ratio of 150. A free-standing structure can be attained by etching both sides of an SOI wafer, followed by etching the buried oxide. Figure 3-1 illustrates the CAT grating concept and schematic design of a prototype on a SOI wafer with 10 $\mu$m device layer. The support mesh and frame are mechanical structures holding the free-standing gratings.

In order to build high aspect ratio microstructures, one may consider two different approaches such as deep reactive ion etching (DRIE) and wet anisotropic etching. Although a DRIE process provides relatively vertical (90±2°) etch profile with fast

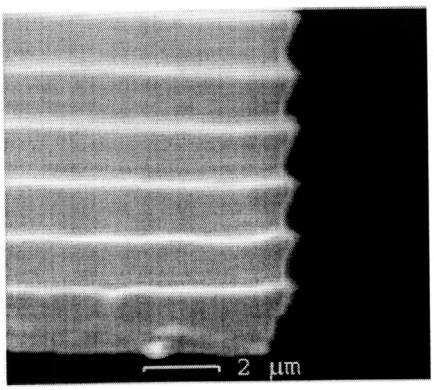


Figure 3-2: Micrograph of a scalloping etch profile produced by a DRIE process [52].

etch rates, the etch profile suffers from scalloping due to nature of an alternating process of etching and protective layer deposition [51, 52]. Figure 3-2 shows the typical etch profile after a DRIE process [52]. On the other hand, wet anisotropic etching with KOH solution has excellent selectivity between $\langle 110 \rangle$ and $\langle 111 \rangle$, and $\{111\}$ planes are atomically smooth [8, 28, 32, 53]. Aligning the grating pattern to the $\{111\}$ planes, we can obtain a vertical etch profile with extremely smooth $\{111\}$ sidewalls. Therefore, we used KOH etching to produce the high aspect ratio structure required for the CAT grating geometry.

### 3.1.1 Anisotropic Etching and Surface Roughness

A simple KOH etch process with the 574 nm-period grating pattern on $\langle 110 \rangle$ silicon wafers was tested to assure a vertical etch profile and to measure sidewall roughness after etching. The process flow is shown in Fig. 3-3. A thin (30 nm) silicon-rich nitride (SiN) layer was deposited on a bulk $\langle 110 \rangle$ silicon wafer by low pressure chemical vapor deposition (LPCVD) to serve as a KOH etch mask. 45 nm of antireflection coating (ARC) (i-CON, Brewer Science Inc.) and 700 nm of photoresist (PFI-88a7, Sumitomo Corp.) were spin-coated for interference lithography. The interference fringe direction was roughly aligned to the wafer flat at $\langle 111 \rangle$ orientation using a protractor. The grating pattern in the photoresist was developed in a positive resist developer (OPD-262, Fuji Film) and transferred into the ARC and SiN with oxygen and $CHF_3$ RIE, respectively. After stripping the ARC and resist with an RCA clean

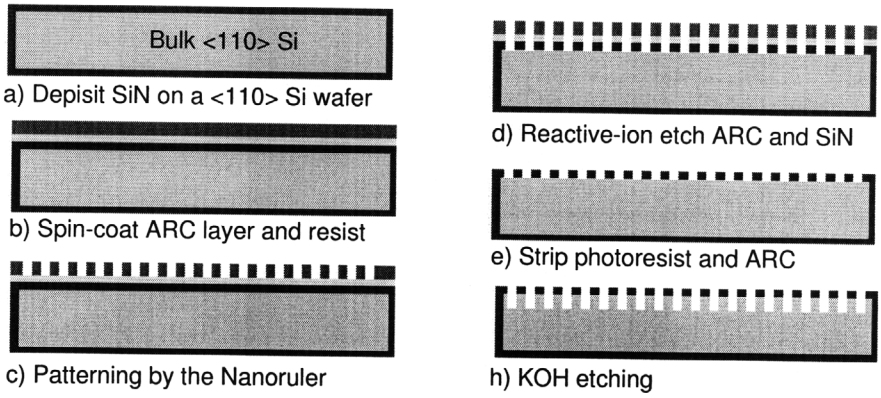


Figure 3-3: Fabrication process for the sidewall roughness measurement test.

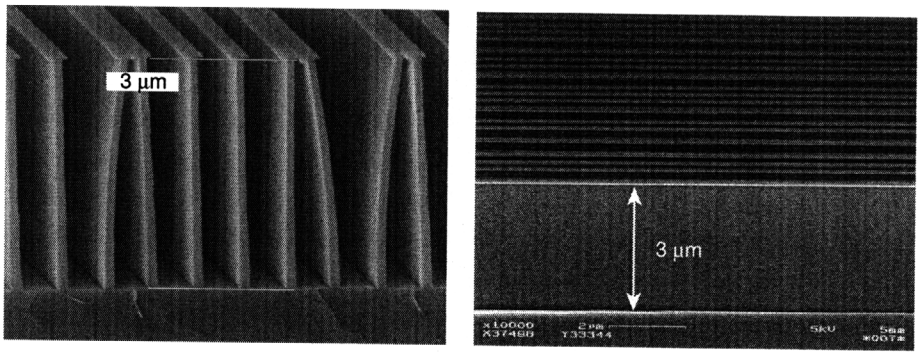


Figure 3-4: A test sample etched for roughness measurement of the etch grating sidewall. (a) cleavage across the grating bars and (b) cleavage along the grating planes.

(hydrogen peroxide:ammonium hydroxide:water = 1:1:5), the substrate was etched in 40 % KOH solution with 1 % isopropanol (IPA) at 80 °C. The IPA was mixed to improve the surface smoothness even though it degraded the etch anisotropy. Figure 3-4 shows cross-sections of a sample etched down to about 3 $\mu$m. I cleaved the sample along the grating direction (Fig. 3-4(b)) and measured sidewall roughness using atomic force microscopy (AFM). An image scanned with AFM is shown in Fig. 3-5. The root-mean-square (RMS) roughness of the sidewall is found to be less than 1 nm in a scanned area of around 65 $\times$ 65 nm$^2$.

In order to find roughness in larger areas, we etched* through a $\langle 110 \rangle$ wafer with a 5 $\mu$m $\times$ 10 mm slot pattern aligned with the $\langle 111 \rangle$ orientation. The RMS roughness of the sidewall was also less than 1 nm in an area of 10 $\times$ 10 $\mu$m$^2$ [Fig. 3-6].

*Note: etched in 50 wt% KOH at 50 °C

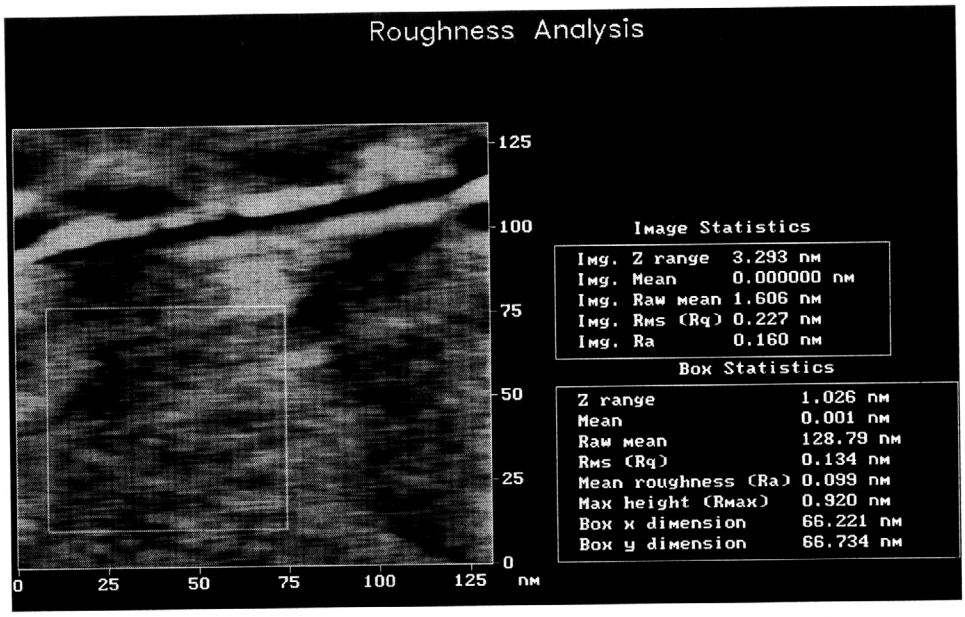


Figure 3-5: AFM measurement of the grating sidewall roughness of the test sample in Fig. 3-4.

In this section, I presented preliminary test results for KOH etching and sidewall roughness of etched $\langle 111 \rangle$ surfaces over areas of $65 \times 65$ nm$^2$ and $10 \times 10$ $\mu$m$^2$. The results provide us with feasibility of utilizing KOH etching to the fabrication of the CAT grating prototypes. In the following sections, I will describe overall process development for the CAT grating prototypes.

## 3.2 Patterning

Our substrates were 100 mm-diameter $\langle 110 \rangle$ SOI wafers (Ultrasil, CA) with a 10 $\pm 0.5$ $\mu$m device layer, 2 $\pm 0.1$ $\mu$m buried oxide, and 500 $\mu$m handle layer. The wafer has two flats in the $\langle 111 \rangle$ directions with a $\pm 0.2°$ tolerance. The $\{111\}$ planes are to be aligned with grating bars to form mirror-like sidewalls. The thermally grown buried oxide will act as an etch stop for the anisotropic etch of the handle layer from the backside. A thin (40 nm) silicon-rich nitride layer was deposited on the substrate by LPCVD to serve as a wet etch mask. Using an electron beam evaporator, 30 nm of chromium was deposited as a reactive ion etch mask to form the support mesh [Fig. 3-7(b)].

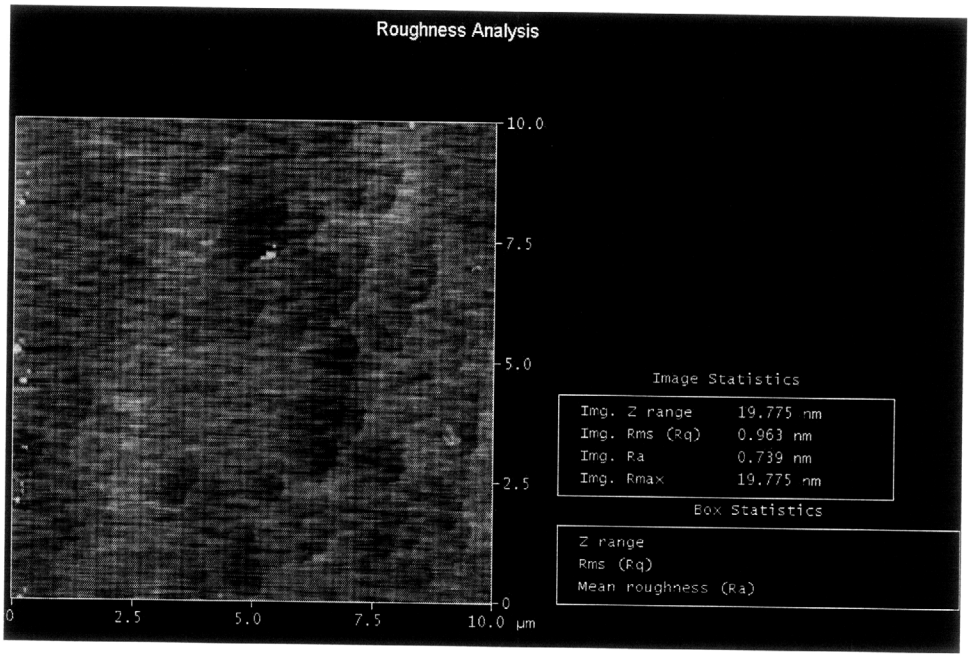


Figure 3-6: AFM image of a 10 × 10 $\mu m^2$ area of a KOH etched ⟨111⟩ plane. The sample was etched with a 5 $\mu$m × 10 mm slot pattern mask on a ⟨110⟩ wafer and snapped along the trench.

The Cr layer was patterned by contact lithography and wet etching in perchloric acid CR-7 (Cyantek, CA) [Fig. 3-7(c)]. We patterned support structures with 70, 90 and 120 $\mu$m pitches and a wide cross which was aligned with the cross pattern on the backside to divide the large (10 × 12 $mm^2$) area of the membrane into four parts. Figure 3-11(a) shows an etched Cr RIE mask pattern with a 70 $\mu$m pitch.

On top of the support mesh, 150 nm of anti-reflection coating (ARC) (XHRiC-11, Brewer Science Inc.) and 700 nm of photoresist (PFI-88a7, Sumitomo Corp.) were spin-coated for interference lithography. The ARC thickness was designed to minimize reflectivity at the resist/ARC interface on the SiN region as well as on the Cr support area, otherwise the grating pattern in the resist would not be developed completely for both of the regions. Figure 3-8 (b) shows the resist pattern problem on the SiN layer when the layer design was optimized only for the Cr/SiN support region. On the other hand, the ARC layer optimized only for SiN area resulted in a pattern collapse problem in Cr/SiN area due to over-exposure as shown in Fig. 3-9(b). Even

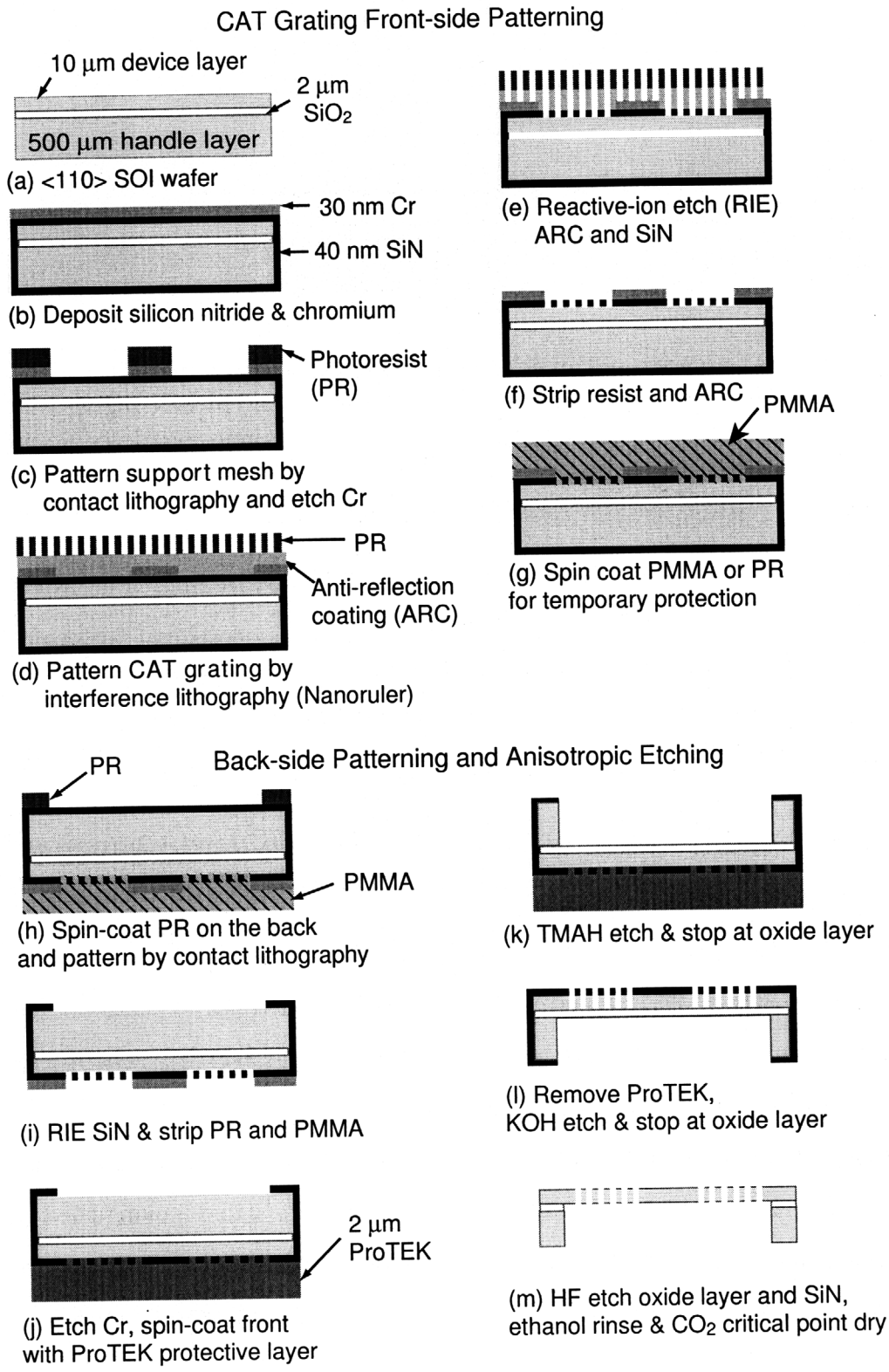


Figure 3-7: CAT grating fabrication process, (a)-(g): front-side patterning to form SiN mask of the grating and support mesh, (h)-(k): backside patterning to form the membrane and frame, (l)-(m): KOH etching, HF etching and supercritical drying to form the high aspect ratio free-standing grating.

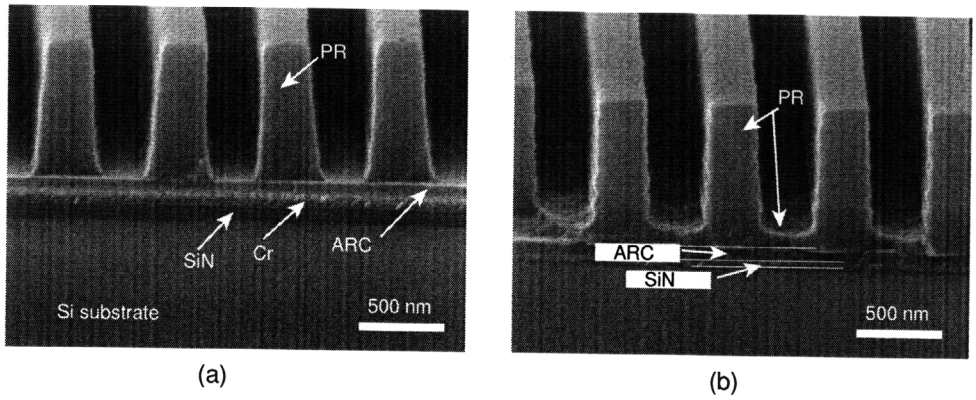


Figure 3-8: SEM micrographs of 574 nm-period grating patterns in the photoresist on a Cr-patterned wafer. (a) Cr/SiN support region and (b) SiN region where the grating pattern will be transferred. The photoresist was not completely exposed in the case (b) due to a bad layer design.

though the grating pattern looks good between the support lines [Fig. 3-9(c)], the interface between the support and grating regions has the occasional pattern collapse problem [Fig. 3-9(a)]. This interface problem will be directly transferred into the SiN layer during RIE steps and end up causing problems during KOH etching. Therefore, it is important to determine an appropriate ARC thickness for both regions. Based on simulation shown in Fig. 3-10, I determined the ARC layer thickness at which reflectivity at the resist/ARC interface is minimized for the Cr/SiN and SiN regions.

The fine period (574 nm) grating was written by scanning-beam interference lithography (SBIL) [54, 55] which is based on the interference of phase-locked mm-sized laser beams of 351 nm wavelength [Figs. 3-7(d) and 3-11(b)]. The interference fringe direction was aligned with the wafer flat using a microscope mounted on the vertical optical bench of the SBIL system looking down on the wafer flat. The wafer flat was aligned to have a fixed position in the microscope when moving the scanning stage along the fringe direction. The grating pattern in the photoresist was developed and transferred into the ARC and silicon nitride with reactive ion etching (RIE). The ARC was etched using $O_2$ plasma and the silicon nitride etched using $CF_4$+$O_2$ plasma [Figs. 3-7(e), 3-11(c) and 3-11(d)]. An RCA clean removed the photoresist and ARC [Fig. 3-7(f)]. The front-side was then spin-coated with PMMA or thick photoresist to protect the front pattern during the following backside patterning process [Fig.

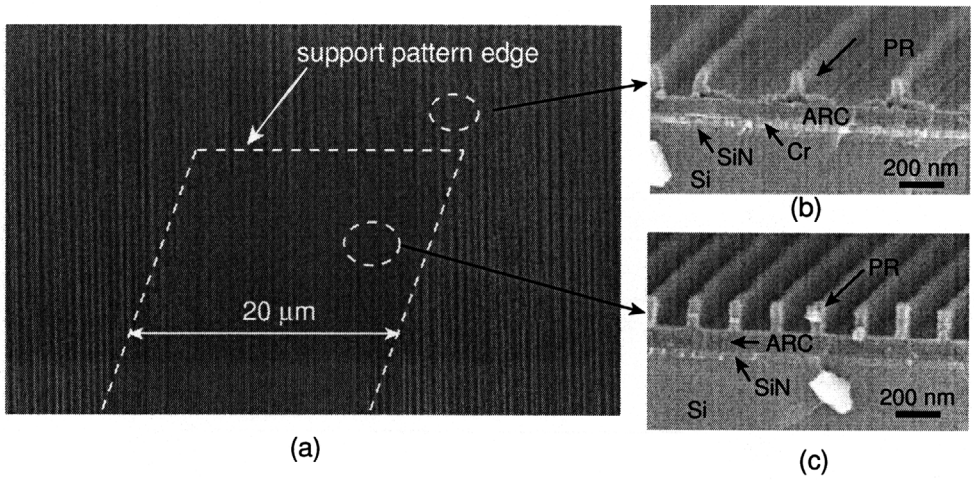


Figure 3-9: SEM micrographs of 200 nm-period grating patterns in the photoresist on a Cr-patterned wafer. For a convenient SEM inspection, the grating was intentionally patterned with 90 ° rotation. (a) Top down view showing a pattern collapse problem in Cr/SiN support region and its interface with the grating region. (b) The photoresist pattern on top of Cr/SiN is collapsed during developing. (b) The 200 nm-period grating pattern on top of SiN is good.

3-7(g)].

The backside was patterned by contact lithography and RIE to serve as a hard mask for tetramethylammonium hydroxide (TMAH) etching to form a thin membrane [Figs. 3-7(h) and 3-7(i)]. The pattern is a simple window shape with a 12 × 10 $mm^2$ outer release frame and cross in the middle. After removing the photoresist, PMMA, and Cr, the wafer is ready for anisotropic wet etching [Fig. 3-11(e)]. The fine nitride grating linewidth was about 200 nm as shown in Fig. 3-11(f).

## 3.3 Anisotropic Wet Etching

In order to cover the front side pattern during a long backside TMAH etching, 2 $\mu$m of protective layer with a primer (ProTEK, Brewer Science Inc.) was spin-coated on top of the device layer [Fig. 3-7(j)]. Because the selectivity between Si and $SiO_2$ in TMAH solutions is very high [28], the buried oxide is a good etch stop. The etch rate for the {110} plane was about 1.4 $\mu$m/min in 25% TMAH at 90°C. Figure 3-12 shows top and bottom views of a single device after TMAH etching. We can see

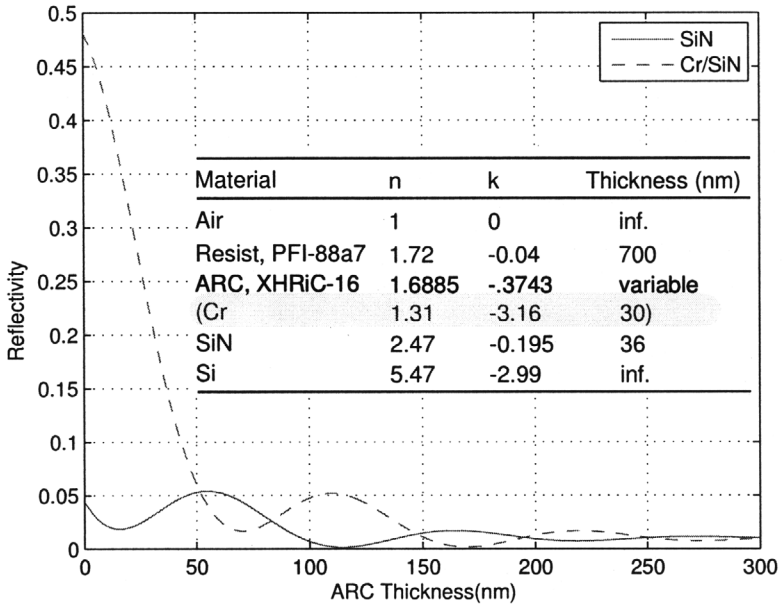


Figure 3-10: Simulated reflectivity at the resist/ARC interface as a function of ARC thickness. The solid line represents the SiN/Si stacked region and the dashed line does the case of Cr/SiN/Si area. The inset table shows the material stack. About 150 nm of ARC minimizes the reflectivity for both regions.

through the thin (10 $\mu$m) silicon layer which is partially transparent with a red color. Three quadrants of the device have the fine grating with support mesh, but the top right quadrant has the support structure only for test purposes. The backside nitride mask had a square window shape, but the etched profile in Fig. 3-12(b) shows etch anisotropy in TMAH solution. The width of the outer frame and the central cross masking were designed to be wide enough to account for the expected undercut. The thin bridges at the corners prevent the device from detaching during wet processing. The silicon membranes tend to buckle slightly due to compressive stress (~300 MPa) of the buried oxide layer, but flatten at the end of the process after HF etching. We found no evidence of the stress causing any problem during the KOH etch for 574 nm-period CAT grating prototypes. However, the stress may cause a stiction problem during HF releasing of finer pitch CAT gratings, which will be discussed in the next chapters.

After removing the ProTEK with solvent and a short oxygen plasma etch, the grating was anisotropically etched in 50 wt% KOH/water solution at 50°C for 55

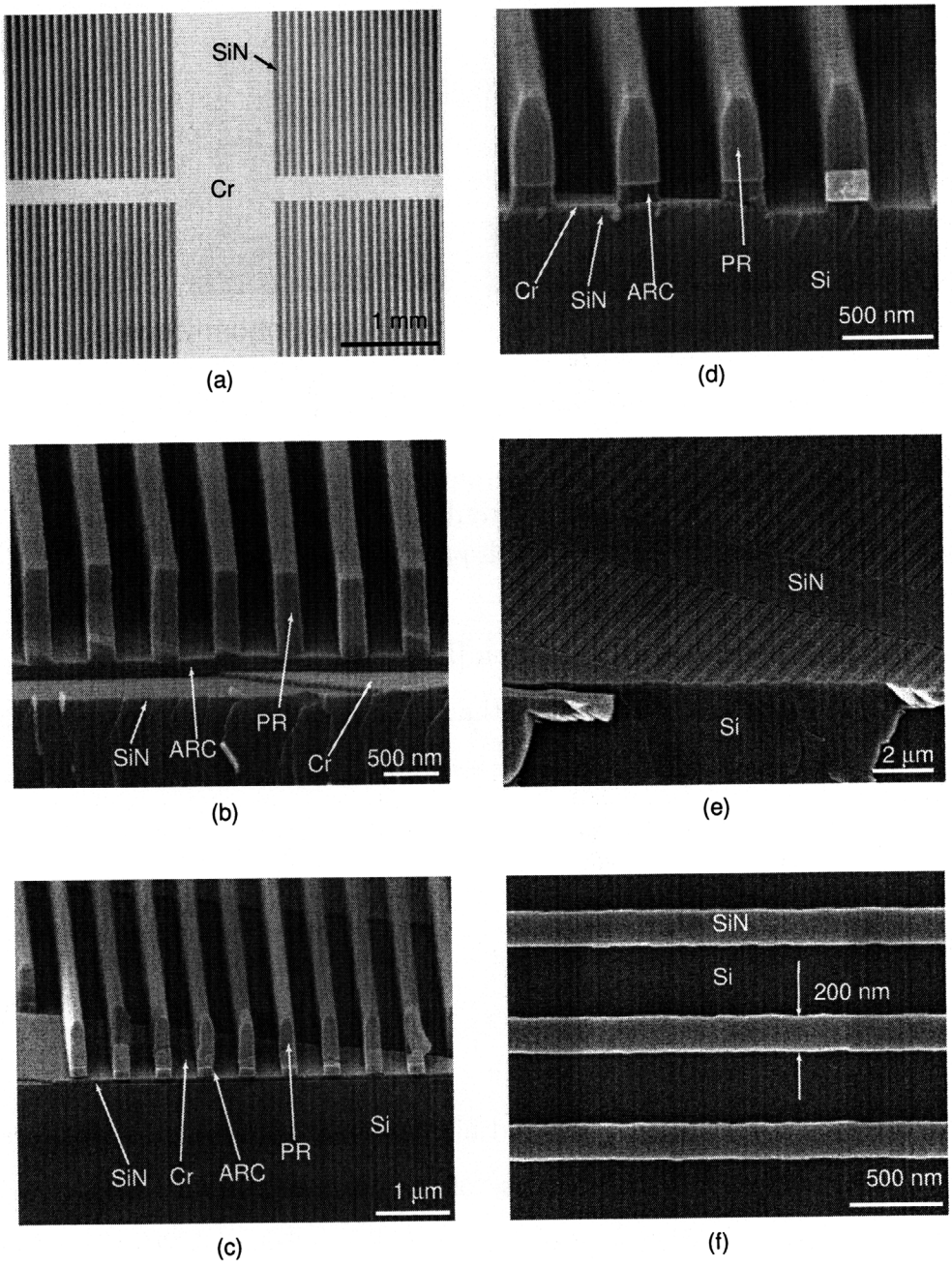


Figure 3-11: Micrographs of the patterning steps. (a) Cr support mesh pattern with 70 $\mu$m period on the SiN layer. (b) Photoresist pattern of the fine grating after scanning beam interference lithography. (c) Pattern transferred to ARC. (d) Pattern transferred to SiN. (e) SiN pattern of the fine grating and the support mesh after removing PR, ARC and Cr. (f) Top view of SiN fine grating lines between 70 $\mu$m-period support meshes on a SOI wafer to be etched in the KOH solution. Note (b)-(d) are taken from a $\langle 100 \rangle$ test wafer with narrow support mesh (period = 7 $\mu$m) to show the support mesh and the fine grating in a single image.

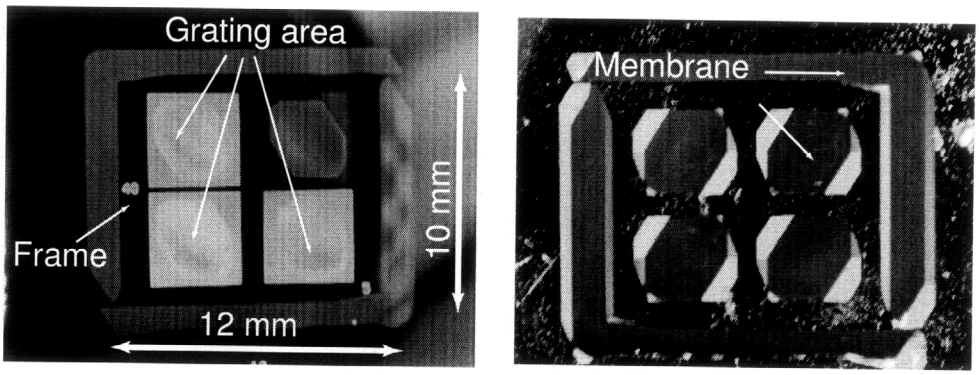


(a) Top view (b) Bottom view

Figure 3-12: Photographs of one grating unit after TMAH Etching. The bright parts in (a), including four grating areas and the outer frame boundary, are the membranes of 10 $\mu$m of Si and 2 $\mu$m of $SiO_2$ etched from the back. The grating areas, except for the top right quadrant, are brighter due to diffraction from the SiN grating. The top right quadrant has only the support mesh pattern for test purposes.

minutes to etch through the 10 $\mu$m silicon [Fig. 3-7(l)]. The loss of the nitride mask and buried oxide is expected to be less than 1 nm and 25 nm, respectively [28, 37]. KOH etching is the most challenging process step because the anisotropy or etch rate ratio is very sensitive to temperature, KOH concentration, additives, and so forth. We will discuss these variances in Section 3.5.

## 3.4 Releasing

After KOH etching, the buried oxide and nitride mask were removed by a 5 minute etch in concentrated (48%) HF. Because of the high aspect ratio and rinse water surface tension, drying in air leads to sticking problems. Figure 3-13(a) shows stiction after air drying even though the aspect ratio of the grating bar is only about 20. Considering the goal aspect ratio of 150, I instead used a liquid carbon dioxide critical point dryer (Tousimis, MD) after dehydration with pure ethanol [Fig. 3-7(m)]. The dehydration process was done by a gradual increase of ethanol concentration from 50 % to 100 %. Figures 3-13(c) and 3-13(d) show that the stiction problem was solved by critical point drying. Special care had to be taken during transfer of the sample in order to prevent drying in air.

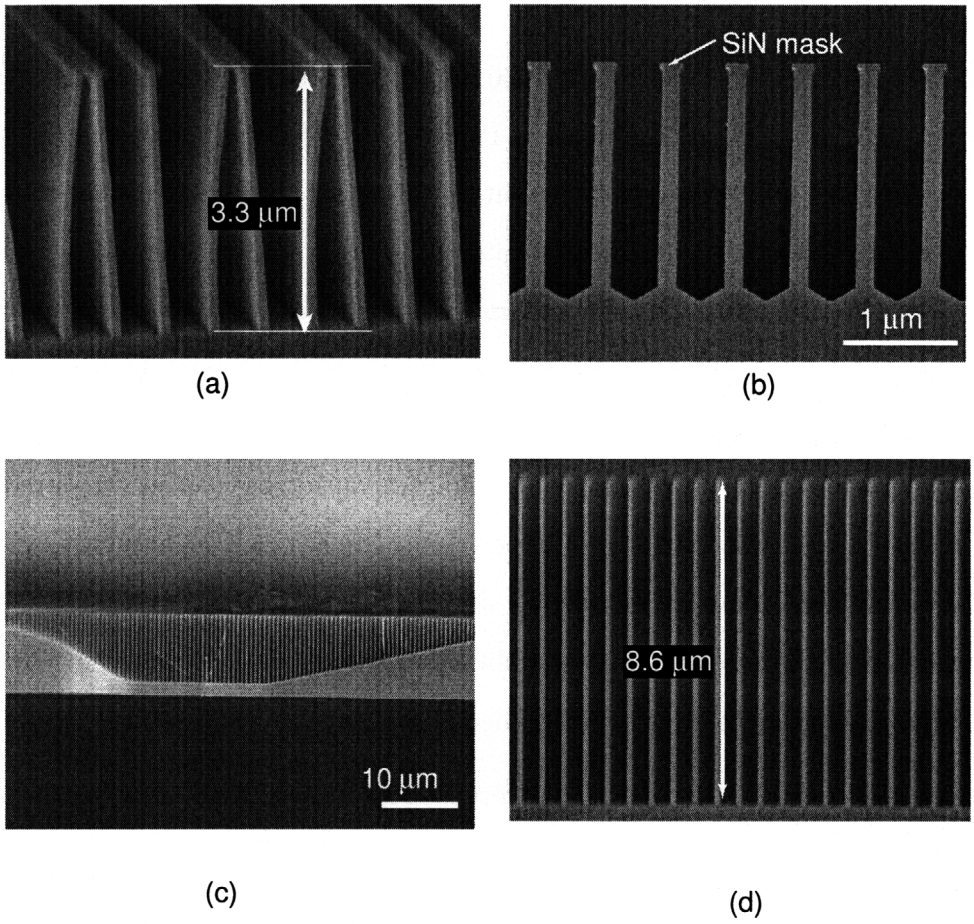


Figure 3-13: Electron micrographs after KOH etching. (a) Etched for 1.5 min in 40 wt% KOH with isopropyl alcohol (IPA) at 80 °C and dried in air. Alcohol addition made the etch front flat, but reduced the anisotropy. Air drying caused a stiction problem. (b) Etched for 1 min in 45 wt% KOH at 80 °C and dried in air. There is considerable lateral etching (undercut). (c) Cross sectional view of a slightly underetched sample in 50 wt% KOH at 60 °C and dried by a supercritical point dryer (d) Close view of (c). A low temperature in a high KOH concentration produced a flat etch front, as compared to (b).

## 3.5 Discussion and Summary

First attempts to etch through the 10 $\mu$m silicon device layer resulted in only partial success or totally destroyed grating lines [Fig. 3-14(a)] due to insufficient etch anisotropy and overetching in 45 wt% KOH at a high temperature (80°C), although Kendall [32] achieved an anisotropy of 600 under similar etching conditions. In order to understand that etching condition, a 1 min KOH etch was performed in 45 wt% KOH at 80°C. The etch profile is shown in Fig. 3-13(b). The vertical etch rate ($R_{110}$) was 1.86 $\mu$m/min and the lateral etch rate ($R_{111}$) was 26 nm/min. The anisotropy ratio, $R_{110}/R_{111}$, is about 70, which is much lower than that reported in previous literature. [28, 32, 39, 56] One explanation might be misalignment between the grating pattern and the crystal direction. However, Krause *et al.* [41] also showed an anisotropy dependence on the groove width. An anisotropy of 70 for our 0.37 $\mu$m groove width agrees well with their experimental behavior. In any case, given the nitride linewidth of 0.2 $\mu$m [Fig. 3-11(f)] and the low anisotropy in the 80°C etching condition above, the grating bars will thin away and the silicon nitride mask will detach before the oxide etch stop is reached.

Kim *et al.* [57] and Hölke *et al.* [39] reported an increase in the etch rate ratio in high KOH concentrations and at low temperatures. With 50 wt% KOH at 50°C, we achieved an improved anisotropy ratio of about 125. While an apex formed at the etch front in a high concentration at a high temperature as shown in Fig. 3-13(b), with an alcohol additive or at a low temperature below 60 °C, the shape of the etch front changed to a flat as shown in Figs. 3-13(a) and 3-13(d). Once an apex is formed the vertical etch rate decreases and thus the anisotropy degrades. However, although a sufficient anisotropy was achieved, etching was not uniform over the whole grating area, as shown Fig. 3-14(b). Stirring with a magnet bar and ultrasonic agitation did not help much, or resulted in unfavorable damage to the membrane as Kaminsky [56] has observed. Because KOH etching produces an abundance of $H_2$ bubbles, trapping of bubbles between the grating bars might intermittently interfere with the reaction. Samples immersed horizontally (facing upward) resulted in better uniformity than

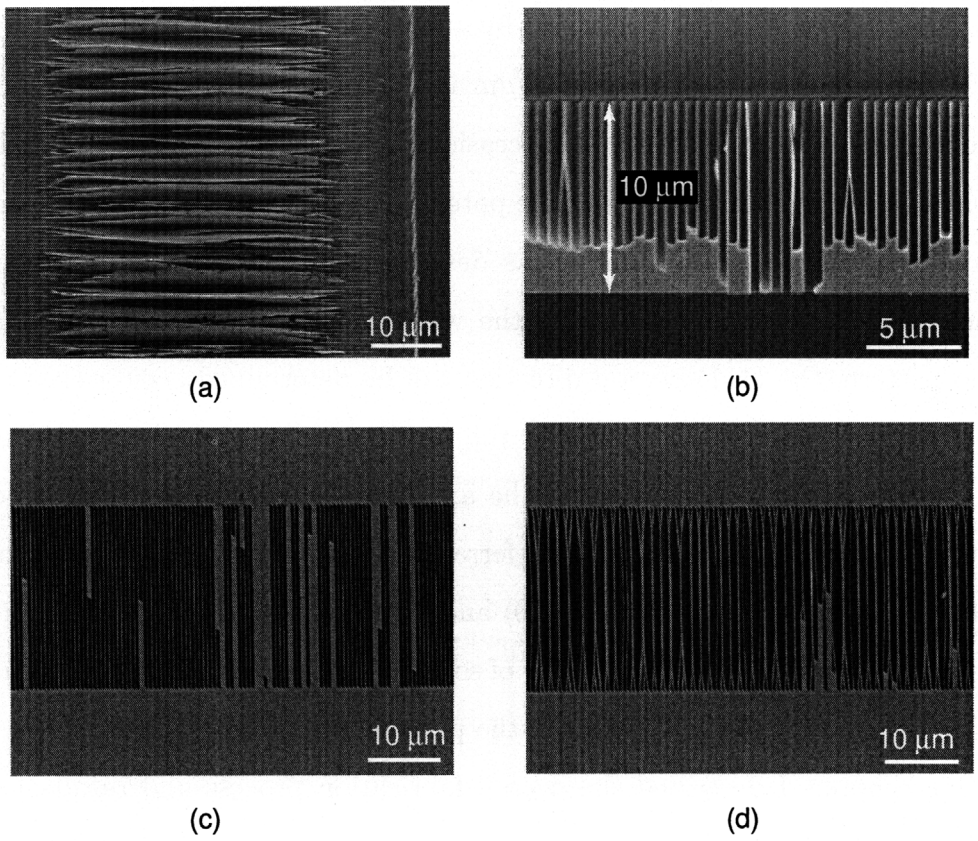


Figure 3-14: Electron micrographs of KOH etching problems. (a) Top view of an overetched sample due to the low anisotropy in 45 wt% KOH at 80 °C. The grating bars were thinned and the nitride mask was lost during etching. (b) Cross sectional view of a sample with non-uniform etching. (c) Bottom view of a sample with non-uniform etching. (d) Bottom view of a sample with stiction in spite of supercritical point drying. (b)-(d) were etched in 50 wt% at 50 °C.

those immersed vertically (compare Fig. 3-13(d) with 3-14(b)). Facing the fine grating bars upward might reduce trapping of $H_2$ bubbles.

With 50 wt% KOH at 50 °C, we achieved ultra-high aspect ratio free-standing transmission gratings. Figure 3-15 shows top and bottom views of a free-standing grating with a 70 $\mu$m pitch support structure. The open gap between support lines was 40 $\mu$m at the top and 5 $\mu$m at the bottom, which agrees well with the crystal angle as shown in Fig. 1-14(b). The line widths of a single grating bar are ~40 nm at the top and ~90 nm at the bottom. The aspect ratio of the grating bar is 152 based on the average width of 65 nm. The slope angle of the sidewalls is only about 0.15°. The sidewall roughness (root mean square) of a test sample is less than 0.2 nm over

$65 \times 65$ nm$^2$ area, which was measured by an atomic force microscope.

For wider support mesh periods of 90 $\mu$m and 120 $\mu$m, similar results were obtained in some areas. However, there are still occasional uniformity and stiction problems as shown in Figs. 3-14(c) and 3-14(d). One potential solution is to find the actual $\langle 111 \rangle$ direction using a pre-etch technique, as described in Ref. [37], for better pattern alignment to the crystal. By etching the wafer anisotropically with a fan-shaped masking pattern, the $\langle 111 \rangle$ crystal direction can be determined accurately to within $\pm 0.05°$. Various surfactants that reduce the surface tension and increase the wetting ability without significantly changing the anisotropy may also improve uniformity. Generally, alcohol additives are not preferred for high aspect ratio etching because alcohols slow down the etch rate of $\langle 110 \rangle$ and degrade the anisotropy [32]. However, an anionic surfactant (e.g., dihexyl ester of sodium sulfosuccinic acid) has been shown to reduce the contact angle to a half of the pure 30 wt% KOH solution [58].

In this chapter, I described the overall fabrication process and results for CAT grating prototypes with 574 nm period. The remaining issues such as etch anisotropy, etch uniformity, and the stress in buried oxide will be addressed in the following chapters.

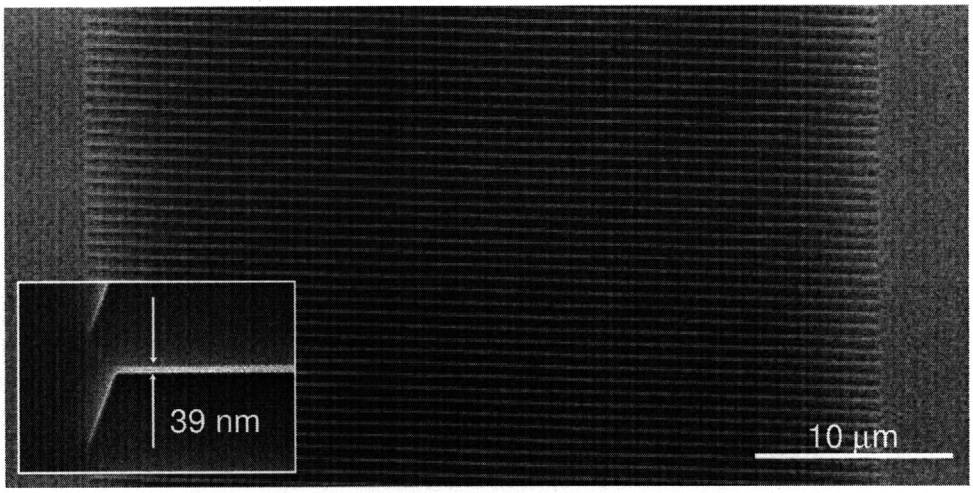


(a)

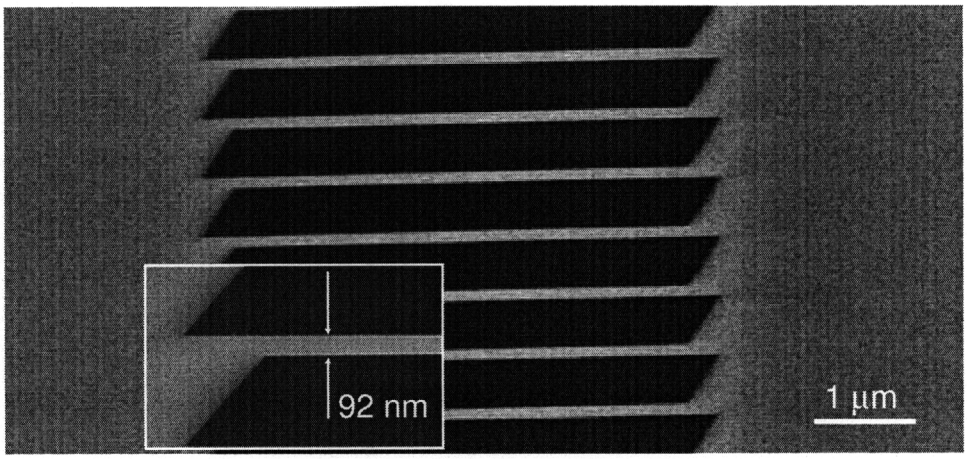


(b)

Figure 3-15: Electron micrographs of a CAT grating between the support mesh bars. (a) Top view of the fine grating between a 40 $\mu$m open gap. The linewidth at the top is 39 nm. (b) Bottom view of the grating. The open gap is shrunk to $\sim$5 $\mu$m to due the slanted $\{111\}$ planes. The linewidth is 92 nm, which is consistent with an average sidewall slope of $\sim$0.15°.

# Chapter 4

# Process Improvement for 200 nm-period CAT Gratings

In the previous chapters, I have introduced the concept of the critical-angle transmission (CAT) grating [2] and fabricated 574 nm-period CAT grating prototypes on 10 $\mu$m-thick SOI wafers [36]. Diffraction tests of these gratings with low energy x-rays (<0.5 keV) have shown high-efficiency blazing as predicted by theory [2]. However, for higher energy x-ray applications, shorter period CAT gratings with a duty cycle (linewidth/period) less than 0.2 are desired [12]. Therefore, we need to adapt the previous process to the fabrication of 200 nm-period CAT gratings with 40 nm linewidth.

I have used KOH etching on ⟨110⟩ SOI wafers to achieve straight and high aspect ratio free-standing gratings. In order to achieve 6 $\mu$m-tall and 40 nm-wide grating bars by etching, etch anisotropy between ⟨110⟩ and ⟨111⟩ silicon crystal lattice planes should be at least 200, considering the silicon nitride mask line width (<100 nm) formed by interference lithography and RIE, as well as undercut during KOH etching. The etch rate anisotropy in KOH solutions dramatically varies depending on pattern alignment to the ⟨111⟩ direction, the KOH concentration, and etching temperature [32, 41]. I also found that there was a rapid initial undercut, which impaired the etch anisotropy. I investigated these factors to optimize the KOH etch process for etching the 200 nm grating pattern. In order to increase etch process latitude through

increased linewidth, I applied an image-reversal technique with a high silicon content spin-on polymer, Silspin (Molecular Imprints, TX). A surfactant, sodium dihexyl sulfosuccinate (SDSS), was added to KOH solutions to promote hydrogen bubble release. In addition to the surfactant, ultrasonic agitation was also tested to improve etch uniformity.

In the following, I will describe the process improvements in detail and demonstrate CAT gratings with a 200 nm period on 4 - 6 $\mu$m-thick SOI layers.

## 4.1 Etch Anisotropy

A high etch anisotropy or etch-rate ratio between {110} and {111} planes is essential to obtain a vertical etch profile without significant lateral etching or undercutting. In particular, it would be very difficult to fabricate 200 nm-period CAT gratings on a 6 $\mu$m-thick SOI layer with an etch anisotropy less than 200. Assuming a 100 nm-wide SiN hard mask, which is the upper bound of the linewidth formed by interference lithography with a positive photoresist, let us estimate a required etch anisotropy. Based on the geometric specification of a 200 nm-period CAT grating, the grating bar width and height are required to be 40 nm and 6 $\mu$m, respectively. The undercut amount for each side has to be smaller than or equal to 30 nm with vertical etching of 6 $\mu$m. Thus, an etch anisotropy greater than 200 is required. Literature data for the etch anisotropy varies in a large range of 50 - 600, depending on pattern alignment, etching conditions, and feature sizes [32]. Generally, people obtain the etch anisotropy of about 200 or less for relatively large micrometer-scale structures. However, there are sparse research results on KOH etching of nano-scale structures with 200 nm-period. Therefore, I investigated various factors affecting KOH etch anisotropy with 200 nm-period grating patterns.

### 4.1.1 Grating Pattern Alignment

Grating pattern alignment is one of the most dominant factors that determine etch anisotropy. When the grating pattern is perfectly aligned to the {111} silicon planes,

we expect the highest etch anisotropy with a minimal undercut and extremely smooth grating sidewalls without microscale steps. Figure 4 in Ref. [32] illustrates the effects of misalignment on the undercut amount and sidewall roughness. The angular misalignments with the {111} plane results in large undercutting of the etch mask and microsteps in the {111} planes.

There are couple of methods to find the actual ⟨111⟩ direction. The easiest but coarse way is to use the wafer flat in ⟨111⟩ orientation as a reference surface for the interference fringe alignment. However, wafer flats are, in general, machined with a finite tolerance of ±0.5° and sometimes I observed the wafer flats were warped as well. Thus this method is not appropriate for a precise pattern alignment within 0.1°.

Another method to determine the true crystal lattice direction is based on cleaving [59]. While a ⟨100⟩-oriented silicon wafer cleaves along {110} planes with an angle of 90°, a ⟨110⟩-oriented silicon wafer cleaves along {111} planes into a parallelogram with an angle of 70.5°. This method is destructive and we have to assume the other wafers from a batch have the same misorientation angle with the cleavage-tested one. However, when a ⟨110⟩-oriented silicon wafer is cleaved, I found that the cleavage plane would not follow a single {111} plane but frequently jumps to the next, resulting in a non-perfect parallelogram. One can observe the micro-steps in a cleaved {111} surface using an optical microscope. Therefore, the cleaving method is not repeatable for a ⟨110⟩ wafer.

The most precise method for determining the true ⟨111⟩ direction of a ⟨110⟩ wafer is to pre-etch an alignment pattern consisting of radially divergent lines with an angle offset [28,37]. After etching this "wagon wheel" shaped or fan-shaped pattern in KOH solution, one can find a direction that produces the smallest undercut amount using microscopy. This method was used for the 200 nm-period CAT grating fabrication. A fan-shape masking pattern (0.05° spacing between ±3°) was defined near the wafer flat by contact lithography and $CF_4$ RIE as shown in Fig. 4-1(a). An individual slot or spoke dimension was 8 $\mu$m × 10 mm. After stripping the photoresist, the wafer was etched in ~ 25 wt% KOH solution at 80 °C for about half an hour. Optical microscopy can be used only for rough determination of the ⟨111⟩ direction because

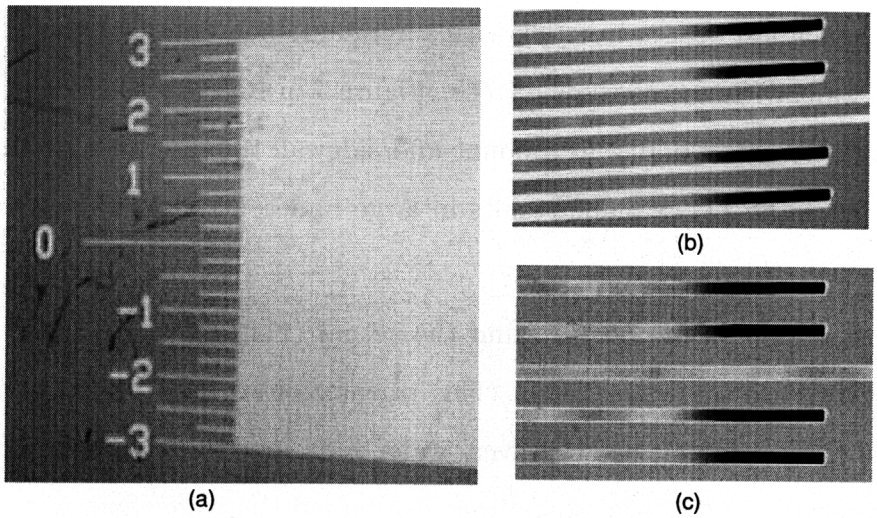


Figure 4-1: Optical micrographs of the fan-shape mask pattern (a) before KOH etching, (b) and (c) after KOH etching for two different regions of the fan-shape pattern. The bright parts in (b) and (c) show the mask undercutting and we can tell the lines in (c) are closer to the true {111} planes than those in (b).

the undercut amounts of neighboring lines near the true ⟨111⟩ planes are hard to distinguish as shown in Fig. 4-1(c). Therefore, the undercut amounts of the spokes were inspected using SEM for a precise measurement. Thin (~40 nm) nitride is partially transparent at 5 keV SEM voltage and the undercut is measurable in the top view as shown in Fig. 4-2. For example, Fig. 4-3 shows the measurement result and the minimum undercut direction (-0.75°) is determined to the true ⟨111⟩.

Once the true ⟨111⟩ direction of a wafer is determined from the wagon-wheel spokes, the interference fringe is to be aligned to that direction. The interference fringe

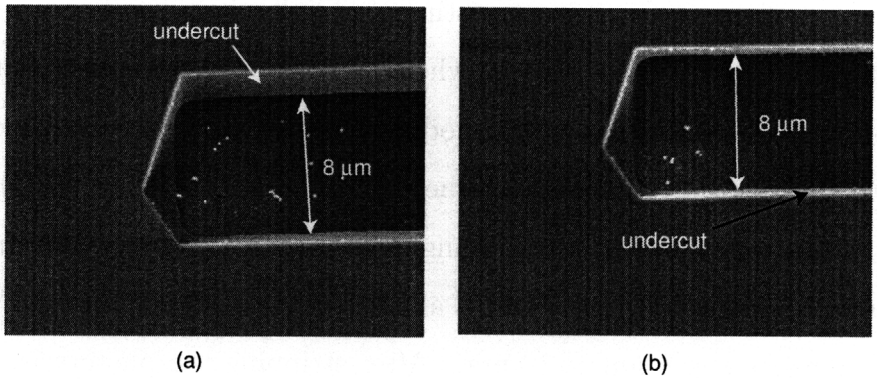


Figure 4-2: SEM images of two different spokes of the fan-shape mask after KOH etching.

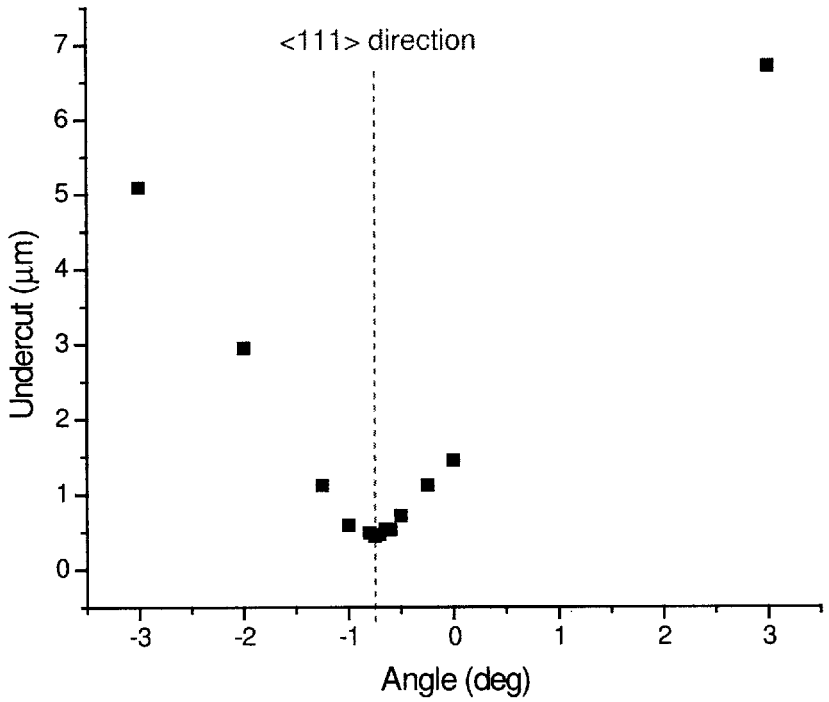


Figure 4-3: An example of determination of the actual ⟨111⟩ direction of a ⟨110⟩ wafer using the pre-etched fan-shape pattern. The minimum undercut direction can be assumed to be parallel to a {111} plane. In this example, the actual {111} plane is -0.75° off from the fan 0° direction.

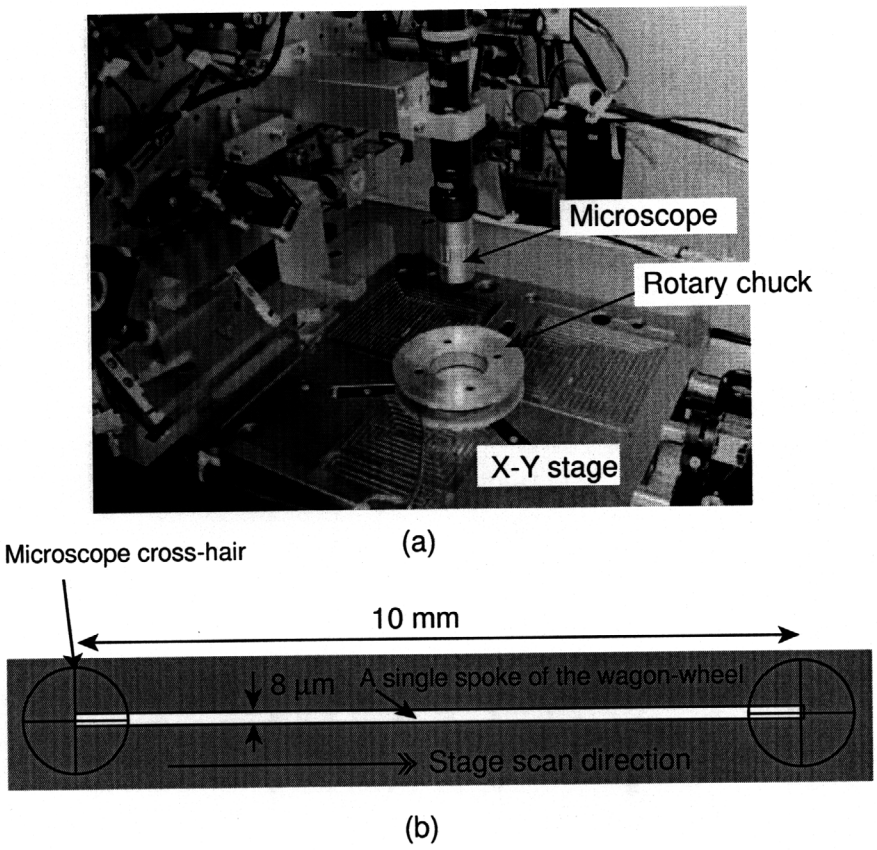


Figure 4-4: (a) The stage microscope mounted on the optical bench of the Nanoruler and (b) fringe alignment scheme using the cross-hair mark of the stage microscope. The X-Y stage is scanned along the fringe direction and the wafer is adjusted using the rotary chuck so that the determined slot is in a fixed position in the microscope.

direction can be found using position sensitive detectors (PSDs) in the Nanoruler [24]. The interference fringe direction was then aligned with the determined spoke or slot direction of the wagon-wheel pattern to within $\pm$ 0.05° using a microscope mounted on the vertical optical bench of the SBIL system looking down on the wafer. The slot was aligned to have a fixed position in the microscope cross-hair when moving the X-Y scanning stage along the fringe direction. Figure 4-4 shows the stage microscope and stage scanning scheme to align the fringe direction to a slot. An angle error due to microscope mislocation within a slot is less than $\tan^{-1}(8\ \mu\text{m}/10\ \text{mm}) = 0.046°$. Making sure that the scanning stage followed the 10 mm-long slot from one end to the other, I exposed the whole 4″ wafer aligned with the interference fringe. Even though a white light source was used for the microscope viewing the wagon-wheel pattern, I

did not observe any effect on the rest of wafer area with the 200 nm-period grating pattern. When the interference fringe was scanned, the microscope light source was kept off.

### 4.1.2 Etching Temperature and Concentration

Etching temperature and KOH concentration affect etch rates of different crystal planes and thus their ratio or etch anisotropy [32–34, 37, 41, 60, 61]. Kendall [60] reported a linear increase of the etch rate ratio ($R_{\langle 110\rangle}/R_{\langle 111\rangle}$) with KOH concentration at 85 °C and Uenishi *et al.* [33] and Krause *et al.* [34] also found a similar relationship between KOH concentration and the etch anisotropy of $\langle 110\rangle$ to $\langle 111\rangle$.

Regarding the effect of temperature, I would utilize an empirical Arrhenius expression for the KOH etch rates [37],

$$R = R_0 \exp(-E_a/kT), \tag{4.1}$$

where $R_0$ is a proportional constant, $E_a$ is the activation energy, $k$ is the Boltzmann constant*, and $T$ is the etching temperature in Kelvin. Note that $R_0$ and $E_a$ depend on KOH concentration and crystallographic orientation of etching silicon surfaces. Seidel *et al.* [37] found the activation energy of the $\langle 111\rangle$ orientation was larger than that of other crystal orientations such as $\langle 110\rangle$ and $\langle 100\rangle$. Therefore, we can expect a decrease of the etch anisotropy as the etching temperature increases because $(E_{a_{\langle 110\rangle}} - E_{a_{\langle 111\rangle}}) < 0$ in the following expression,

$$\frac{R_{\langle 110\rangle}}{R_{\langle 111\rangle}} = \frac{R_{0_{\langle 110\rangle}}}{R_{0_{\langle 111\rangle}}} \exp(-(E_{a_{\langle 110\rangle}} - E_{a_{\langle 111\rangle}})/kT). \tag{4.2}$$

For example, with the experimental data for $R_{\langle 110\rangle}$ and $R_{\langle 111\rangle}$ shown in Fig. 4-7, the etch rates and anisotropy are plotted as a function of temperature in Fig. 4-5 assuming $E_{a_{\langle 110\rangle}} \simeq 0.6$ eV and $E_{a_{\langle 111\rangle}} \simeq 0.7$ eV [37]. From Fig. 4-5, we can expect an increase of the anisotropy at low etching temperatures.

*$k = 8.617 \times 10^{-5}$ eV/K

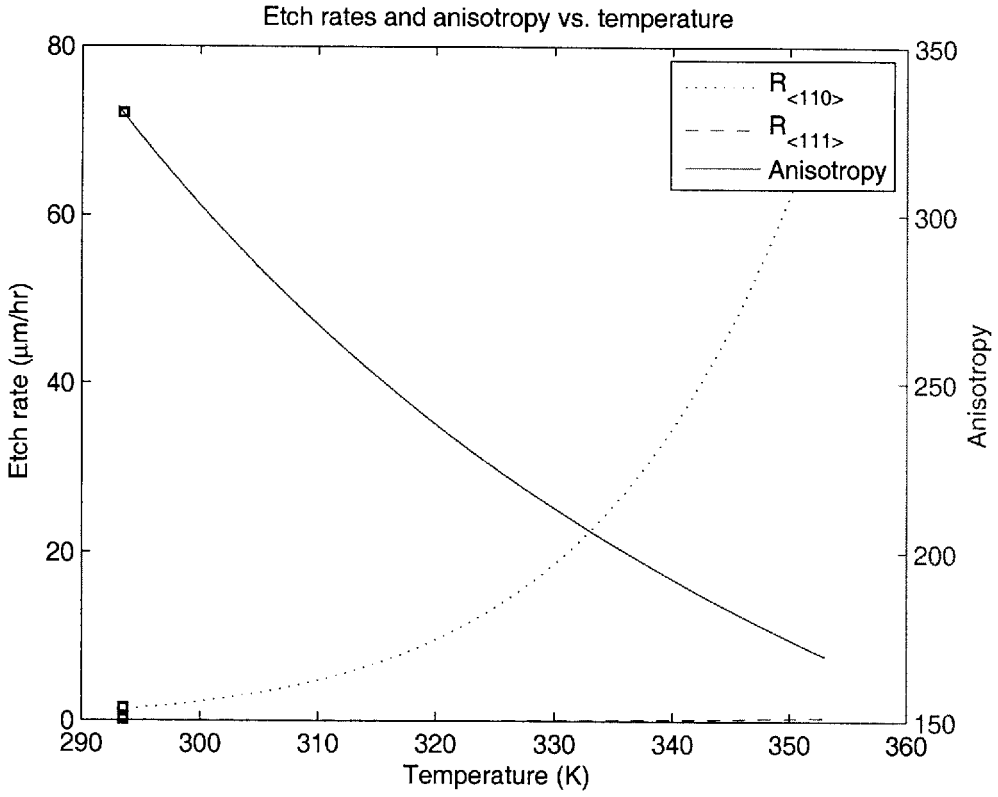


Figure 4-5: Etch rates and anisotropy versus temperature (20 - 80 °C) based on the Arrhenius equations in Eqns (4.1) and (4.2). The dotted and dashed lines represent calculated etch rates of ⟨110⟩ and ⟨111⟩ orientations, respectively. The solid line shows etch anisotropy. The open squares are experimental data points from Fig. 4-7.

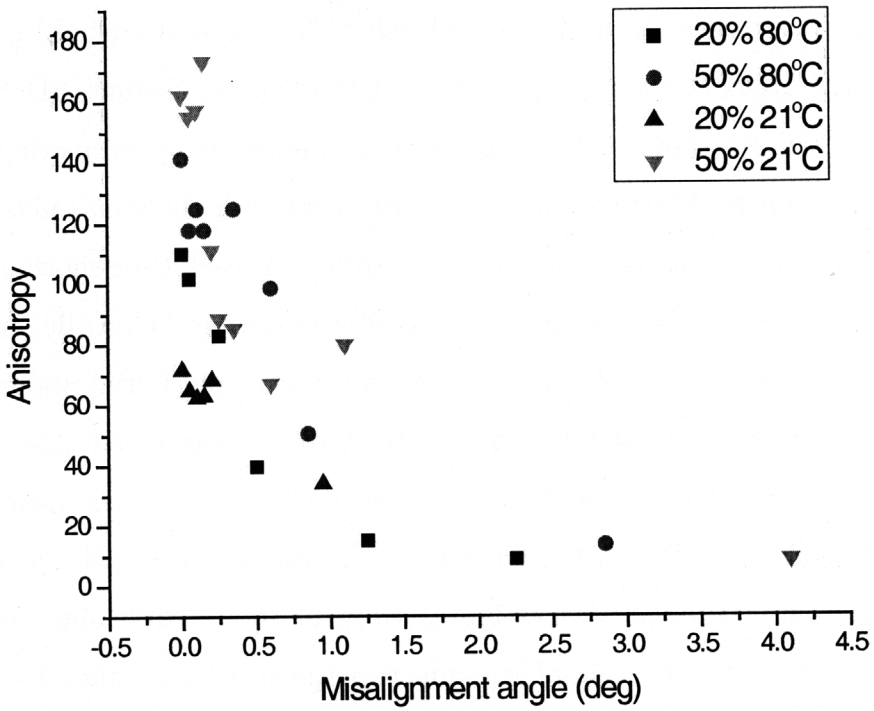


Figure 4-6: Etch anisotropy between ⟨110⟩ and ⟨111⟩ planes at different etching conditions and pattern misalignment with respect to the ⟨111⟩ plane.

Based on the expectation of a high etch anisotropy at high KOH concentrations and low etching temperatures, I investigated etch anisotropy dependency on KOH concentration, temperature, and pattern alignment by etching the fan-shape patterns under four different conditions, as shown in Fig. 4-6. The anisotropy was determined by the ratio of etch depth to the undercut amount. I observed that higher concentrations and lower temperatures resulted in higher etch anisotropy as expected. We can notice the pattern alignment is also one of the most important factors in obtaining a high etch anisotropy.

### 4.1.3 Rapid Initial Undercut

In the previous section, we confirmed that a high etch anisotropy could be obtained in a highly concentrated KOH solution at a low etching temperature. However, even the best anisotropy values in Fig. 4-6 were less than literature values [28, 32] and below our process requirement (>200). Therefore, I conducted a timed etching experiment with a 200 nm-period grating to investigate this low etch anisotropy problem. The

grating used was well aligned by the pre-etch technique and etched in surfactant-added 50 wt.% KOH at room temperature (21 °C). The surfactant, SDSS (MA-80I, Cytec Inc., NJ), was applied to improve etch uniformity by promoting hydrogen bubble release during KOH etching [58]. I will deal with the etch uniformity issue and surfactants in a separate section in this chapter. At each time shown in the plot, I measured the silicon linewidth from the top after removing the nitride, and the etch depth after cleaving. Figure 4-7 shows there is a very rapid initial undercut, which might be caused by mask roughness. After about 10 minutes of etch, the lateral etch rate approaches a roughly constant rate of 4.3 nm/hr, which is assumed to be the actual ⟨111⟩ etch rate. The ⟨110⟩ etch rate (open squares) in Fig. 4-7 was relatively constant at about 1.4 $\mu$m/hr. An etch anisotropy of about 325 is obtained from the ratio of these etch rates. I repeated the same experiment with another 200 nm-period grating sample with a different SiN mask line width and found similar results as shown in Fig. 4-8. It is clear that the anisotropy values in Fig. 4-6 are inaccurate because the lateral etch rate had been determined by including the initial rapid undercut from the initial mask linewidth roughness.

## 4.2 Process Latitude

With an etch anisotropy about 300 and the initial undercut amount of 20 - 30 nm, it is difficult to etch through the 6 $\mu$m-thick device layer with a goal grating bar width of 40 nm, considering the SiN mask linewidth formed by interference lithography with a positive photoresist and RIE. The maximum duty cycle of the grating pattern in a positive photoresist is 50% [26], and following RIE processes to transfer the pattern into the ARC and SiN layers produce some amount of lateral etching as well. The lateral etching amount in RIE processes depends on the etch anisotropy ($\sim 5 - 10$) of the RIE processes and overetching time. We usually overetch by 10 - 20% to make sure the target layer is completely removed. As a consequence, the SiN mask linewidth ends up being no wider than 80 nm and there is a rapid initial undercut about 20 -30 nm during KOH etching as well. Figure 4-9(c) shows the low process

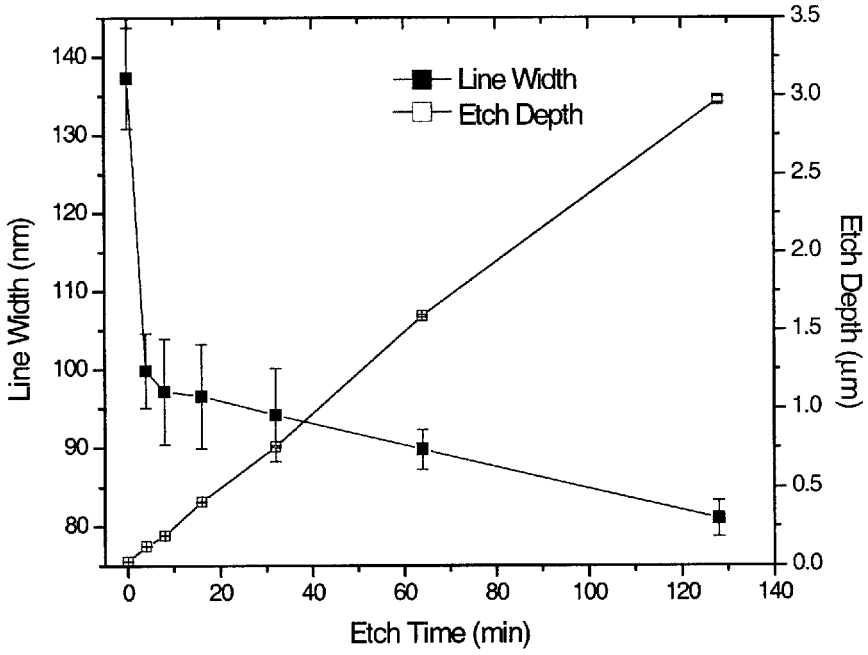


Figure 4-7: Etched grating line width and depth with increasing etching time. The etch depth (open squares) increases linearly, so the vertical etch rate, $R_{\langle 110 \rangle}$, stays constant at about 1.4 $\mu$m/hr. However, the line width (full squares) drops very rapidly in the first few minutes and slows to a constant rate, which should correspond to the actual $\langle 111 \rangle$ etch rate ($R_{\langle 111 \rangle}$). The initial undercut rate and the actual $R_{\langle 111 \rangle}$ are about 4.6 nm/min and 4.3 nm/hr, respectively.

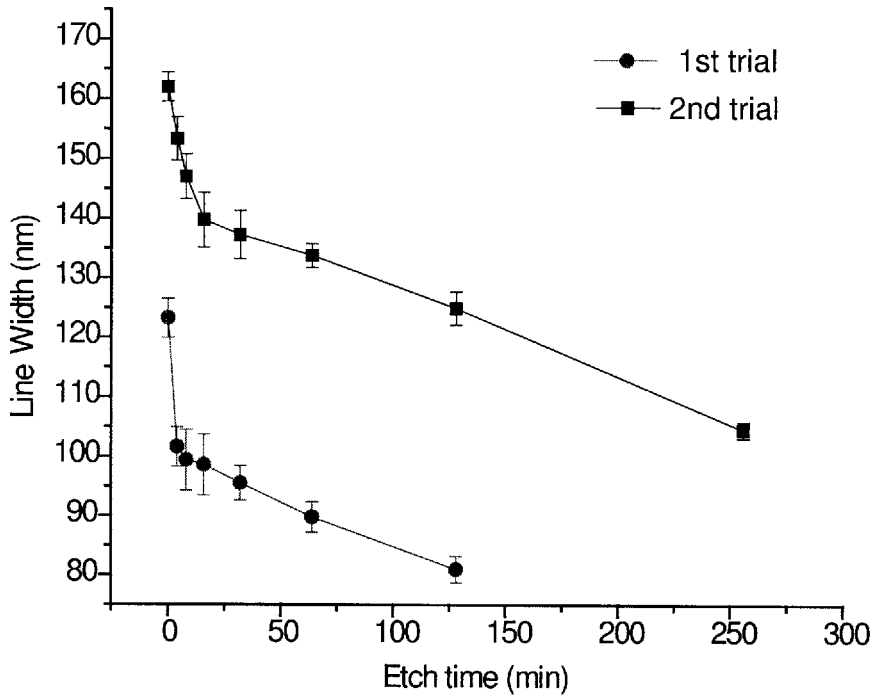


Figure 4-8: Repeatability tests of the rapid initial issue during KOH etching of 200 nm-period gratings. In the first and second trials, the grating samples with different SiN mask line widths were etched under the same conditions.

latitude problem of KOH etching with narrow SiN mask lines.

In order to solve this problem, I used an image reversal technique that Dr. Chang developed for his multilevel process [26]. The 200 nm-period grating pattern with a duty cycle of less than 20% was reversed using the Silspin and RIE processes to form a wider nitride mask, as shown in Fig. 4-10. By using the spin-on polymer, we obtain better pattern uniformity within the wafer compared to metal evaporation with a point source and a lift-off process. In the image-reversal process, the photoresist pattern is first transferred into the antireflection coating (ARC) [Fig. 4-10(a)]. The remaining photoresist can be left on because it will be dissolved by the Silspin or optionally removed by n-methyl-2-pyrrolidone (NMP). Silspin is conformally spin-coated on the ARC pattern [Fig. 4-10(b)]. Using $CF_4$ and $O_2$ RIE consecutively, the pattern is transferred into nitride and silicon [Figs. 4-10(c)-(e)]. The remaining Silspin can be removed by piranha cleaning (sulfuric acid + hydrogen peroxide). The duty cycle of the image-reversed pattern is about 70%.

There is a processing issue during the image reversal process due to the 30 nm-thick

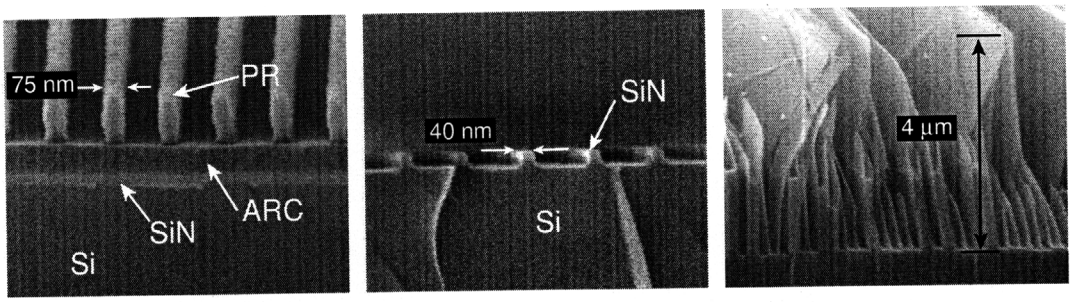


Figure 4-9: (a) A typical 200 nm-period grating pattern in the photoresist (PR) and (b) the grating pattern transferred into silicon nitride (SiN) after removing PR and ARC. (c) An example of unsuccessful KOH etching due to the narrow SiN mask shown in (b). The SiN mask was detached during KOH etching due to undercutting.

chromium support pattern. The ARC and Silspin thicknesses on top of the Cr/SiN layers are thinner than those on top of the SiN layer where the grating pattern is to be transferred [Fig. 4-11]. Therefore, when etching the Silspin and ARC layers, we need to take into account this thickness variation between the areas with different layer stacks to ensure the grating pattern is completely transferred into the Silspin layer. Figures 4-12(a) and (b) show a successful pattern transfer into the Silspin layer on both areas and a problem during the image reversal process due to an insufficient $CF_4$ etch-back time, respectively.

## 4.3 Etch Uniformity

In Chapter 3, I briefly discussed etch depth variation or non-uniformity across a CAT grating sample shown in Fig. 3-14(c). There are many factors that affect the etch uniformity, including the aspect ratio of the channel between the grating bars [39], local KOH concentration variation [62], sample placement [36], and hydrogen bubbles from KOH reaction with silicon. Non-uniform etch depth and surface roughness for deep structures are often ascribed to micromasking due to hydrogen bubbles from KOH etch reaction [28, 37, 58],

$$\mathrm{Si} + 2\mathrm{OH}^- + 2\mathrm{H_2O} \rightarrow \mathrm{SiO_2(OH)_2^{2-}} + 2\mathrm{H_2(gas)} \ . \tag{4.3}$$

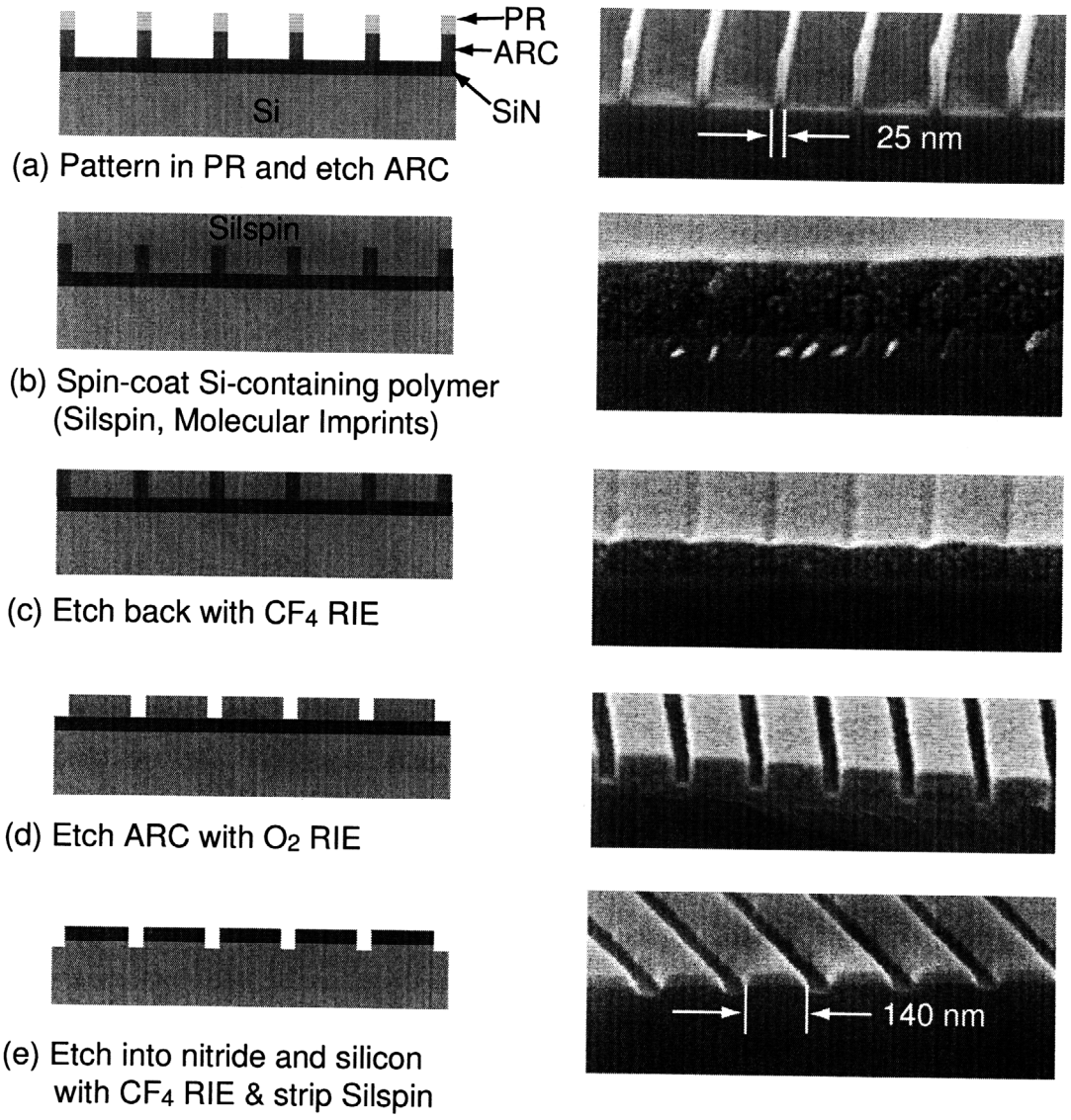


Figure 4-10: Schematic and SEM images of an image-reversal technique using a Si-containing polymer. The duty cycle of the 200 nm-period grating pattern is reversed from 12.5% in photoresist (PR) and antireflection coating (ARC) to 70% in silicon nitride.

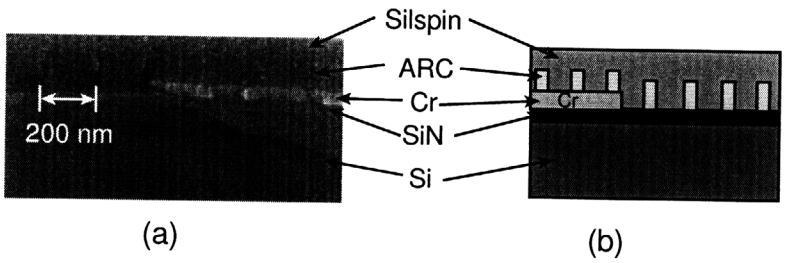


Figure 4-11: (a) SEM image and (b) schematic of the interface between Cr/SiN area and SiN area after spin-coating the Silspin.

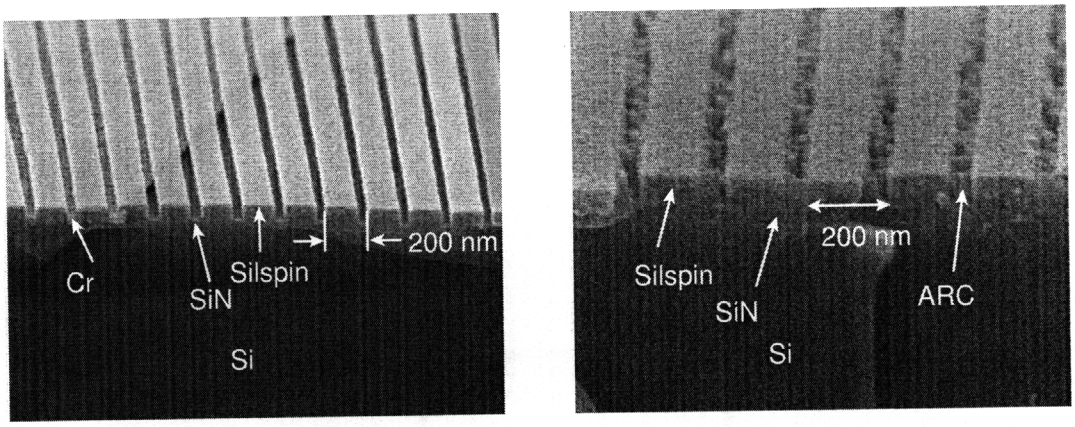


Figure 4-12: (a) A good pattern transfer into the Silspin layer and (b) ARC left-over between the Silspin lines on top of silicon nitride due to insufficient $CF_4$ etch-back of the Silspin.

As described in Section 3.5 in Chapter 3, the sample placement might be related to the hydrogen bubbles trapped between the grating bars. While the horizontal sample placement solved the uniformity problem for 574 nm-period CAT grating prototypes, it was insufficient to improve the etch uniformity for the 200 nm-period CAT gratings because the bubbles more likely tend to be trapped between narrower channels. Figure 4-13 shows the micro-masking problem due to the hydrogen bubbles. Silicon under the bubbles is protected from being etched in KOH solution. These hydrogen bubbles are believed to lead a non-uniform etch depth and rough surfaces forming hillocks in the etched surface. Previously various additives and agitation methods for MEMS applications have been tried to accelerate bubble detachment [58,63–65]. I tested a surfactant and ultrasonic agitation for the fabrication of 200 nm-period gratings while keeping a high etch anisotropy to form high aspect-ratio grating bars.

### 4.3.1 Surfactants

Surface tension is the force that causes hydrogen bubble attachment on the surface. An increase of the bubble volume and hence of buoyancy leads to detachment of the bubble from the surface. However, a bubble stuck on silicon collects hydrogen slowly

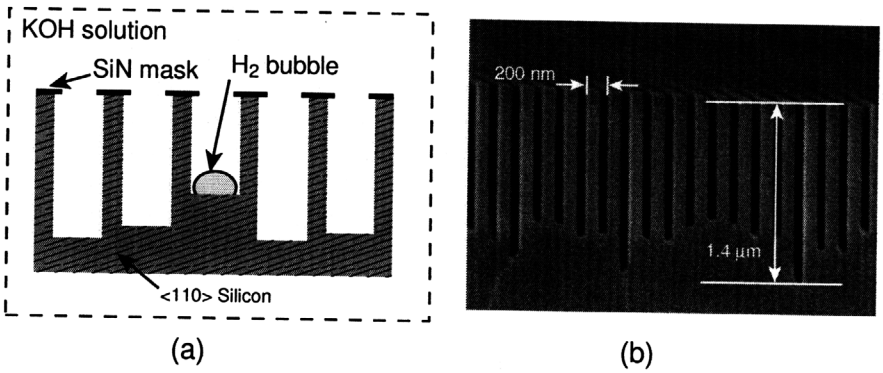


Figure 4-13: (a) Schematic of micromasking due to hydrogen bubbles and (b) cross section electron micrograph of a KOH-etched 200 nm-period silicon grating with non-uniform etch depth.

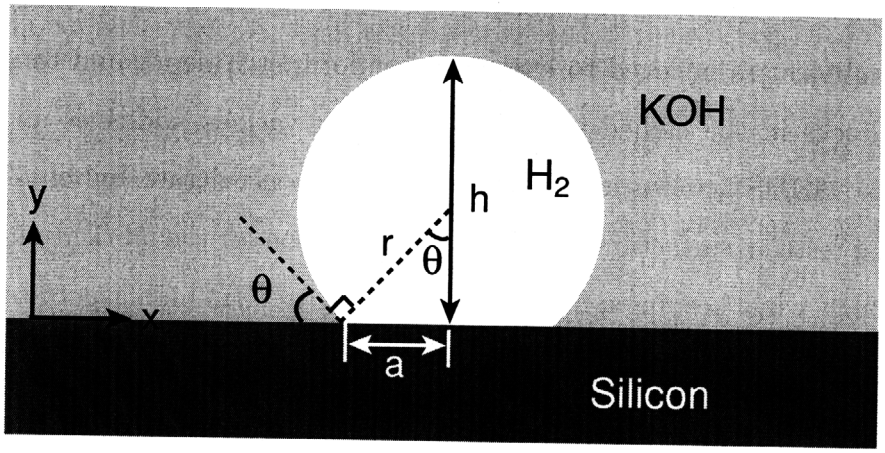


Figure 4-14: A hydrogen bubble attached to the silicon surface with an angle $\theta$.

because the bubble-covered area cannot react with KOH. Figure 4-14 illustrates a spherical hydrogen bubble with a fixed volume $V_{H_2}$ attached to silicon in KOH solution with the contact angle $\theta$ between the solid surface and the tangent to the liquid-gas interface. The + y-direction force due to buoyancy is

$$\begin{aligned} F_b &= (\rho_{KOH} - \rho_{H_2}) \cdot g \cdot V_{H_2} \\ &= (\rho_{KOH} - \rho_{H_2}) g \left[ \frac{1}{6} \pi h (3a^2 + h^2) \right] \\ &= (\rho_{KOH} - \rho_{H_2}) g \left[ \frac{1}{3} \pi r^3 (1 + \cos\theta)^2 (2 - \cos\theta) \right], \end{aligned} \tag{4.4}$$

where $\rho_{KOH}$ and $\rho_{H_2}$ are densities of the KOH solution and hydrogen bubble, respectively. From the geometry,

$$a = r \sin\theta, \tag{4.5}$$

$$h = r(1 + \cos\theta), \text{ and} \tag{4.6}$$

$$r = \left[ \frac{3}{\pi} \frac{V_{H_2}}{(1 + \cos\theta)^2 (2 - \cos\theta)} \right]^{1/3}. \tag{4.7}$$

The - y-direction force due to surface tension $\gamma$ is

$$F_\gamma = 2\pi a \gamma \sin\theta. \tag{4.8}$$

The contact angle $\theta$ is determined by force equilibrium at the solid/liquid/gas interface and described by the Young Equation [64, 66, 67]

$$\cos\theta = \frac{\gamma_{sg} - \gamma_{sl}}{\gamma}, \tag{4.9}$$

where $\gamma_{sg}$ and $\gamma_{sl}$ denote the solid-gas and solid-liquid interfacial energies, respectively, and $\gamma$ ($> 0$) is the surface tension at the liquid-gas interface. Note that $(\gamma_{sg} - \gamma_{sl}) > 0$ for $0° < \theta < 90°$ and $(\gamma_{sg} - \gamma_{sl}) < 0$ for $90° < \theta < 180°$ because $\gamma$ is always positive. Substituting Eqns (4.5), (4.7), and (4.9) into Eqn.(4.8), we obtain $F_\gamma$ as a function of $(\gamma_{sg} - \gamma_{sl})$ and $\gamma$. Assuming that $(\gamma_{sg} - \gamma_{sl})$ is constant for $0° < \theta < 90°$, $F_\gamma$

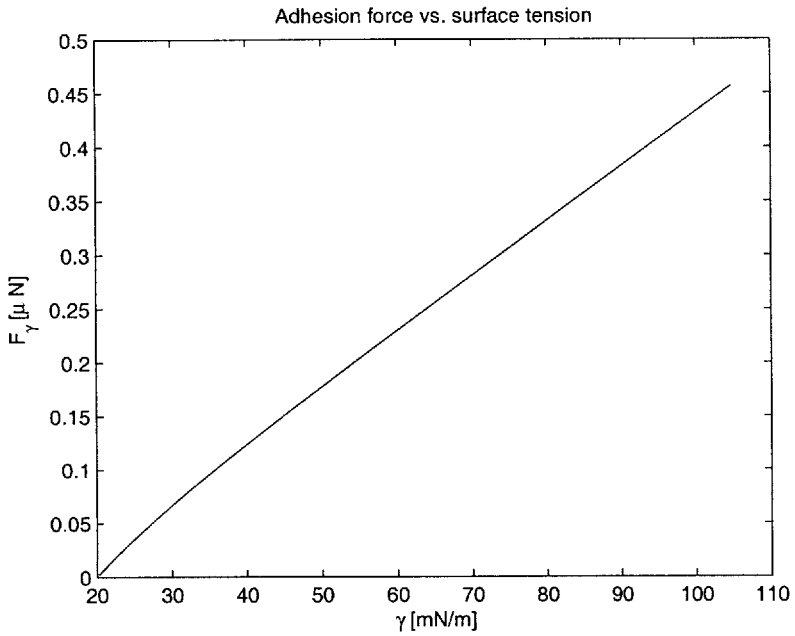


Figure 4-15: Adhesion force vs. surface tension for a 1 $\mu m^3$ spherical hydrogen bubble, assuming $(\gamma_{sg} - \gamma_{sl})$ is constant and $10° < \theta < 80°$. The adhesion force increases with surface tension as expected.

is plotted in Fig. 4-15 as a function of surface tension $\gamma$. From this graph, we can deduce hydrogen bubble detachment will be promoted by reducing surface tension and equivalently the contact angle.

A surfactant is a wetting agent that reduces surface tension. Isopropanol (IPA) is a common surfactant for KOH etching to improve etch uniformity and surface smoothness by reducing surface tension. However, alcohol additives are known to impair the etch anisotropy because the $\langle 110 \rangle$ etch rate in an IPA + KOH solution is decreased by 90% without significantly decreasing the $\langle 111 \rangle$ etch rate [32, 37, 68]. Recently, Yang *et al.* measured the contact angle of various surfactant-added KOH droplets on a silicon wafer [58]. They found that 0.02 wt% sodium dihexyl sulfosuccinate (SDSS, $C_{16}H_{29}NaO_7S$) in KOH solution reduced the contact angle to about 50% of pure KOH solution's contact angle without degrading the etch anisotropy.

I tested the SDSS surfactant (Cytec Industries Inc.) with $\langle 110 \rangle$ silicon pieces with the wagon-wheel pattern in silicon nitride. SDSS was added to 50 wt.% KOH by

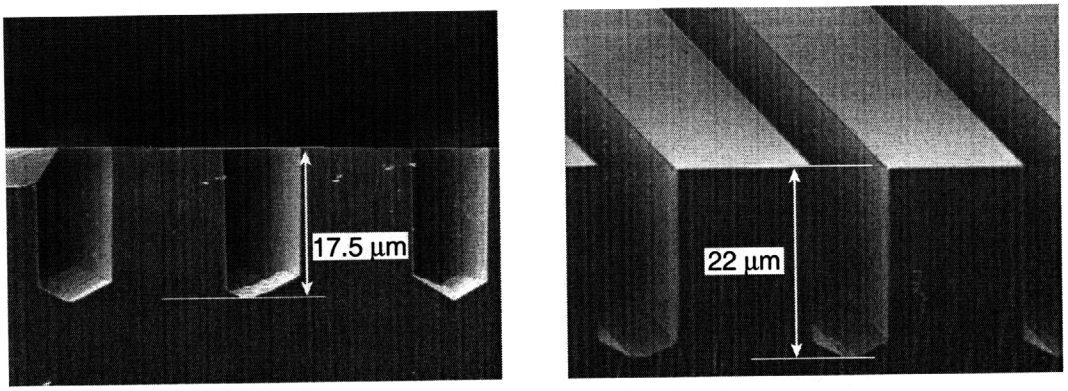


Figure 4-16: SEM images of the wagon-wheel patterns etched for 16 hours at room temperature (a) in 50 wt.% KOH without the surfactant and (b) in 50 wt.% KOH + 0.02 wt.% SDSS.

0.02 wt.% and this solution was cooled down[†] to room temperature (21 °C) before etching. The samples were etched for 16 hours in KOH solutions with and without the surfactant at room temperature. Figure 4-16 shows the influence of the surfactant. The etch bottom was bumpy and irregular when being etched without the surfactant (Fig. 4-16(a)). On the other hand, 0.02 wt.% of SDSS in 50 wt.% KOH solution made it much smoother and uniform (Fig. 4-16(b)). Notably, it increased the vertical etch rate by 30 %, and hence etch anisotropy while not changing the lateral etch rate. White residue after KOH etching could be removed by HF etching. With these relatively large wagon wheel patterns, we did not observe non-uniform etch depth in the pure KOH solution, but the SDSS surfactant definitely improved the etch surface without degrading the etch anisotropy. In particular, the increase of $\langle 110 \rangle$ etch rate led to an increase of the etch anisotropy. From the improved etch surface in the SDSS + KOH solution, we could infer that the hydrogen bubbles were efficiently detached from the silicon surface due to lower surface tension.

There is a processing issue with rinsing samples after etching in the SDSS+KOH solution. Even though solubility of SDSS in water is not low (320 g/L at 25 °C), there is a residue problem with deep etched structures after immersion rinsing with water at room temperature. Figure 4-17(a) shows the organic residue problem on the

[†]KOH + $H_2O$ reaction is exothermic.

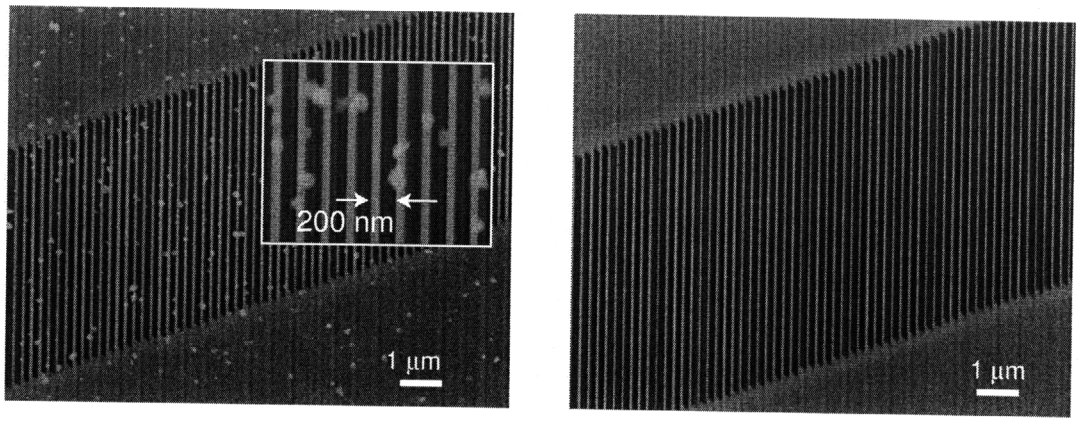


Figure 4-17: SEM images of the back side of 200 nm-period CAT gratings etched in KOH + SDSS after rinsing with (a) water at room temperature and (b) 80 °C water.

back side of a CAT grating sample. Flowing water rinse might remove the residue more efficiently, but it could damage the thin membranes. Therefore, in order to increase the solubility, I used hot water (80 - 90 °C) to rinse the surfactant-added KOH solution. Figure 4-17(b) shows the hot water rinse result without the residue problem.

### 4.3.2 Ultrasonic Agitation

Another way to improve etch uniformity is to actively detach the hydrogen bubbles from silicon surfaces using ultrasound agitation [58, 64, 65, 69]. Traditionally, ultrasonic agitation has been used for cleaning surfaces based on cavitation implosion in oscillating fluid waves. An ultrasound frequency for cleaning applications is normally in a range of 20 - 50 kHz and the cavitation bubble size decreases with the frequency. Even though the cavitation implosion energy is large, the size of the bubbles is so small that the implosion would not damage surfaces in general cleaning applications. However, in many MEMS applications with thin membranes, ultrasonic agitation sometimes breaks the weak structures [58]. Recently, megasound agitation, with a frequency close to 1 MHz, was tried to improve etch uniformity in KOH etching without damaging membranes [65].

While adding a surfactant to KOH solution improved etch uniformity for 200 nm-

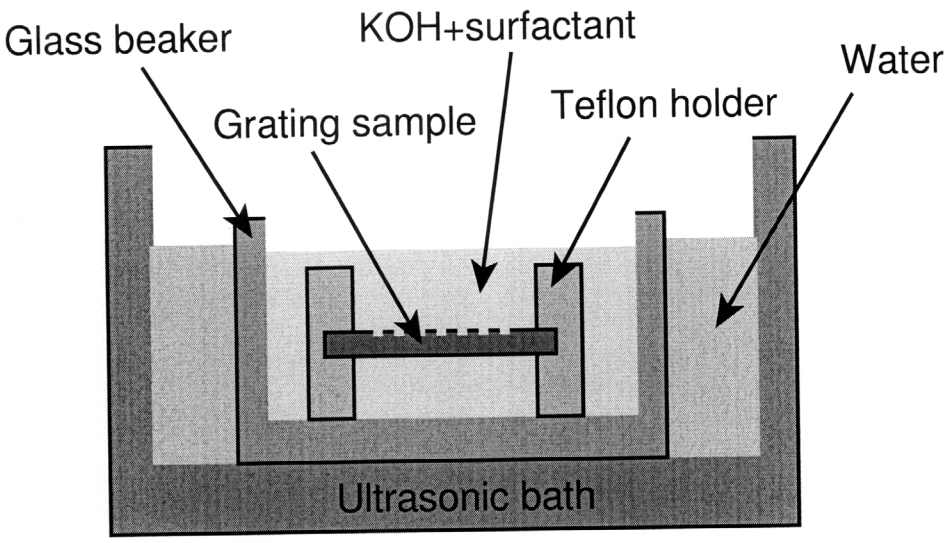


Figure 4-18: A setup for KOH etching with ultrasonic agitation.

period CAT gratings in 4 $\mu$m-thick device layer, it was not satisfactory for etching even thicker device layers because the hydrogen bubbles would be more likely trapped in higher aspect ratio channels. Therefore, I applied ultrasonic agitation to KOH etching with relatively low ultrasonic power levels. Figure 4-18 illustrates the experiment setup where the ultrasound wave (40 kHz) is transmitted through a glass beaker. The ultrasonic bath (Model 275D, Crest Ultrasonics) has adjustable power setting between 10 and 90 Watts with a fixed frequency of 40 kHz. With a low ultrasonic power of 30 W, I etched 200 nm-period gratings in $\langle 110 \rangle$ silicon wafers in a 50 % KOH solution with the SDSS surfactant, resulting in a significant improvement in etch uniformity. Figure 4-19 shows the results after one and two hours of etching. Compared to the irregular etching depth shown in Fig. 4-13, uniformity of etching depth over larger areas is remarkably improved with ultrasonic agitation.

Ultrasonic agitation with the same power level (30 W) was tested with a 5 $\mu$m-thick $\langle 110 \rangle$ Si membrane including the 200 nm-period grating nitride pattern. Even though a similar improvement in etch uniformity was sometimes obtained as shown in Fig. 4-20, ultrasonic agitation with a low frequency may not be a repeatable process especially for a membrane type substrate due to occasional sample damage observed. A megasonic agitation bath might improve etch uniformity more reliably for the CAT grating etching process.

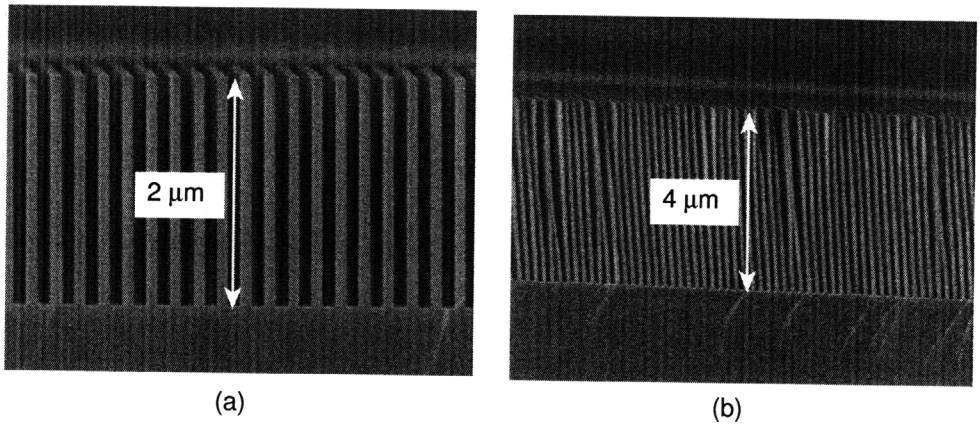


Figure 4-19: 200 nm-period gratings in ⟨110⟩ silicon wafers etched in a surfactant-added KOH solution with ultrasonic agitation (a) for one hour and (b) for two hours. The samples were dried using a critical point drier and stiction in (b) is a cleaving artifact.

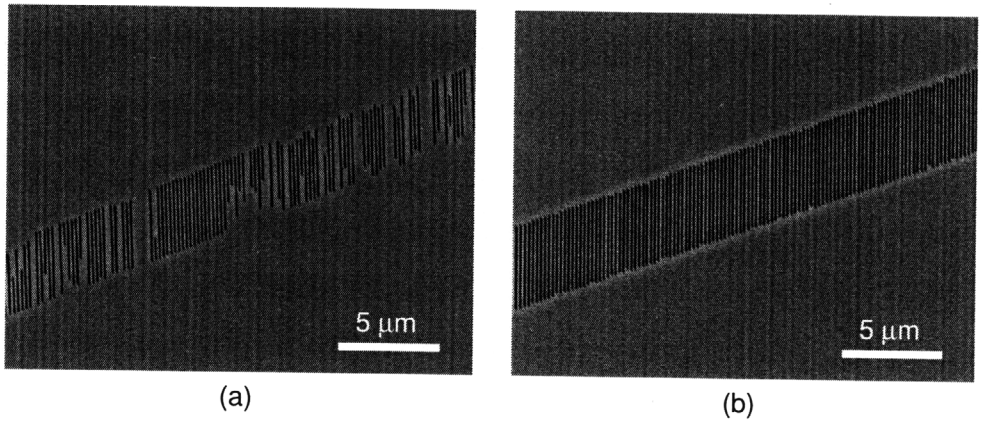


Figure 4-20: SEM images of the backside of 5 $\mu$m-thick CAT gratings. (a) was etched in the surfactant-added 50% KOH at room temperature for 6 hours, and (b) was etched in the same etchant with ultrasonic agitation for 5.5 hours.

## 4.4 Fabrication Results

I successfully fabricated 200 nm-period CAT gratings in 4 - 6 $\mu$m-thick device layers of SOI wafers. 16 grating devices were patterned in a 4″ SOI wafer and each device has a 2.4 $\times$ 2.6 mm$^2$ membrane within a 10 $\times$ 12 mm$^2$ outer silicon frame. Figure 4-21 shows front and back side photographs of the SOI wafer before KOH etching. The membrane area has a 2D support structure and 200 nm-period grating pattern in silicon nitride. Figure 4-22 shows the final nitride etch mask with the support structure and image-reversed 200 nm-period grating pattern. For the 6 $\mu$m-thick CAT gratings, the open gap between support lines at the top was modified to 26 $\mu$m to produce a 5 $\mu$m opening at the bottom after KOH etching.

With the etch mask described above, I performed KOH etching with 50 % KOH and 0.02 % SDSS at room temperature. Figure 4-23 shows top, bottom, and cross-section views of the 4 $\mu$m-thick CAT grating. The open gap between support lines was 20 $\mu$m at the top and 5 $\mu$m at the bottom, which agrees well with the silicon crystal angle for inclined {111} planes. The line widths of a single grating bar are 35 nm at the top and 45 nm at the bottom. The aspect ratio of the grating bar is about 100 with a sidewall slope angle of 0.07°, which implies a very high etch anisotropy. To the best of my knowledge, the sidewall slope in this scale is the steepest reported angle that has been achieved by any etching technique.

Similar fabrication results were obtained in 5 and 6 $\mu$m-thick device layers with a minor modification of the process developed for 4 $\mu$m-thick CAT gratings. In order to take into account more undercutting due to longer etch time for thicker membranes, the image reversal process was optimized to form a wider nitride etch mask. Ultrasonic agitation was applied during etching the 5 and 6 $\mu$m-thick CAT grating to improve etch uniformity. Figures 4-24 and 4-25 show the fabrication results of the 5 and 6 $\mu$m-thick CAT gratings, respectively. The 6 $\mu$m-thick CAT grating in Fig. 4-25 was contaminated with particles during supercritical drying. After changing a filter for inlet liquid $CO_2$ in the critical point dryer, the particles were not observed. However, there could be other possible sources of particle contamination including purity of

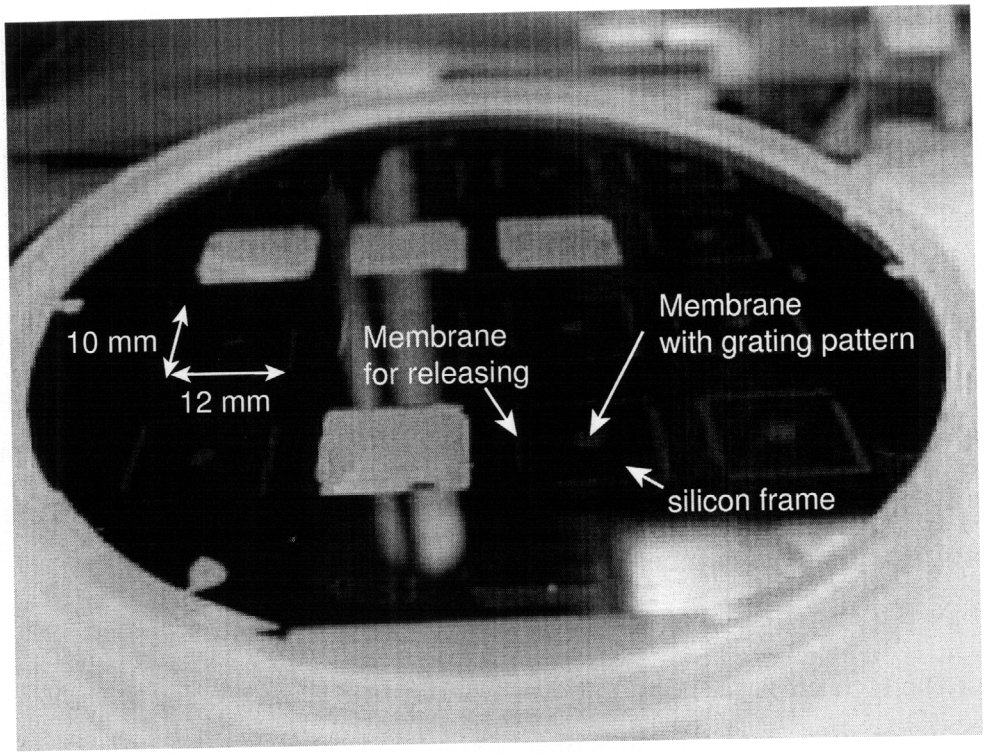


(a) Front side

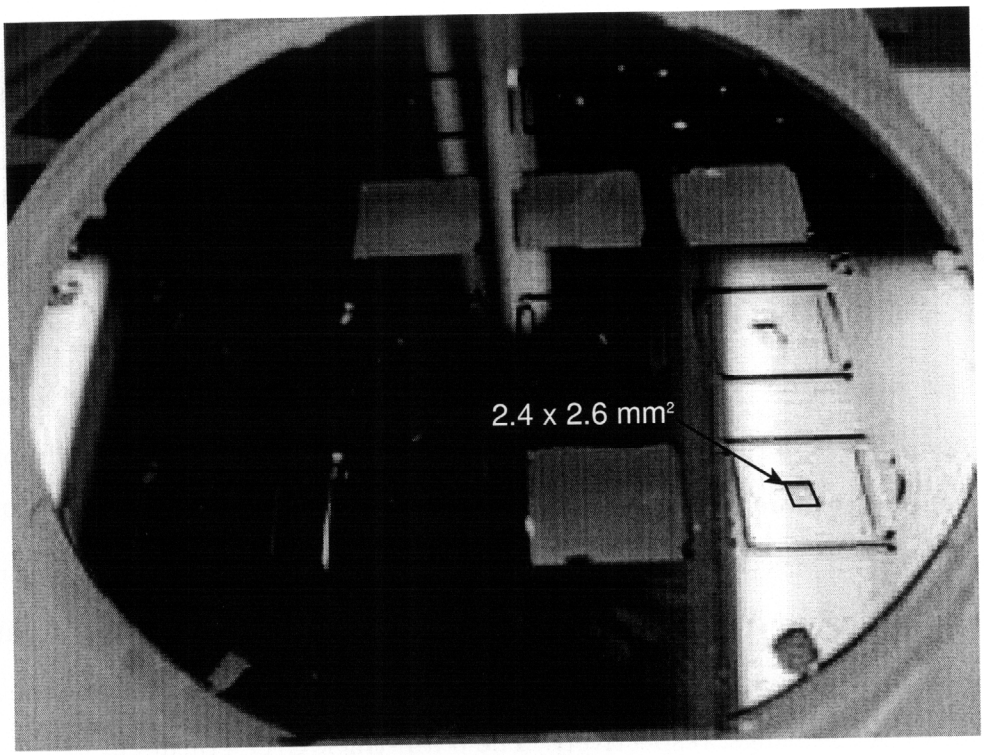


(b) Backside

Figure 4-21: Photographs of an SOI wafer before KOH etching. The membrane areas look brighter than the frame area in the front side picture (a). The backside (b) has been etched in TMAH and stopped at the buried oxide. Four devices out of 16 have been taken out for etching tests.

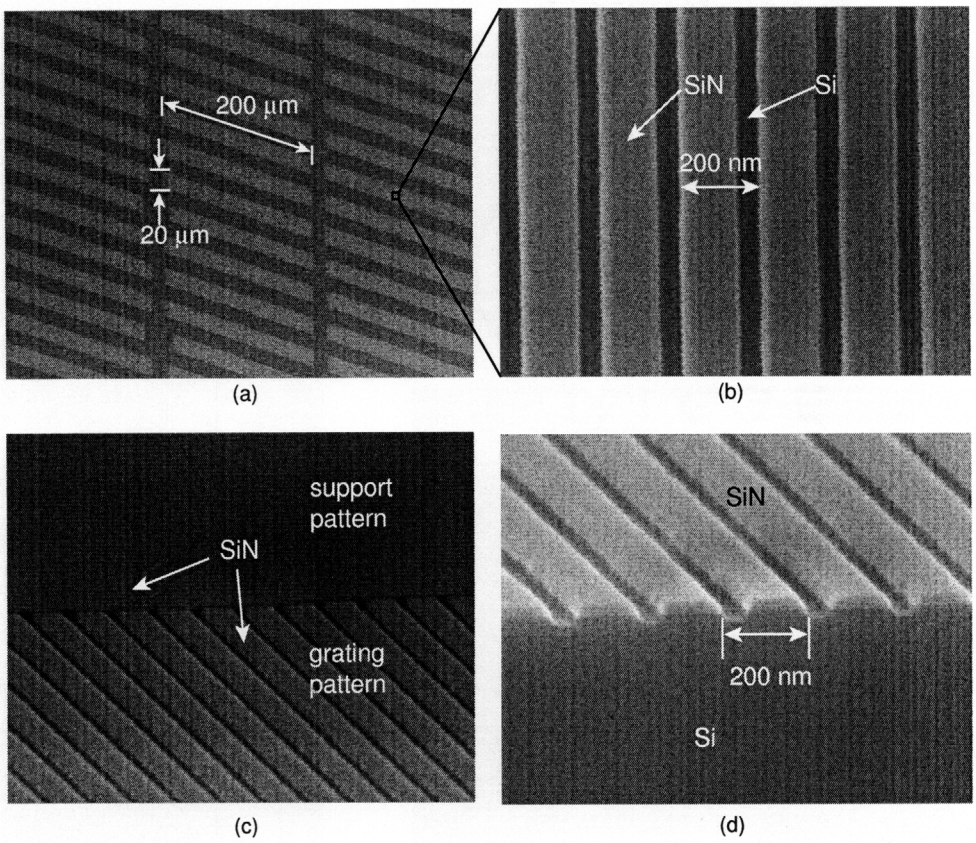


Figure 4-22: SEM images of a nitride etch mask with 2D support lines and 200 nm-period gratings on top of silicon. (a) and (b) are top views, (c) is an angle view, and (d) is a cross-section of the grating pattern. (b) is a blowup of the grating area (brighter parts) in (a).

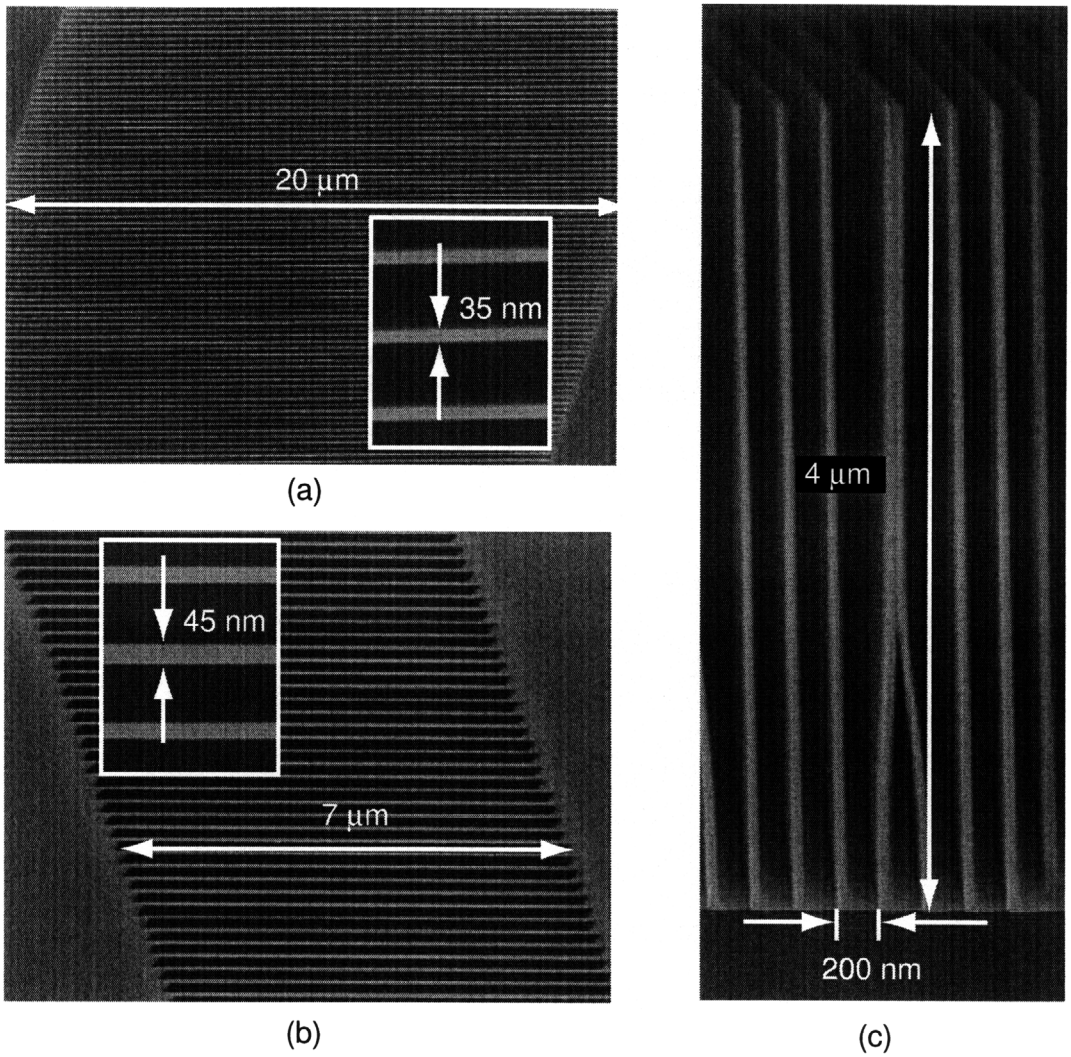


Figure 4-23: SEM images of a 200 nm-period blazed free-standing transmission grating in a 4 $\mu$m-thick $\langle 110 \rangle$ silicon-on-insulator substrate. (a) Top view of the fine grating between a 20 $\mu$m open gap. The linewidth at the top is 35 nm. (b) Bottom view of the grating. The open gap has shrunk to $\sim$7 $\mu$m to due the slanted $\{111\}$ planes. The linewidth is 45 nm, which is consistent with an average sidewall slope of $\sim$0.07°. (c) Cross-section of the grating. The stiction is due to cleaving.

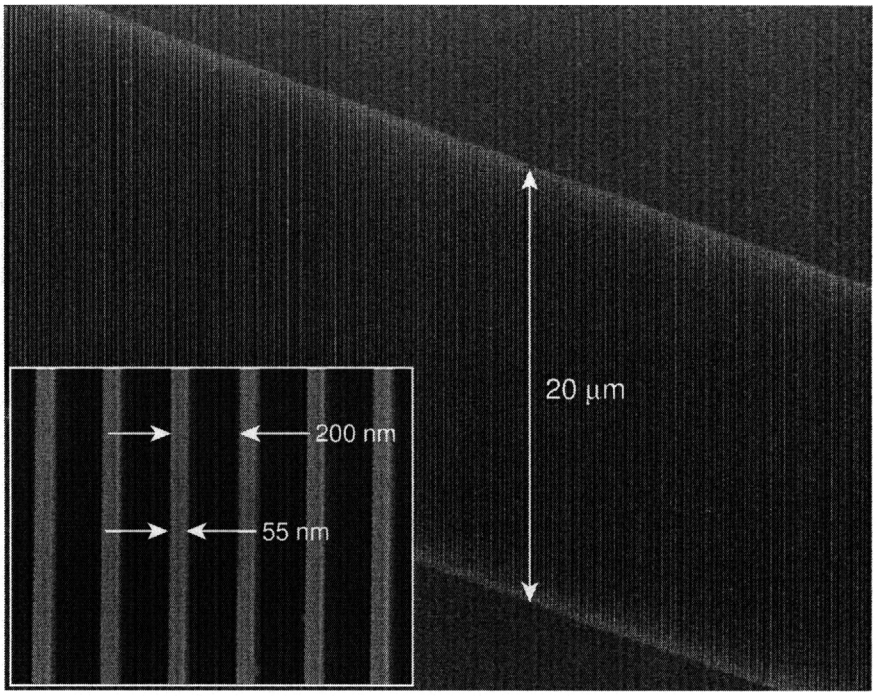


(a)

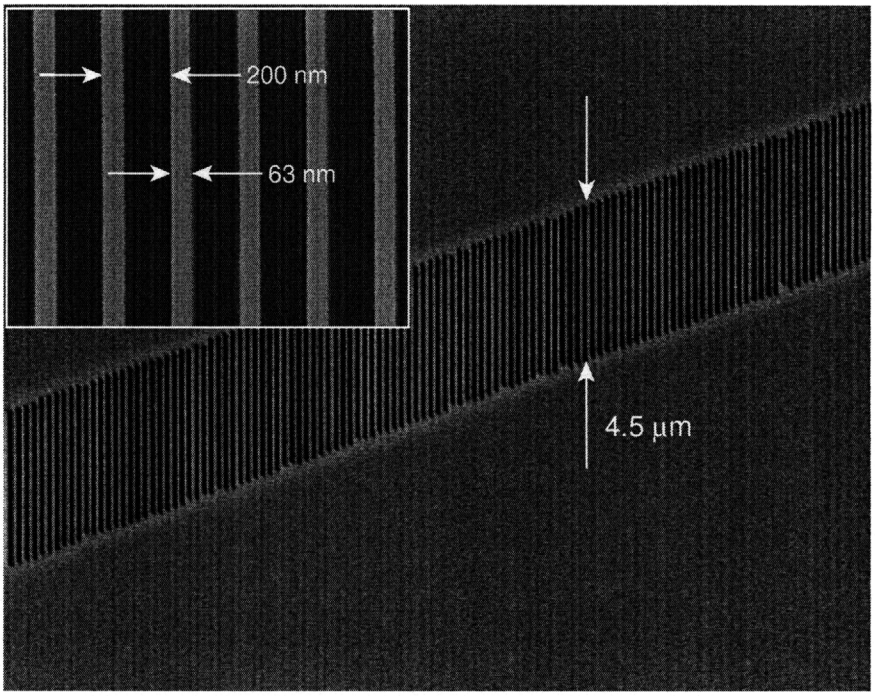


(b)

Figure 4-24: SEM (a) top and (b) bottom view of a 5 $\mu$m-thick 200 nm-period CAT grating between the support lines. The insets show blown-up SEM images. The sample was etched in 50 wt% KOH+0.02 wt% SDSS solution with 30 W ultrasonic agitation.

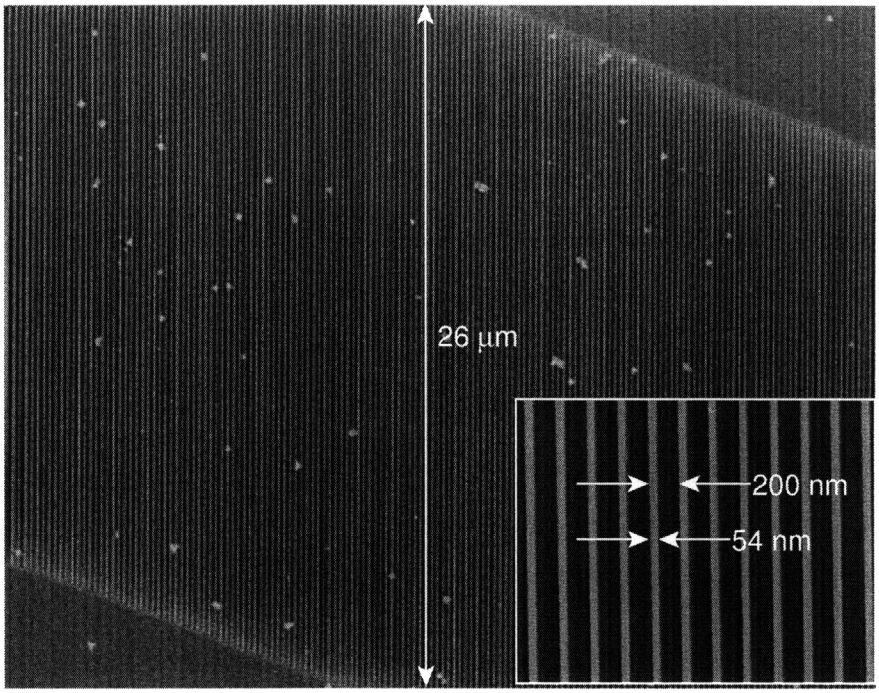


(a)

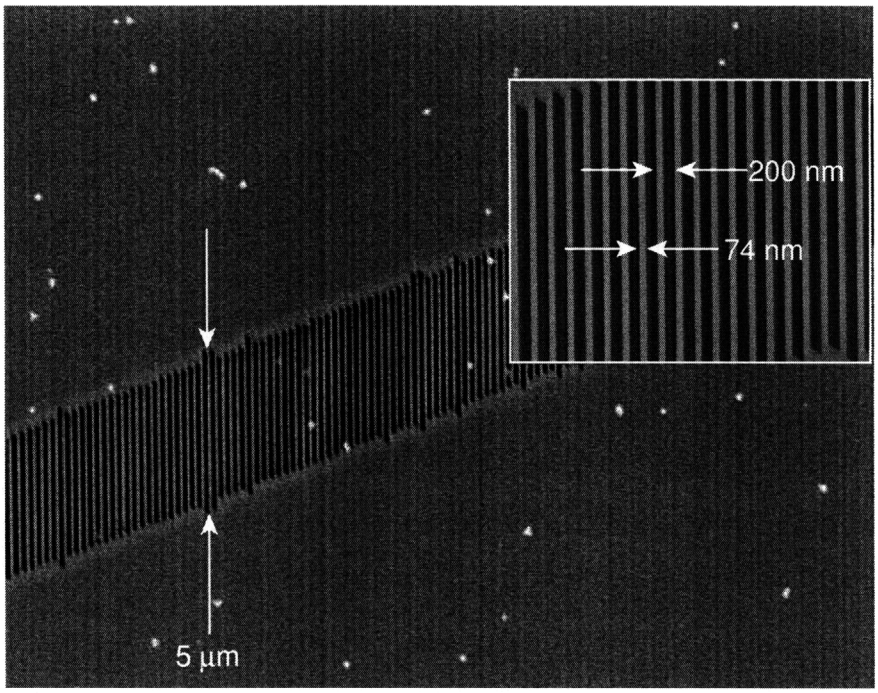


(b)

Figure 4-25: SEM (a) top and (b) bottom view of a 6 $\mu$m-thick 200 nm-period CAT grating between the support lines. The insets show blown-up SEM images. The sample was etched in 50 wt% KOH (no surfactant) solution with 20 W ultrasonic agitation. The white particles seem to be due to contamination during supercritical drying.

liquid $CO_2$, precipitation of remaining etching byproducts or impurity of KOH due to incomplete rinsing, and particles left in the drying chamber. The 200 nm-period CAT gratings were released from thin oxide ($< 100$ nm) in concentrated (48 %) HF to address a stress-induced stiction problem, which will be dealt with in the next chapter in detail. The high aspect-ratio free-standing gratings were dried in a critical point dryer to avoid stiction due to surface tension.

# Chapter 5

# Stress-induced Grating Stiction

In microfabrication processing, structures with a high surface-to-volume ratio easily stick to the substrate or neighboring structures in close proximity, which, for example, happens during air drying after wet processes or developing [70, 71]. Figure 5-1 illustrates an example of structure adhesion due to the capillary force ($F_\gamma$). This well-known "*stiction*" phenomenon occurs when the mechanical restoring force of the structure cannot overcome the capillary force in this case. Once stiction happens for whatever reasons, the stuck structures will not separate again without some finite work because the combined structure has a lower surface energy than separated.

Researchers have worked on the stiction issue, especially related to surface tension, and proposed some methods to alleviate stiction [70–76]. The methods include surface roughening [77], surface coating with hydrophobic layers [78, 79], freeze-drying [80], and supercritical drying [36]. There are also dry-release methods using vapor HF for sacrificial oxide and $XeF_2$ for polysilicon [76]. Kobayashi *et al.* [81] demonstrated a release method with a photoresist support mesh and plasma etch followed.

While the stiction due to capillary forces is well understood and there are many ways suggested to avoid the pattern collapse problems, less attention was paid to a stress-related stiction problem during structure release from buried oxide under a compressive stress in SOI substrates. Even though supercritical drying was used to avoid capillary forces, a stress-induced stiction problem was observed when 200 nm-period free-standing gratings were released from buried oxide using wet HF etching.

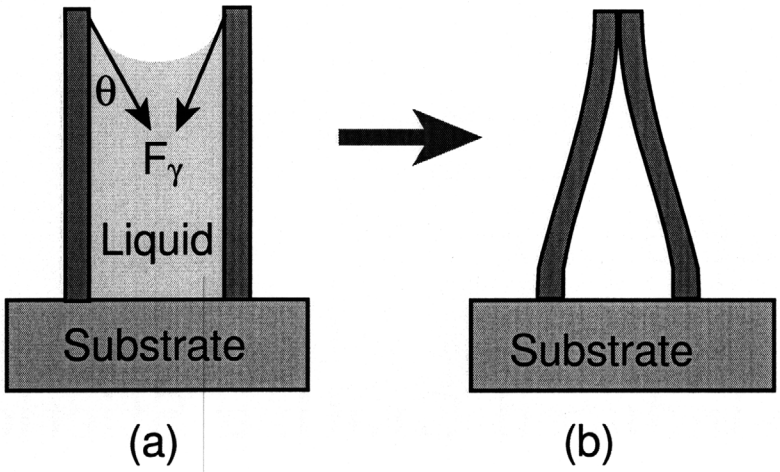


Figure 5-1: A typical stiction problem during air drying of high aspect ratio structures. (a) The capillary force, $F_\gamma$, acting with an angle $\theta$ at the meniscus, causes adhesion of the two bars, resulting in bar sticking after drying (b).

In this chapter, I will present the stiction mechanism related to buckling of the grating bars due to compressive stress in buried oxide. Using finite element modeling (FEM), design strategies to alleviate the stress-induced stiction will be discussed.

## 5.1 Grating Stiction Mechanism

### Observation

Supercritical drying was used to dry the CAT gratings without stiction due to capillary forces. However, a random stiction problem was observed after wet HF etching of buried oxide to release the high aspect ratio CAT gratings produced by KOH etching. While the grating bars on buried oxide did not adhere to each other before HF releasing, they were stuck together right after HF releasing. Figure 5-2 shows observation of stiction after HF releasing. If it was because of minimal surface tension (ideally zero) during supercritical drying, the grating bars on buried oxide could not stand alone without stiction, either. Therefore, in the following, I investigate the origin of this stiction problem and propose a mechanism related to compressive stress in buried oxide. Thermally-grown buried oxide in an SOI wafer usually have a compressive stress in the range of 300 - 400 MPa [82, 83].

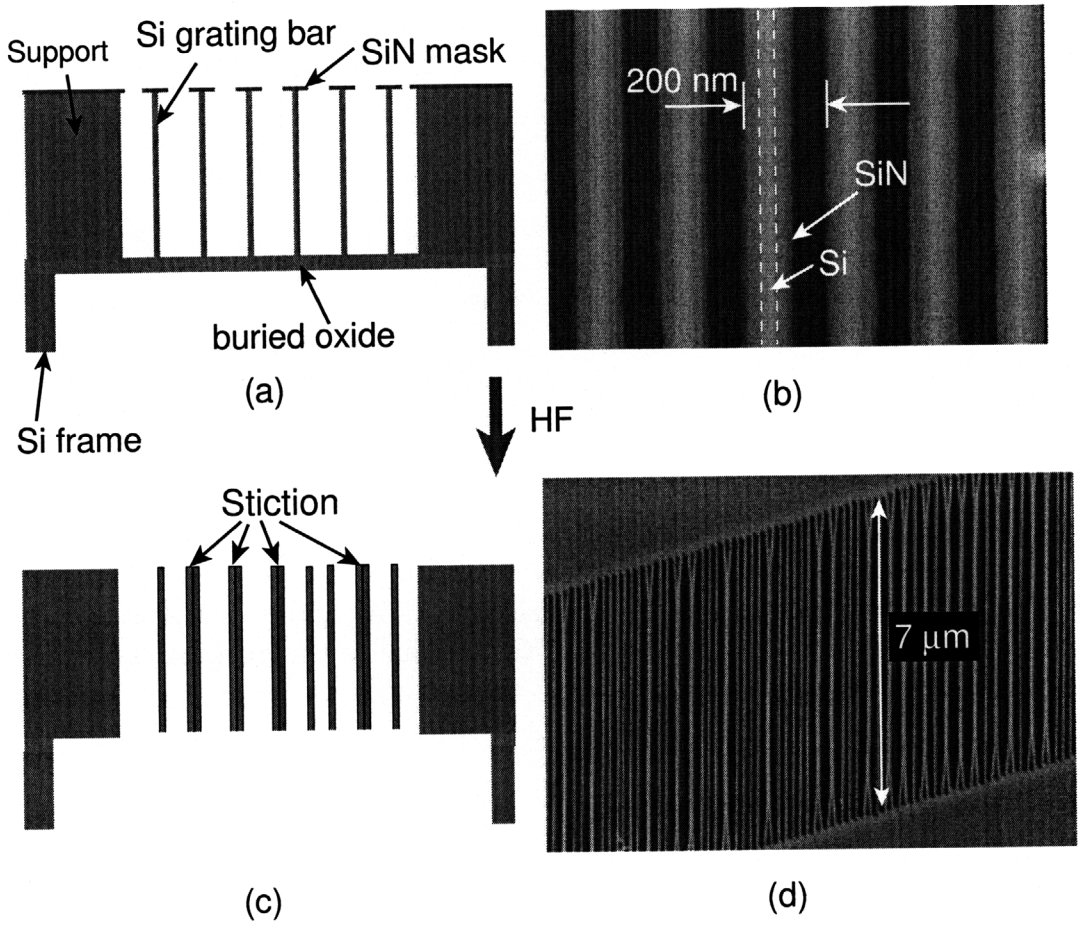


Figure 5-2: Schematics and SEM images of stiction observed with 200 nm-period CAT gratings during HF release. Before HF etching, the grating bars on buried oxide did not adhere to each other after supercritical drying. (b) shows the top view of the grating bars with no stiction. (d) After HF etching, a random stiction problem occurred even though the sample was dried using a critical point dryer.

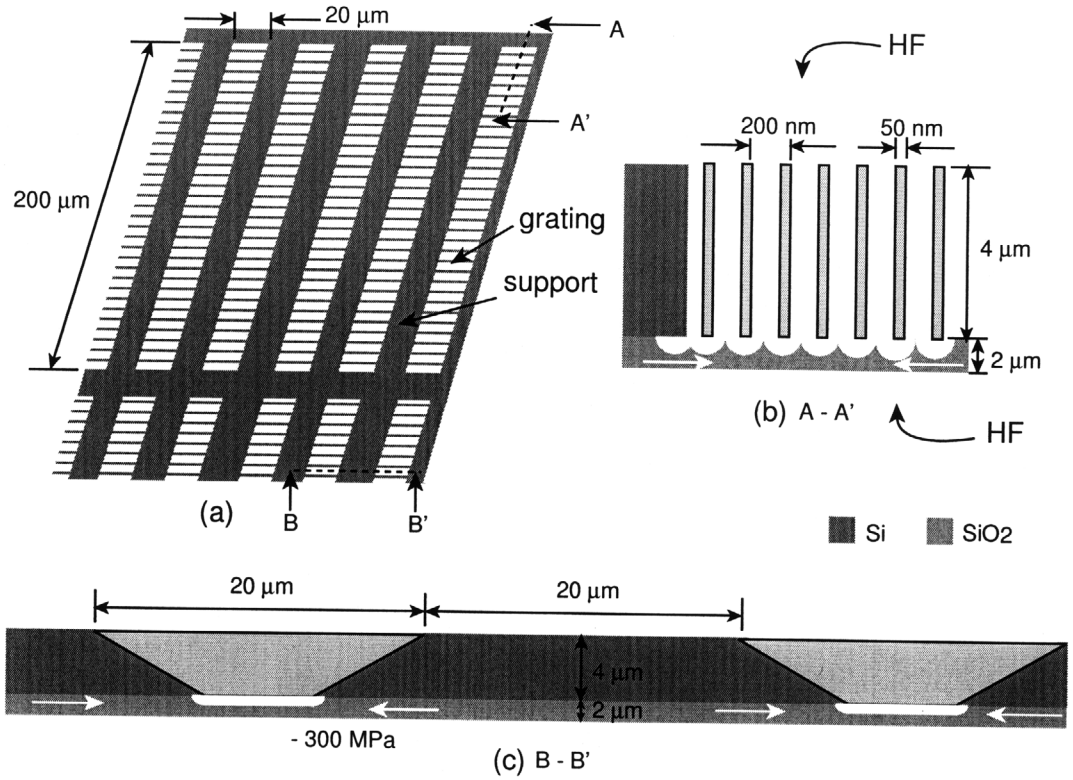


Figure 5-3: Schematics (not drawn to scale) to explain a stiction mechanism during HF etching induced by compressive stress in buried oxide. (a) is an overview of a CAT grating with support mesh, (b) is the section A - A′, and (c) is the section B - B′. The white arrows show compressive force vectors due to the oxide stress which will cause buckling of the grating plane.

### Hypothesis

Let's carefully consider the wet HF release step. Because it is an immersion wet process, HF isotropically etches the buried oxide from the top and bottom of the grating area, whereas the oxide under the support mesh is attacked only from the bottom. As a consequence, the thin grating bars are released and become free-standing earlier than the support mesh which is under a compressive stress due to the remaining oxide. This compression force acts on the thin grating bars and produces buckling, resulting in stiction of the grating bars. Figure 5-3 visualizes this hypothesis with sectional schematics.

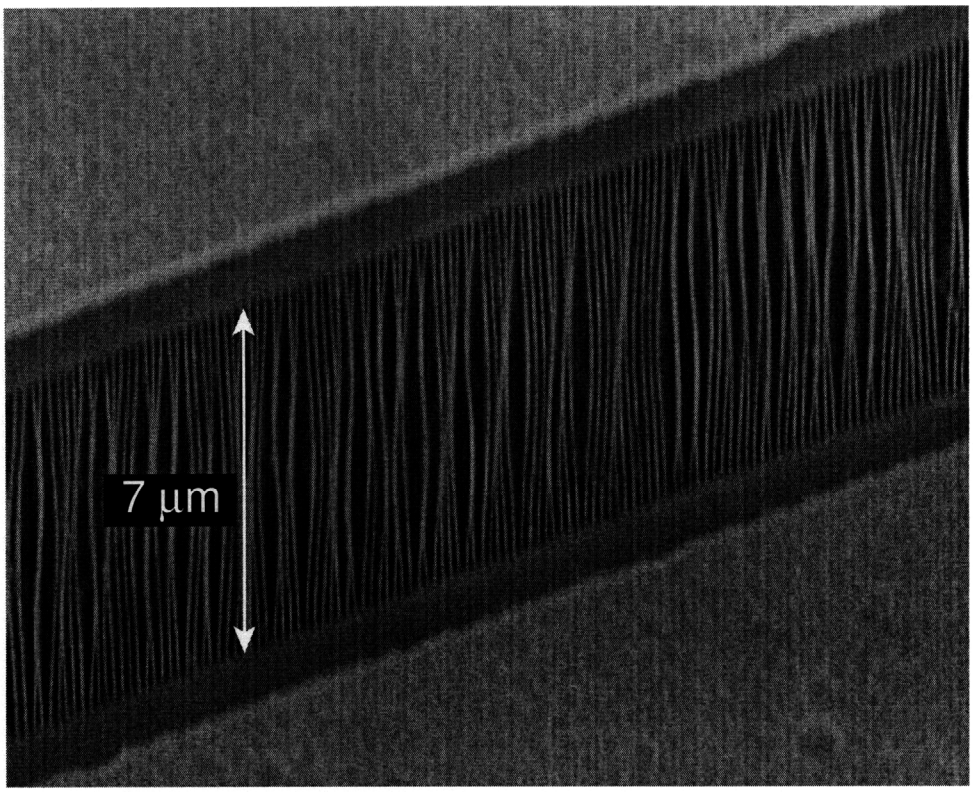


Figure 5-4: SEM image of the bottom of a CAT grating released in HF vapor.

### Experimental proof

Based on the hypothesis, I conducted some experiments to verify the stiction is not related to surface tension but related to the stress. First of all, HF vapor release was tried with a KOH etched grating sample on buried oxide so as to check if stiction occurs even with a dry release process. In order to prevent water condensation during HF vapor etch, a light bulb was used to heat the sample to about 40 °C [84]. The sample was inspected using SEM after HF vapor release and a similar stiction problem was observed, as shown in Fig. 5-4. This result supports the hypothesis because HF vapor also goes all around the sample, and the buried oxide under the grating bars is removed before the support mesh is released, which is the same situation as wet HF release.

A second experiment was to etch the buried oxide from the backside using $CHF_3$ RIE which selectively etches $SiO_2$ without etching silicon. In that way, we can uniformly remove the buried oxide under the grating bars and support mesh at the same

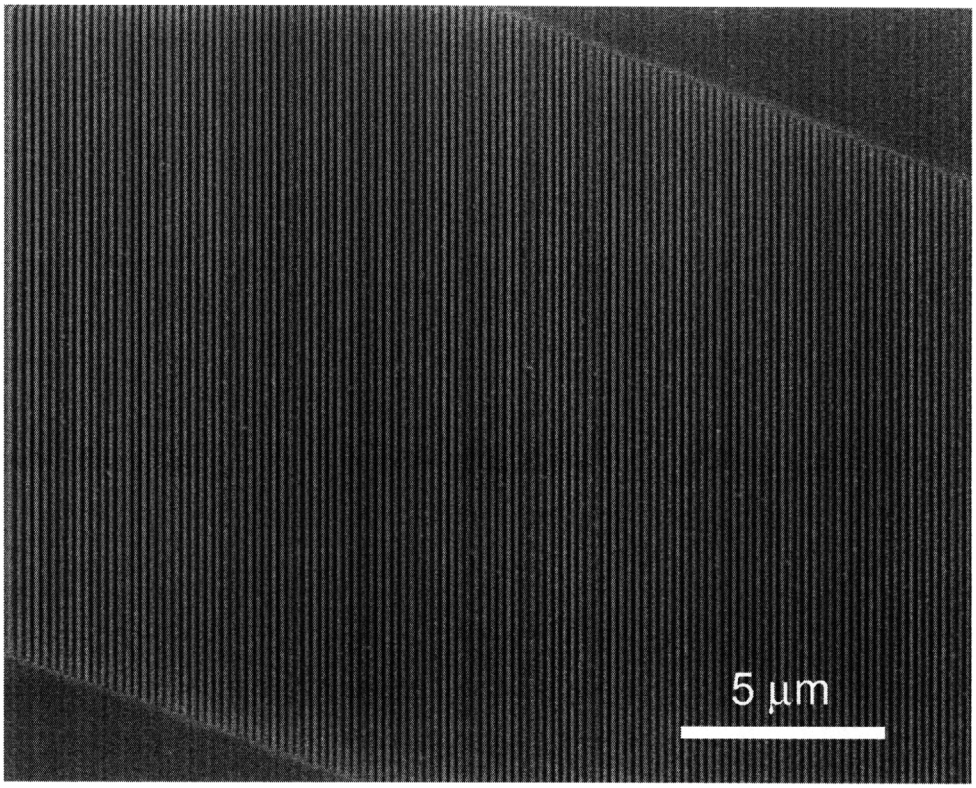


Figure 5-5: SEM image of the top of a CAT grating released by $CHF_3$ RIE on the backside.

time. As a result, there would be no chance for the compression force to act on the grating bars. A supportive result was obtained with this experiment as shown Fig. 5-5. The stiction problem was eliminated by the one-side releasing process. However, this method is not desirable for the CAT grating fabrication because Teflon-like polymers from $CHF_3$ RIE may be deposited around the grating bars, which could impair reflectivity of the grating sidewalls.

If the stress is the origin of stiction, a thinner buried oxide should alleviate the stiction problem because the compressive force is proportional to the oxide thickness. Instead of releasing the grating out of 2 $\mu$m-thick oxide, I first thinned the buried oxide to $\sim$500 nm using buffered-HF (BHF) before KOH etching. The oxide etch rate in BHF is relatively slow ($\sim$100 nm/min), so the thinning process was quite controllable. A few drops of BHF were applied only on the backside using a pipette to keep the front side nitride mask from BHF etching. With the thinned oxide, the sample was etched in KOH and released in concentrated HF. After supercritical drying, much

less sticking damage was observed. With even thinner oxide (< 100 nm), no stiction was observed after HF releasing. The fabrication results described in Chapter 4 were achieved without the stiction problem using this oxide-thinning process.

## 5.2 Analytical Modeling for Buckling of Rectangular Plates

In order to analytically estimate the buried oxide thickness at which the stress-induced stiction would occur due to buckling, we will consider a single grating plane as a rectangular plate constrained along two edges as shown in Fig. 5-6(a). To further simplify the calculations, deflection about the $y$ axis will be only considered. Therefore, we can simplify the 3D plate deflection problem to a 1D beam buckling problem as shown in Fig. 5-6(b).

When an axial compressive force $P$ is uniformly applied to the plate, the governing equation for the beam deflection $w$ is

$$\frac{d^2}{dx^2}\left(EI\frac{d^2w}{dx^2}\right)+\frac{d}{dx}\left(P\frac{dw}{dx}\right)=0, \tag{5.1}$$

where $I$ is the moment of inertia and $E$ is Young's modulus of the beam, which will be replaced with the plate modulus $E/(1-\nu^2)$ after solving this beam deflection problem [76, 85]. $\nu$ is Poisson's ratio of the plate. The moment of inertia is given by

$$I=\frac{bt^3}{12}. \tag{5.2}$$

The boundary conditions for Eqn. (5.1) are given by

$$\left.\begin{array}{l} w=0 \\ \frac{dw}{dx}=0 \end{array}\right\} \text{at } x=0 \text{ and } L. \tag{5.3}$$

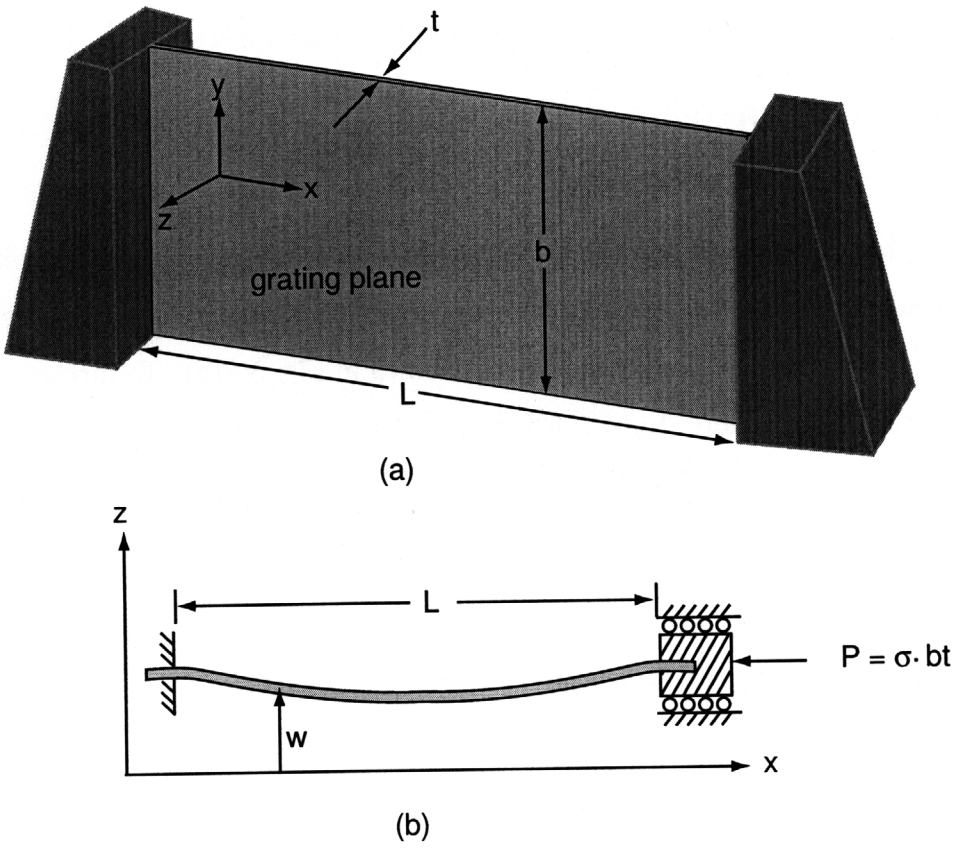


Figure 5-6: (a) A grating plane is modeled as a rectangular plate (L×b×t) with two edges clamped. (b) Simplified beam buckling model assuming cylindrical deflection only about the $y$ axis. The beam is assumed to have a uniform longitudinal compressive stress $\sigma$.

We can write down a trial solution for Eqn. (5.1) with four independent constants.

$$w(x) = c_1 + c_2 x + c_3 \sin\sqrt{\frac{P}{EI}}x + c_4 \cos\sqrt{\frac{P}{EI}}x \tag{5.4}$$

There is a trivial solution $w(x) = 0$, which means the straight beam is one of the equilibrium configurations. Using the boundary conditions, one can find a non-trivial solution

$$w(x) = c_4\left(\cos 2n\pi\frac{x}{L} - 1\right), \tag{5.5}$$

when

$$P = \frac{4\pi^2 n^2}{L^2}EI, \tag{5.6}$$

where $n = 1, 2, 3...$, in equilibrium. At the lowest mode ($n = 1$), the beam deflection curve is

$$w(x) = c_4\left(\cos 2\pi\frac{x}{L} - 1\right), \tag{5.7}$$

and the corresponding critical load $P_{cr}$ is

$$P_{cr} = \frac{4\pi^2}{L^2}EI. \tag{5.8}$$

Substituting the plate modulus and the moment of inertia, the critical load for the plate buckling is

$$P_{cr} = \frac{\pi^2}{3}\frac{E}{1-\nu^2}\frac{bt^3}{L^2}. \tag{5.9}$$

Assuming a uniform stress in the plate, the corresponding critical stress $\sigma_{cr}$ is

$$\sigma_{cr} = \frac{P_{cr}}{bt} = \frac{\pi^2}{3}\frac{E}{1-\nu^2}\left(\frac{t}{L}\right)^2. \tag{5.10}$$

In general, the critical compressive stress of rectangular plates can be given by

$$\sigma_{cr} = K\frac{E}{1-\nu^2}\left(\frac{t}{L}\right)^2, \tag{5.11}$$

where $K$ depends on boundary conditions and the ratio $L/b$ [86].

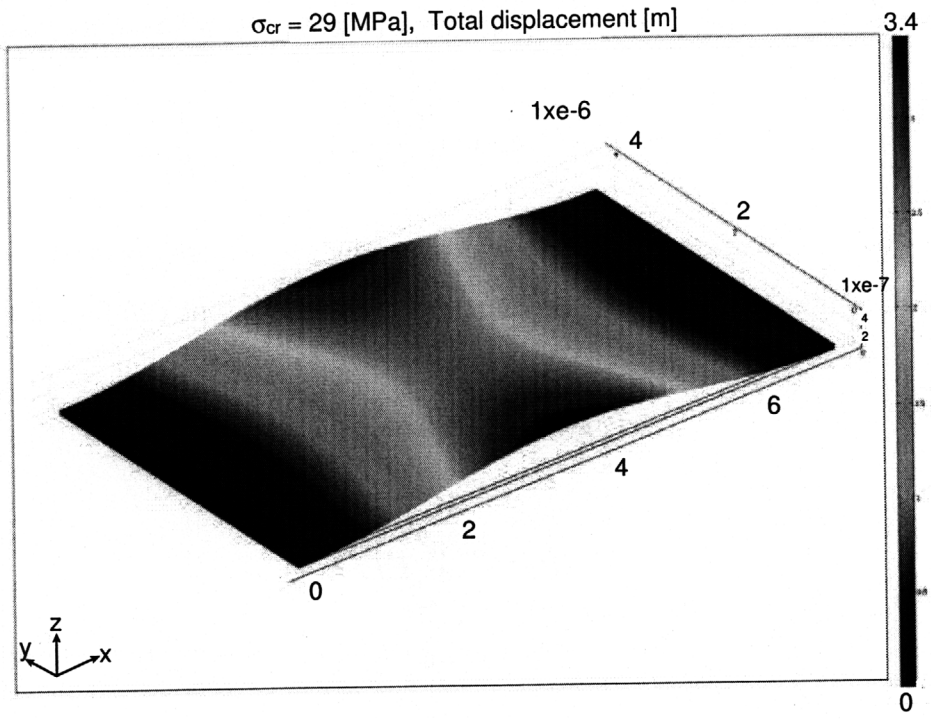


Figure 5-7: Finite element analysis of rectangular plate buckling. The critical stress is 29 MPa. The numbers for the color map are meaningful only when finding relative displacement.

Let's look at a 4 $\mu$m-thick CAT grating bar or plane, for example. Applying Eqn. (5.10) to a silicon* grating plane with $L = 7$ $\mu$m†, $b = 4$ $\mu$m, and $t = 50$ nm, we get $\sigma_{cr} = 30$ MPa. This calculation result is consistent with the FEM result (29 MPa) shown in Fig. 5-7. Next, we need to estimate how much stress the buried oxide would apply to the grating plate. For a rough estimation, let's assume the compression force ($P$) due to the residual stress ($\sigma_0$‡) of oxide is uniformly distributed along the grating bar. Considering one period ($p = 200$ nm) of the grating, the stress in the grating plane ($\sigma_g$) is

$$\sigma_g = \frac{P}{bt} = \frac{\sigma_0 ph}{bt}, \tag{5.12}$$

*Assume silicon has isotropic material properties, $E = 170$ GPa and $\nu = 0.28$.
†The plate length $L$ is a typical opening width at the bottom of the 4 $\mu$m-thick CAT grating.
‡$\sigma_0 \sim 300$ - 350 MPa

where $h$ is oxide thickness. Buckling occurs when $\sigma_g > \sigma_{cr}$, that is,

$$\frac{\sigma_0 ph}{bt} > \frac{\pi^2}{3}\frac{E}{1-\nu^2}\left(\frac{t}{L}\right)^2. \tag{5.13}$$

Rearranging Eqn. (5.13) with respect to $h$, the buckling condition is given by

$$h > \frac{\pi^2}{3}\frac{E}{1-\nu^2}\frac{bt^3}{\sigma_0 pL^2}. \tag{5.14}$$

Substituting the geometric parameters of the example above and material properties of silicon, we expect buckling when the oxide thickness is larger than 0.1 $\mu$m. This rough estimation is consistent with the experimental result described in the previous section where no stiction problem was observed when the buried oxide was thinner than 0.1 $\mu$m.

## 5.3 Finite Element Analysis of Grating Bar Buckling

The analytical model, described in the previous section, provides a rough estimation for buckling of rectangular plates under uniform compressive stress. However, more accurate analysis for the actual trapezoidal grating planes is desired not only to examine the previous experimental results but also to design new support meshes and oxide thickness that would not cause the stiction problem. The assumption of uniform stress distribution in the rectangular plate also needs to be changed considering that the actual stress source is in the buried oxide underneath the support mesh. Using a commercial finite element modeling (FEM) tool, *COMSOL Multiphysics* [87], I analyzed buckling of a grating plane between support lines on top of buried oxide which is believed to cause the stiction problem during wet HF release. In order to reduce simulation load, I used a half model of a grating plane within one period (200 nm) based on geometric symmetry. Figure 5-8 shows a buckling analysis example for half of a 40 nm-thick grating plane between 5 $\mu$m-open support lines at the bottom. With

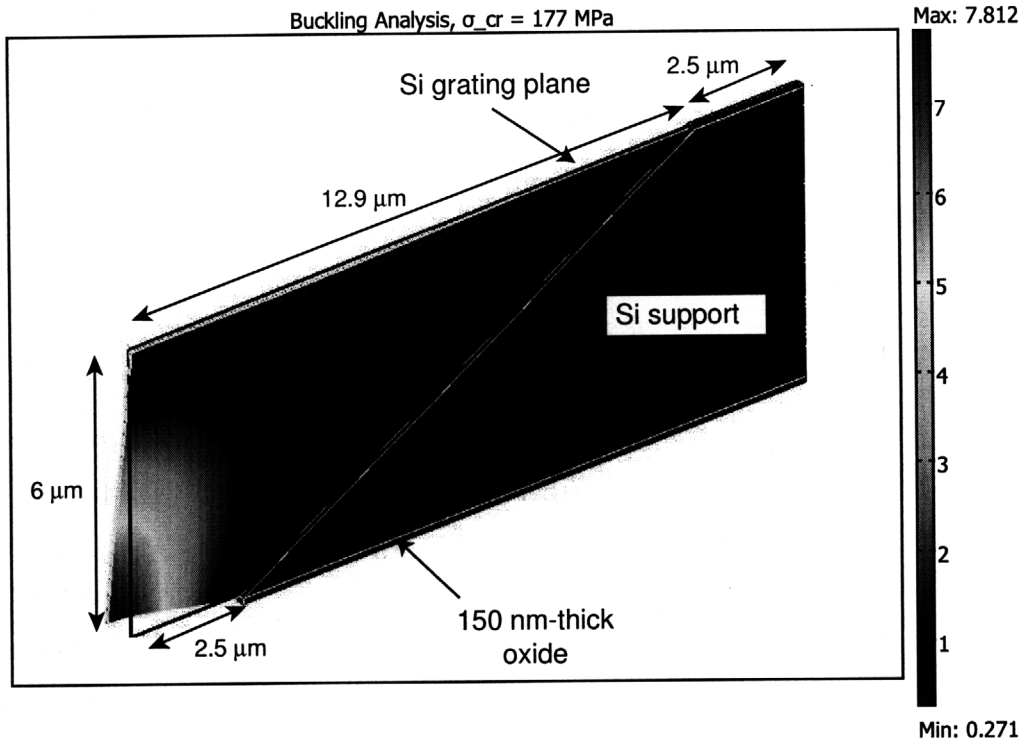


Figure 5-8: An example FEM of grating plane buckling. The critical stress is 177 MPa. The numbers for the color map are meaningful only when finding relative displacement.

150 nm-thick oxide, the grating is predicted to buckle when the oxide stress is larger than 177 MPa. Considering usual thermal oxide stress (> 300 MPa), this structure in the example would buckle and cause the stiction problem.

Generally speaking, the oxide stress is unavoidable even though we might modify it by controlling its deposition temperature [88]. In our case, the stress is fixed by the SOI wafer manufacture. Therefore, we instead would like to change the design of the support mesh and oxide thickness which are expected to have larger critical stresses than the buckling limit estimated by simulation. Changing the oxide and grating thicknesses using FEM, I obtained critical stresses as a function of the bottom opening width of support meshes as shown in Figs. 5-9 and 5-10 for 4 $\mu$m and 6 $\mu$m-thick CAT gratings, respectively. Buckling would occur when the curves are below the given oxide stress ($\sigma_0$) of 300 MPa. The results show that thinner oxide increases the critical stress, which means there is less chance to buckle. Although thicker

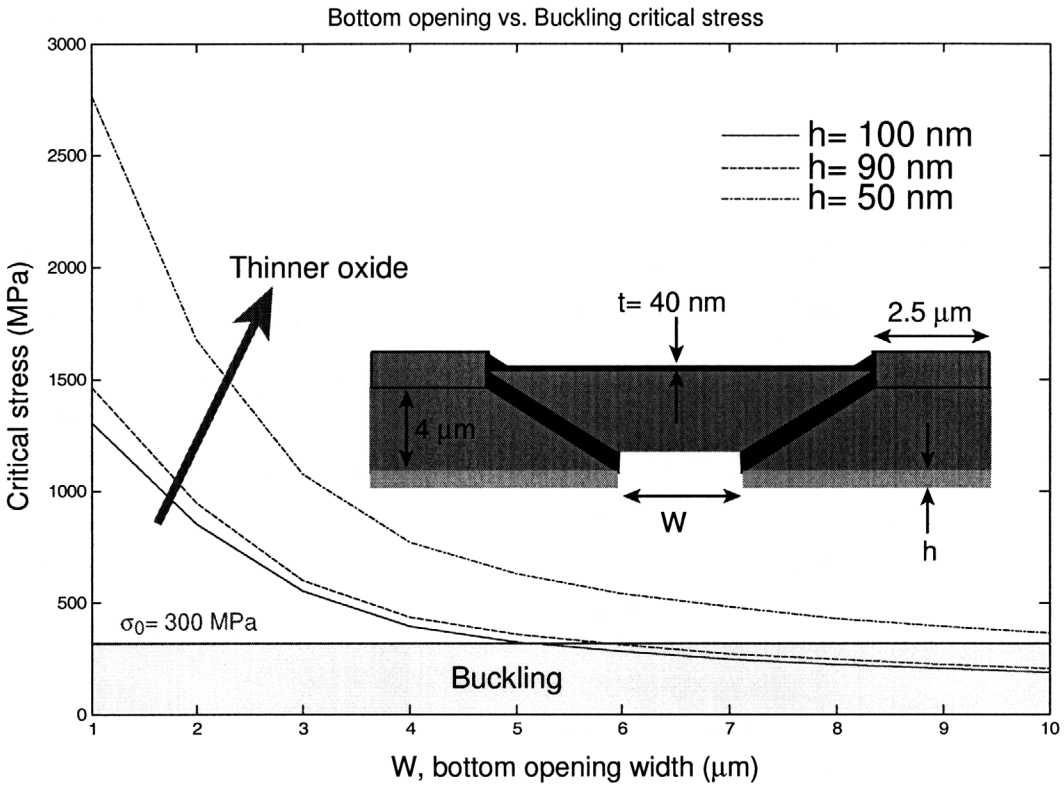


Figure 5-9: FEM buckling simulation results of a 4 $\mu$m-tall CAT grating bar as a function of bottom width. As the oxide thickness $h$ decreases, the critical stress increases. The grating thickness $t$ is assumed to be 40 nm. The straight solid line is the given oxide residual stress (300 MPa).

grating bars would also be better for structural stability without buckling, the grating thickness has already been defined by the CAT grating geometry. Based on these simulation results, I modified the support mesh width and buried oxide thickness accordingly and achieved stiction-free CAT gratings.

In this chapter, I analyzed buckling of high aspect-ratio grating bars in SOI wafers suffering from a stress-induced stiction problem during wet HF release. The support structure for free-standing grating bars and buried oxide thickness were designed to avoid the stiction problem based on prediction by buckling simulation. Experimental results were consistent with the simulation results and the grating bars were successfully released from the buried oxide without stiction.

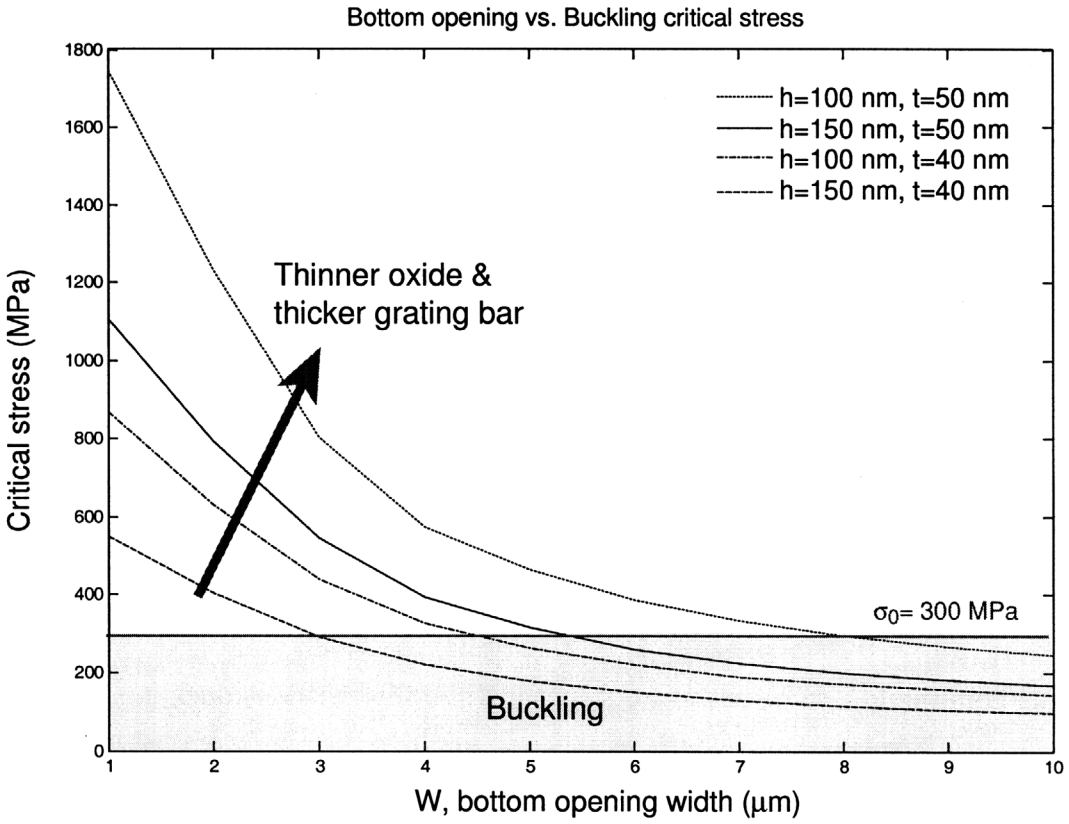


Figure 5-10: FEM buckling simulation results of a 6 $\mu$m-tall CAT grating bar as a function of bottom width. As the oxide thickness $h$ decreases and the grating thickness $t$ increases, the critical stress increases. The straight solid line is the given oxide residual stress (300 MPa).

# Chapter 6

# Support Structure Engineering with Plasma Etching and Wet Polishing

Support structures provide the free-standing gratings with mechanical strength and are essential to hold the membrane including the gratings. However, the silicon support structure for the CAT gratings absorbs the incident x rays, resulting in a decrease of the grating effective area. As a consequence, overall diffraction efficiency with respect to the incident x rays decreases even though the diffraction efficiency of a CAT grating, normalized with the open area fraction, is much higher than that of a traditional transmission grating with the same effective area. Therefore, it is important to optimize the support structure to minimize area loss while holding the free-standing grating structure. However, KOH anisotropic etching, utilized to develop the CAT gratings, decreases the open area fraction during deep etching due to the 30°-tilted $\{111\}$ planes while forming very smooth and straight $\{111\}$ sidewalls. Figure 6-1 illustrates this geometrical constraint for KOH etching of $\langle 110 \rangle$ silicon [32]. From the geometry, the maximum etch depth $D_{max}$ and the bottom open length $L_B$ are

$$D_{max} = \frac{L}{2\sqrt{3}} \tag{6.1}$$

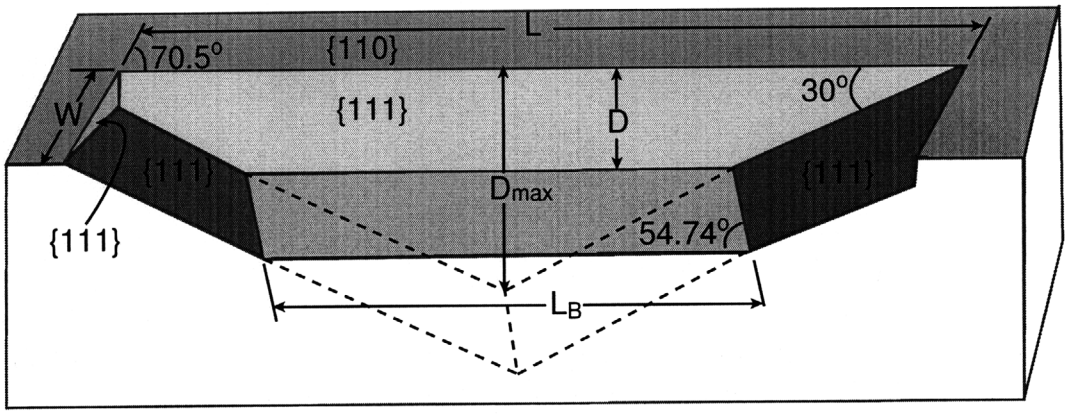


Figure 6-1: Geometry of a groove in ⟨110⟩ silicon produced by KOH etching [32].

and

$$L_B = L - 2\sqrt{3}D + \frac{3\sqrt{2}}{4}W, \tag{6.2}$$

respectively. The CAT gratings have been fabricated with these geometrical constraints. For example, Fig 6-2 shows the geometry of the CAT gratings confined between support lines. The 40 $\mu$m opening at the top ends up being only 5 $\mu$m after etching down to 10 $\mu$m [Fig 6-2(a)]. We may design a support structure with a wider top opening length $L$ to increase the ratio $L_B/L$, but this may lead to mechanical instability.

Other etching methods are desired to effectively engineer the support structure because it is difficult to design with the geometrical constraints involved in the KOH etching process. Reactive ion etch (RIE) is a directional etching method not depending on crystallographic orientations even though there are remaining issues with the sidewall slope angle and roughness [51, 89] as discussed in Chapter 3. Recently, Agarwal *et al.* [90] proposed a polishing method using KOH+IPA to smooth sidewall scalloping after deep RIE (DRIE) based on the fact that KOH solution quickly etches non-⟨111⟩ planes. In this chapter, I present feasibility test results of a RIE process followed by KOH polishing to fabricate high aspect-ratio gratings with a 200 nm period.

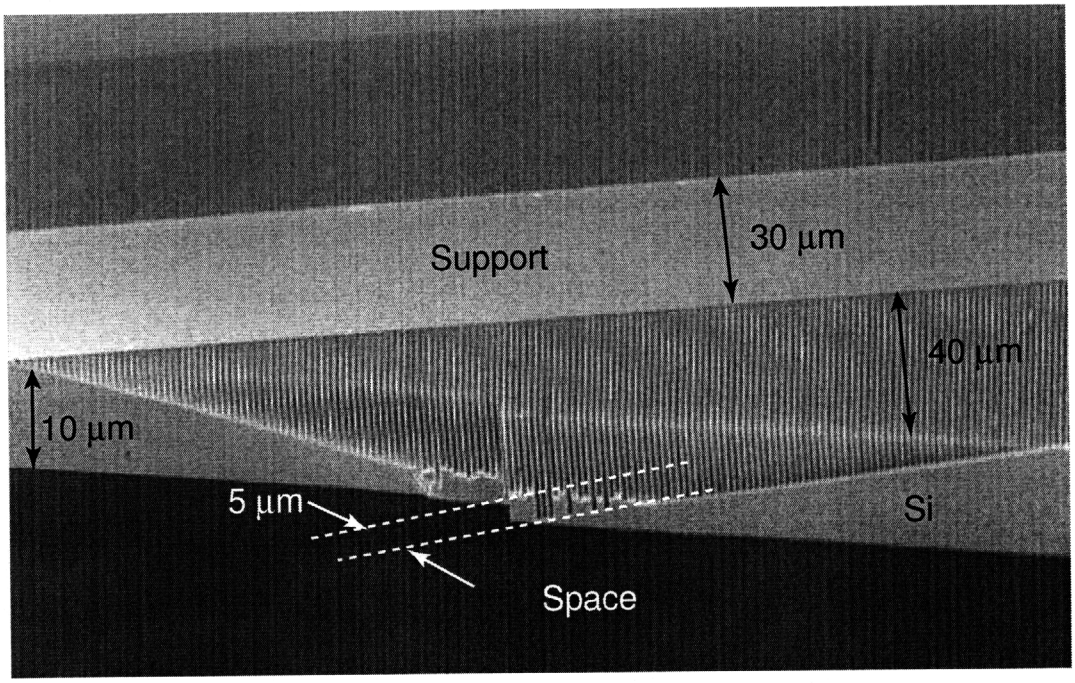


(a)

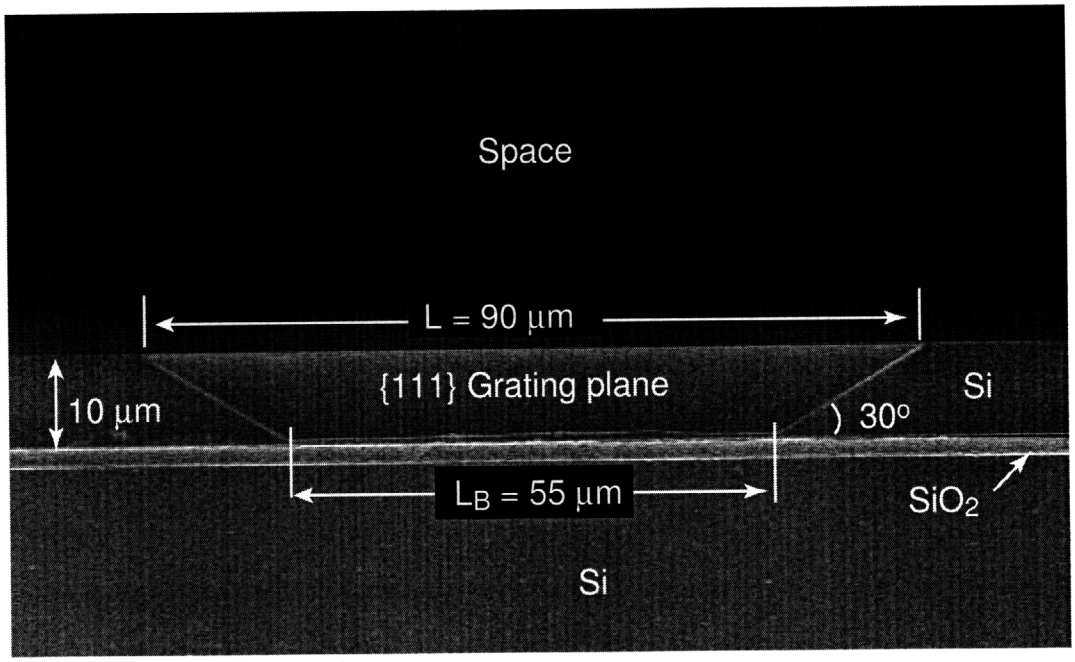


(b)

Figure 6-2: Cross section SEM images of 574 nm-period CAT gratings between support lines with (a) 40 $\mu$m and (b) 90 $\mu$m opening at the top.

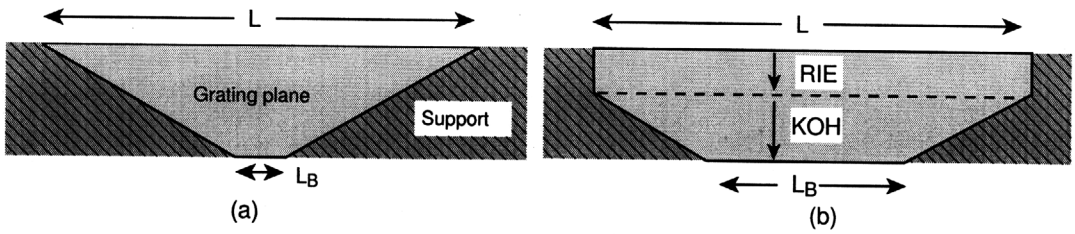


Figure 6-3: Schematics of a CAT grating plane produced by (a) only KOH etching (b) partial RIE + KOH etching.

## 6.1 Reactive Ion Etching + KOH Polishing

DRIE has been used to fabricate high aspect-ratio structures in silicon with a micrometer scale for various MEMS applications [51]. However, sidewall scalloping in a range of 10 - 100 nm leaves difficulty in applying DRIE to fabrication of nanometer-scale structures with an aspect ratio larger than 50 [91]. On the other hand, chlorine and bromine-based RIE processes have been broadly used to anisotropically etch silicon with nanoscale features [92, 93]. However, the maximum aspect ratio of the nanostructures has been demonstrated only in a range of 20 - 30 due to sidewall tapering [92–94]. Therefore, it might not be practical to use a RIE process to completely etch the CAT grating with an aspect ratio of 100 - 150. Instead, we can use the RIE process for a partial etch of the grating and complete etching with KOH as shown in Fig 6-3. Using RIE, we can obtain a larger bottom opening or $L_B/L$ than using KOH etching. In addition, subsequent KOH etching would polish the sidewall, that is, straighten the slope and smooth sidewall roughness. In this section, I will describe a RIE process with hydrogen bromide (HBr), followed by KOH polishing. Compared to chlorine-based RIE, HBr RIE processes have been reported to have superior directionality and selectivity to etch masks such as silicon dioxide and photoresist [95]. However, etch rates in HBr RIE are generally slower than those in $Cl_2$ RIE.

### Patterning

$\langle 110 \rangle$ silicon wafers with 400 nm-thick thermal oxide were used as substrates. In order to minimize reflections from the substrate and facilitate pattern transfer to the thick oxide, a stack of 15 nm of $SiO_2$ and 15 nm of $Ta_2O_5$ on top of 400 nm-thick ARC

Table 6.1: Pattern transfer process parameters

| | Gas | Flow (sccm[a]) | Pressure (mTorr) | $V_{DC}$ or Power | Etch Rate (nm/min) |
|---|---|---|---|---|---|
| Interlayer[b] | $CHF_3$ | 18 | 10 | 350 V | 25 |
| ARC | $O_2$ | 20 | 7 | 200 W | 160 |
| $SiO_2$ | $CHF_3$ | 18 | 10 | 350 V | 35 |

[a] standard cubic centimeter per minute
[b] 15 nm of $SiO_2$ + 15 nm of $Ta_2O_5$

(BARLi, AZ Electronic Materials) was prepared for the trilevel resist process [96]. Figure 6-4 depicts the multilayer stacks and corresponding simulated reflectivity at the boundary between the resist and underlayers. When using 15 nm of $SiO_2$ alone as the interlayer (Fig. 6-4(a)), we can get a low reflectivity with 140 nm-thick BARLi, which is not thick enough for an etch mask for pattern transfer to the 400 nm-thick oxide layer using $CHF_3$ or $CF_4$ RIE. Instead of using $SiO_2$ for the interlayer, we can use 15 nm of $Ta_2O_5$ to reduce the reflectivity to 1% with 400 nm of BARLi (Fig. 6-4(b)). Optionally, we can achieve a very low reflectivity (0.2%) at 400 nm ARC thickness with a double interlayer consisting of $SiO_2$ and $Ta_2O_5$* (Fig. 6-4(c)). On top of the multilayer stack, 200 nm-thick photoresist (PFI-88a2, Sumitomo Corp.) was spin-coated after vapor hexamethyldisilazane (HMDS) treatment for adhesion promotion. Using the multilevel resist process, I patterned 200 nm-period gratings using the Nanoruler. Figure 6-5 shows a SEM micrograph of the resist after wet development.

Figure 6-6 shows pattern transfer into the interlayer and ARC using $CHF_3$ and $O_2$ RIE, respectively. With the remaining interlayer and ARC as an etch mask, the 400 nm-thick oxide was etched using $CHF_3$ RIE. Figure 6-7 shows the slightly tapered etch profile in the oxide because of ARC erosion during the long $CHF_3$ RIE. The RIE process parameters for the pattern transfer are detailed in Table 6.1.

*$SiO_2$ on top of $Ta_2O_5$

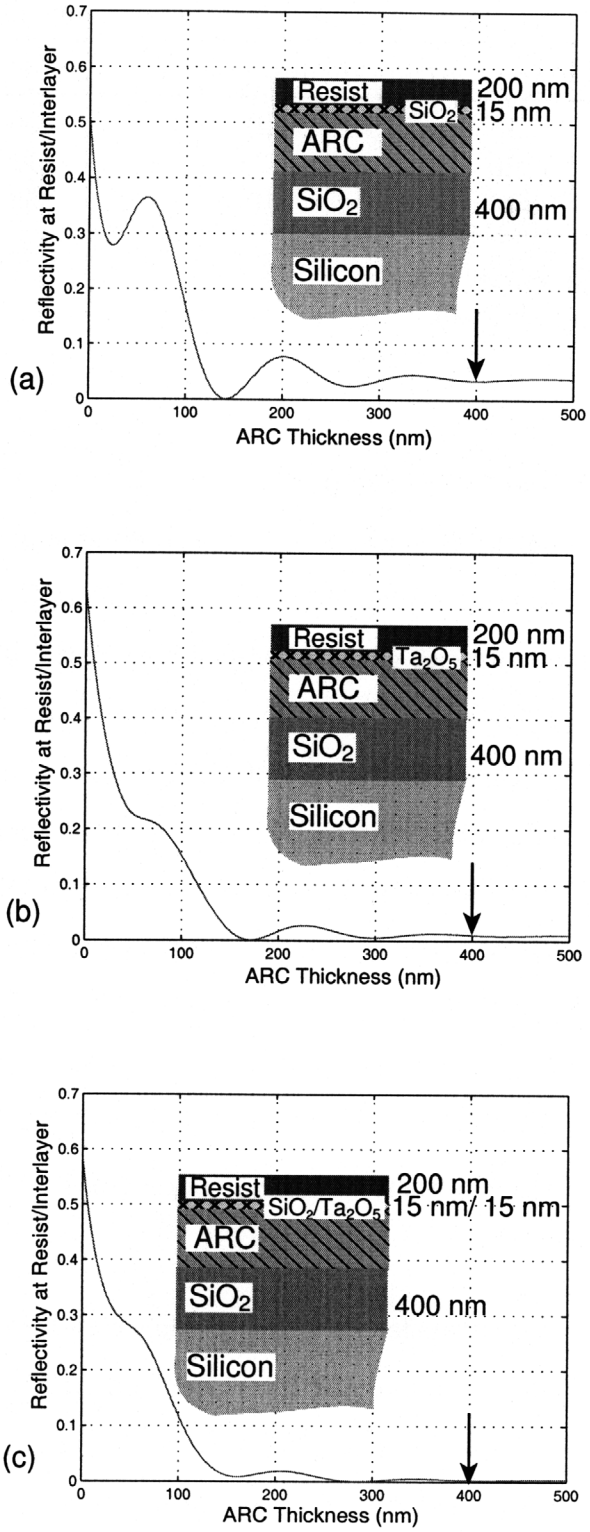


Figure 6-4: Multilayer stack design for interference lithography on a silicon substrate with 400 nm-thick thermal oxide. The interlayers are (a) 15 nm of $SiO_2$, (b) 15 nm of $Ta_2O_5$, and (c) 15 nm of $SiO_2$ + 15 nm of $Ta_2O_5$. The arrows point the target ARC thickness at 400 nm required for an efficient pattern transfer.

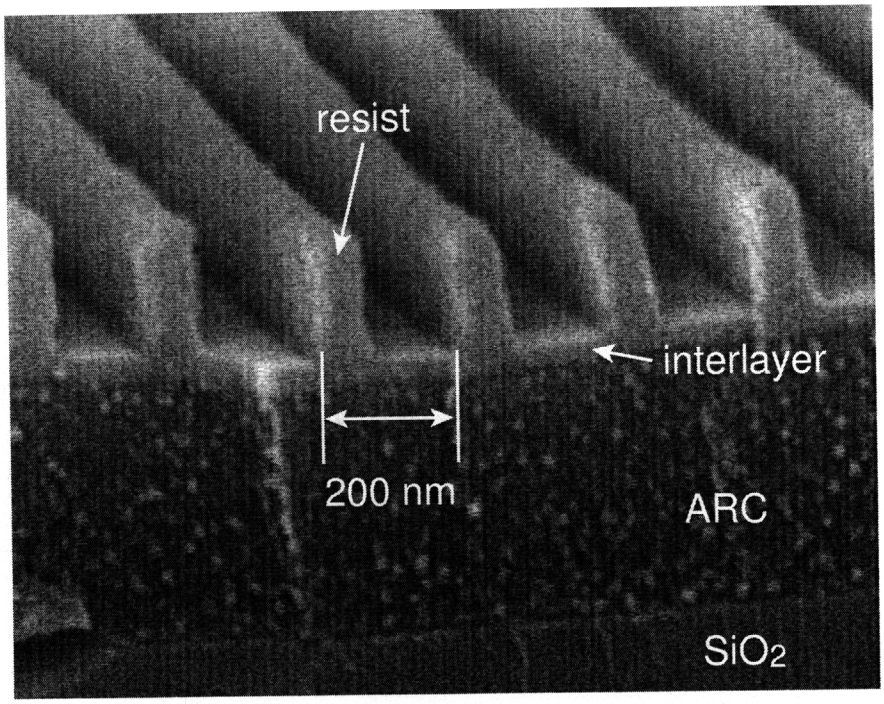


Figure 6-5: SEM micrograph of a 200 nm-period grating in resist over 400 nm ARC and an interlayer (15 nm of $SiO_2$ + 15 nm of $Ta_2O_5$).

### HBr RIE

For testing purposes, ⟨100⟩ silicon wafers with 200 nm-thick oxide were patterned using the similar process described in the previous section. Figure 6-8 shows the 200 nm-thick oxide mask on silicon.

A conventional parallel plate RIE system (PlasmaTherm SLR770) was used for etching tests. With the 200 nm-thick oxide mask, I performed HBr RIE tests with three different bias voltages at a fixed chamber pressure of 2 mTorr and gas flow of 20 sccm. The results are shown in Figure 6-9. As the bias voltage increases from 100 to 350 $V_{DC}$ [Figs. 6-9(a)-(c)], directionality increases while the selectivity to the $SiO_2$ mask decreases. With 350 V [Fig. 6-9(c)], the oxide mask was completely removed after one hour etching because of physical etching by high energy ion bombardment. While etching deeper, we found that the etch profile became wavy as shown in Fig. 6-9(d). Based on the result of one hour etch with 200 V and 2 mTorr, the silicon etch rate was about 15 nm/min with a selectivity of ~10 with respect to $SiO_2$. However, as the trenches become deeper and narrower, the silicon etch rate decreases and

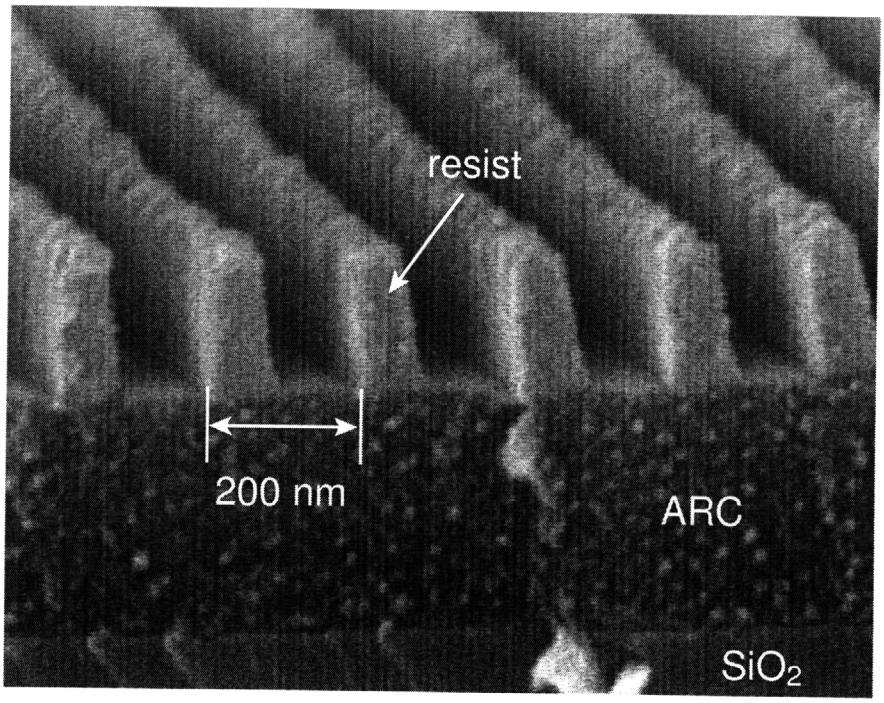


(a)

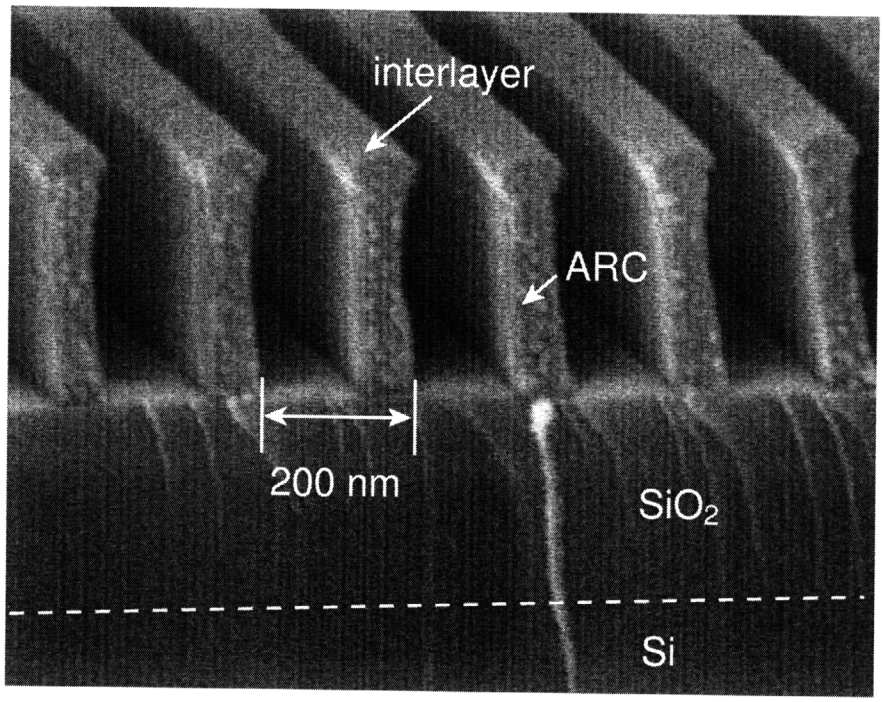


(b)

Figure 6-6: SEM micrographs of 200 nm-period gratings (a) after interlayer etch with $CHF_3$ RIE and (b) ARC etch with $O_2$ RIE.

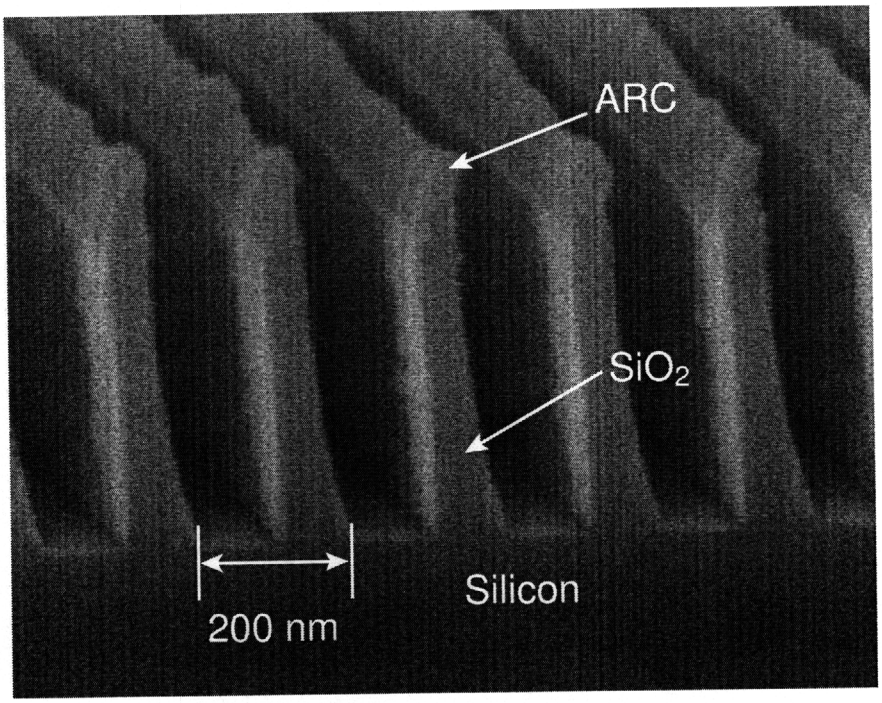


(a)

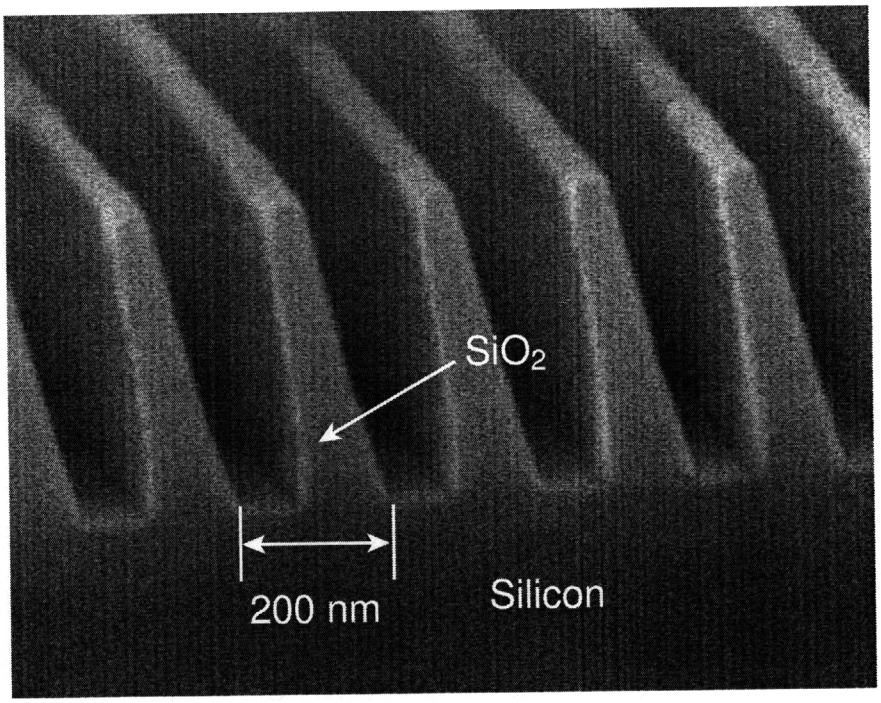


(b)

Figure 6-7: SEM micrographs of 200 nm-period gratings in 400 nm-thick oxide after (a) $CHF_3$ RIE and (b) removing ARC with an RCA clean. This oxide pattern will serve as an etch mask for HBr RIE.

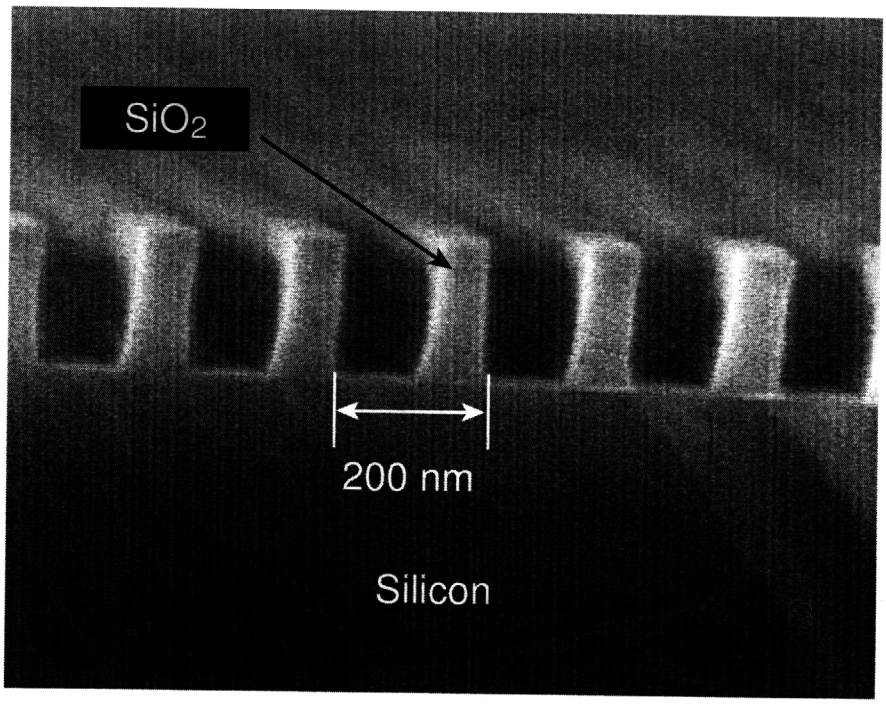


Figure 6-8: SEM micrograph of a 200 nm-period grating in 200 nm-thick oxide.

consequently the selectivity decreases as well.

Next, etch profile dependence on the chamber pressure was studied with a fixed bias voltage of 200 V. Figures 6-10(a) and (b) compare the etch profile of 200 nm-period gratings etched for one hour with 2 mTorr and 10 mTorr. With 10 mTorr, the etch rate slightly increased because of more gas atoms available to be ionized, but the profile is less directional because of more ion collisions during transit across the sheath in the gas phase [97].

Based on the etching tests with ⟨100⟩ wafers with the 200 nm-thick oxide mask, I performed HBr RIE with ⟨110⟩ wafers with the 400 nm-thick oxide mask shown in Fig. 6-7(b). Figure 6-11 shows the etch result after two-hour HBr RIE with the chamber pressure of 2 mTorr and the bias voltage of 200 V. The remaining 205 nm-thick oxide mask will serve as an etch mask during subsequent KOH polishing.

### KOH Polishing

The 200 nm-period grating samples etched using HBr RIE had a sidewall slope with a wavy etch profile as shown in Fig. 6-11. I polished these gratings using a KOH

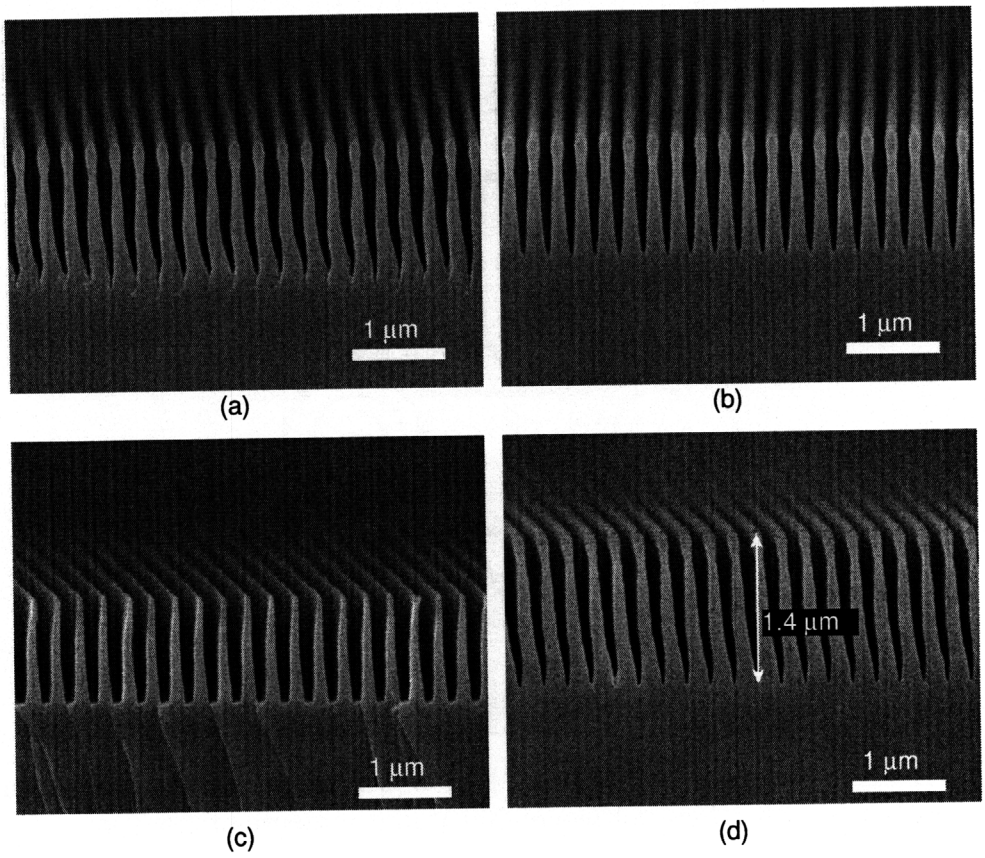


Figure 6-9: SEM micrographs of 200 nm-period gratings in silicon etched using HBr RIE with different bias voltages and etch times. (a) 100 V for two hours, (b) 200 V for one hour, (c) 350 V for one hour, and (d) 200 V for 1.5 hour. Note that the oxide mask in (c) was completely removed during HBr etching.

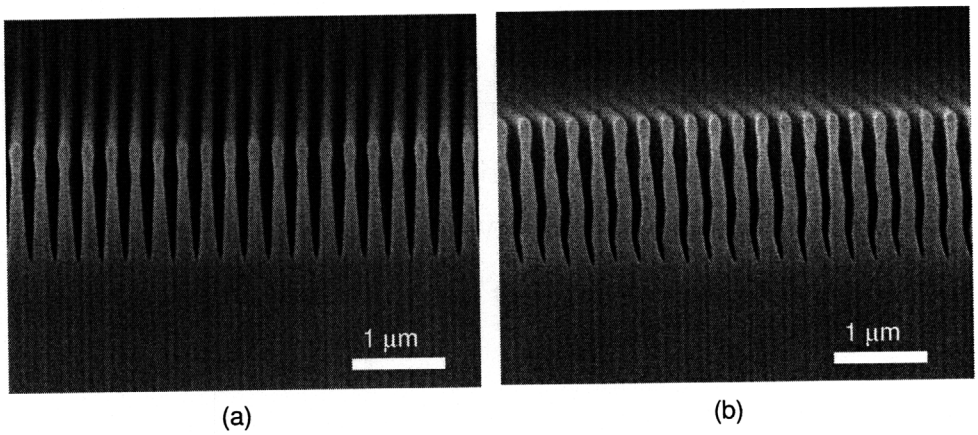


Figure 6-10: SEM micrographs of 200 nm-period gratings in silicon etched using HBr RIE for one hour with two different chamber pressures of (a) 2 mTorr and (b) 10 mTorr.

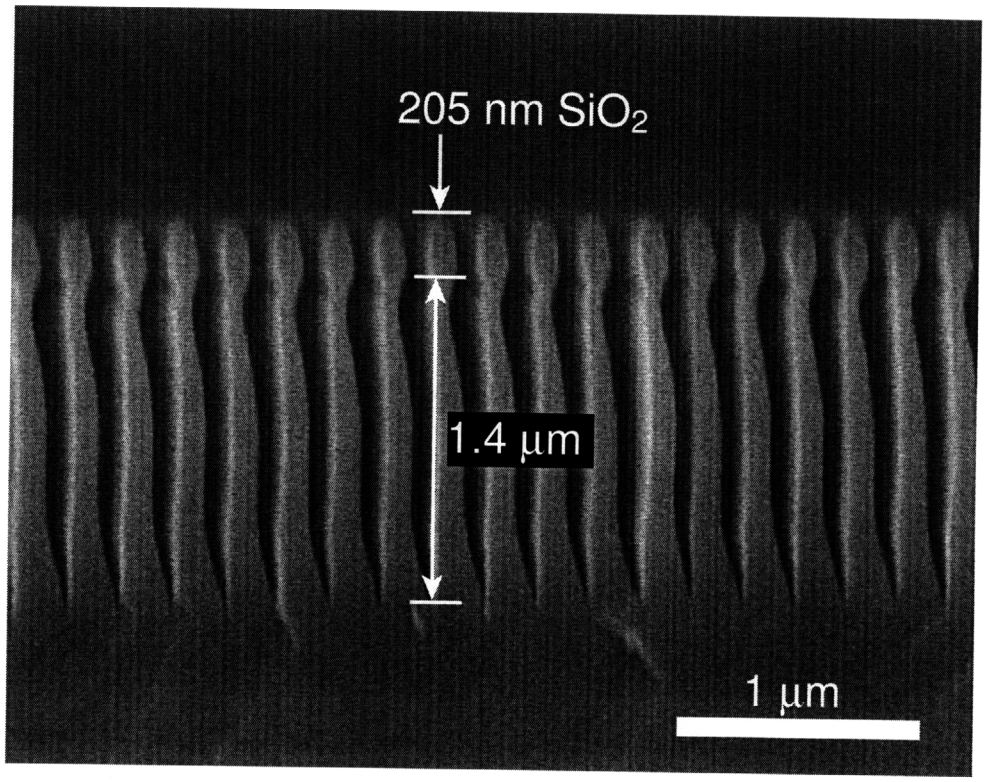


Figure 6-11: SEM micrographs of 200 nm-period gratings in silicon etched using HBr RIE for two hours with a bias voltage of 200 V and pressure of 2 mTorr.

solution at room temperature (21 °C). The KOH concentration was 50 wt% with 0.02 wt% of the surfactant SDSS. The KOH polishing results are shown in Fig. 6-12. The sidewall waviness seems to disappear relatively quickly (in 5 minutes) by KOH etching, while the sidewall slope slowly straightens from the top as etching time increases. However, the oxide mask was detached during 15 minutes of KOH etching due to significant undercutting. This low etch anisotropy might be ascribed to pattern misalignment because the grating pattern was not aligned with the true $\langle 111 \rangle$ using the wagon-wheel technique. With a better pattern alignment and longer KOH etching, the polishing step might be able to improve the sidewall slope close to 90°.

In this chapter, I presented a plasma etching process in conjunction with KOH polishing to reduce area loss of the CAT grating fabricated using only KOH anisotropic etching. Even though the process is not fully integrated with the previous fabrication process for the CAT grating, the HBr RIE+KOH polishing process is a feasible ap-

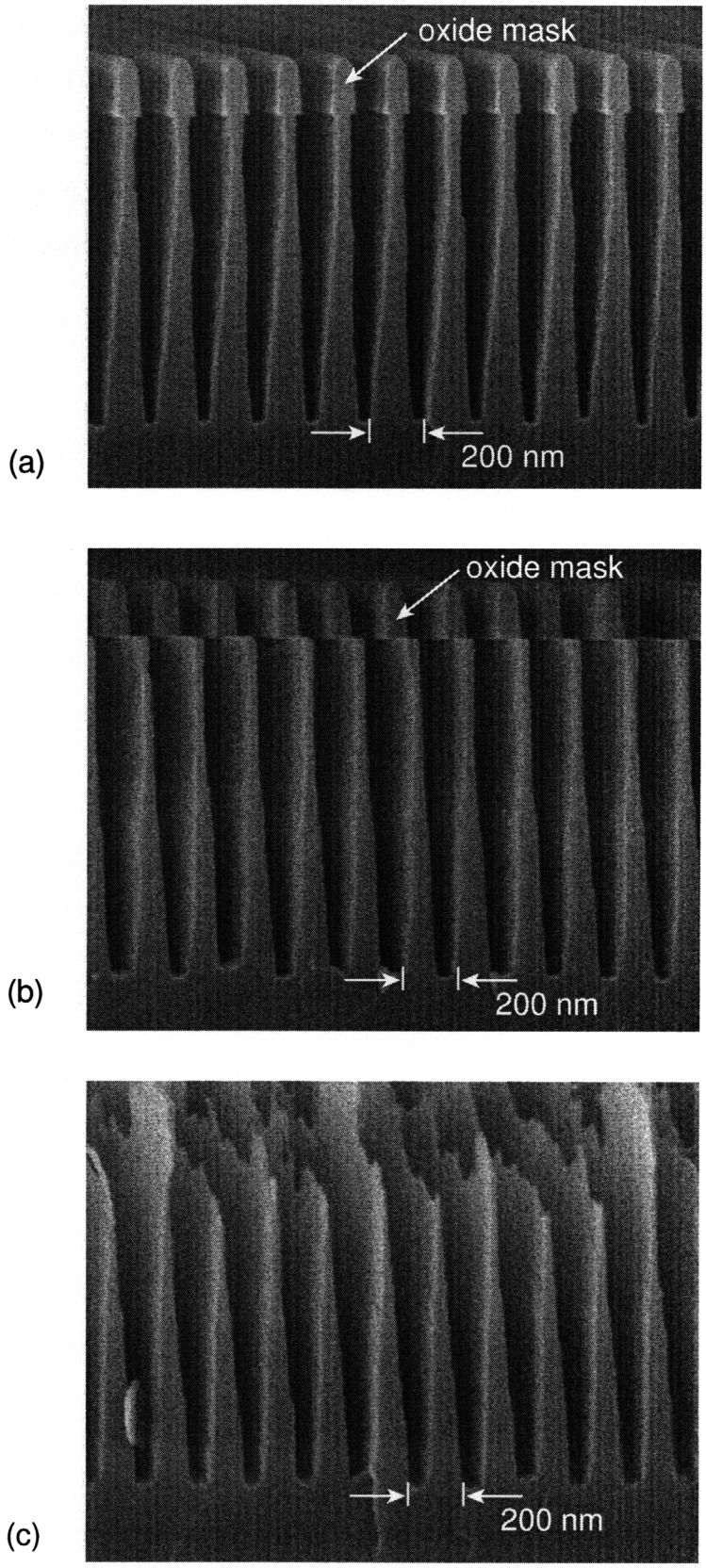


Figure 6-12: SEM micrographs of 200 nm-period gratings polished by KOH etching for (a) 5 min, (b) 10 min, and (c) 15 min. Note that the oxide mask in (b) is broken due to cleaving.

proach to produce high aspect-ratio silicon gratings with smooth sidewalls. If we use a high density plasma system like inductively coupled plasma (ICP) RIE, we might be able to completely etch the 6 $\mu$m device layer with a faster etch rate and then polish the grating with KOH. In that way, we could effectively engineer the support structure regardless of the geometrical constraints of KOH etching.

# Chapter 7

# X-ray Diffraction Tests

Based on the CAT grating idea, I successfully designed and fabricated the free-standing silicon gratings with an ultra-high aspect ratio as required. I was able to meet or exceed all design goals such as grating bars with the aspect ratio of 150 and smooth and straight grating sidewalls (measured RMS roughness $< 0.2$ nm and sidewall slope $< 0.2°$). In order to experimentally prove the CAT grating concept, we measured diffraction efficiency of the CAT gratings with EUV and x rays from a synchrotron facility of the Advance Light Source (ALS) at Lawrence Berkeley National Laboratory. The dimensions of the CAT gratings used for x-ray testing are summarized in Table 7.1. The x-ray test setup and results are described in detail in Refs. [2, 5]. Most of the results that will be reported in this chapter were obtained from the references.

Figure 7-1 shows the schematic of the measurement setup. The CAT gratings were mounted with an incident angle $\alpha$ from the grating normal. The angle $\alpha$ was found from the grating bar geometry

$$\alpha = \tan^{-1}\left(\frac{a}{d}\right), \tag{7.1}$$

where $d$ is the height of a grating bar and $a$ is the space between grating bars. Scanning the detector, we measured intensity of the diffracted beam from the 574 nm-period CAT grating at wavelengths ranging from 1.62 to 49 nm. The detector position or

Table 7.1: Dimensions of the CAT gratings used for x-ray diffraction testing.

| | | | |
|---|---|---|---|
| Grating period (nm) | | 574 | 200 |
| Grating thickness[a] ($\mu$m) | | 10 | 4 |
| Grating bar width (nm) | Top | 40 | 42 |
| | Bottom | 100 | 44 |
| Sidewall slope angle (deg) | | 0.17 | 0.07 |
| Support period ($\mu$m) | | 70 | 40 |
| Support opening ($\mu$m) | Top | 40 | 20 |
| | Bottom | 5 | 7 |
| Membrane area (mm$^2$) | | 10 | 9 |

[a] $\pm 0.5$ $\mu$m tolerance, given by the SOI manufacturer.

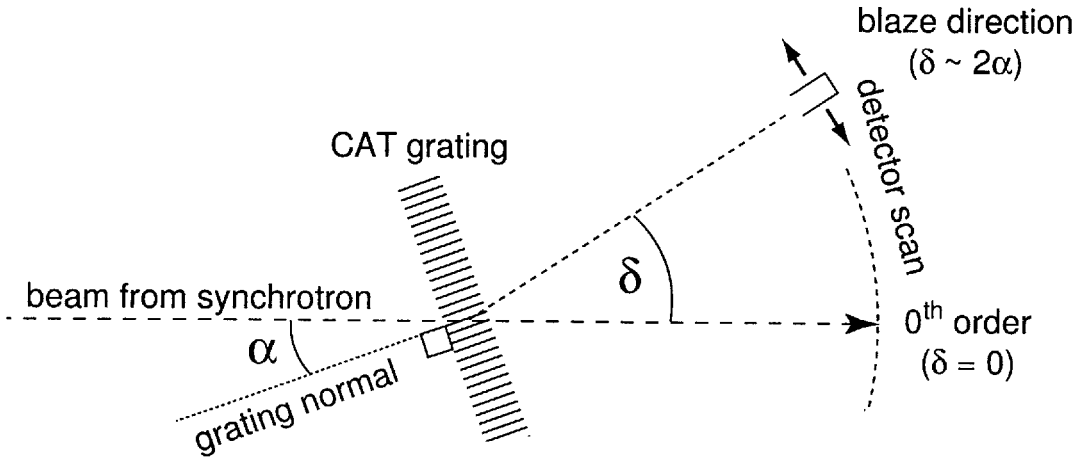


Figure 7-1: Schematic of x-ray diffraction measurement [2].

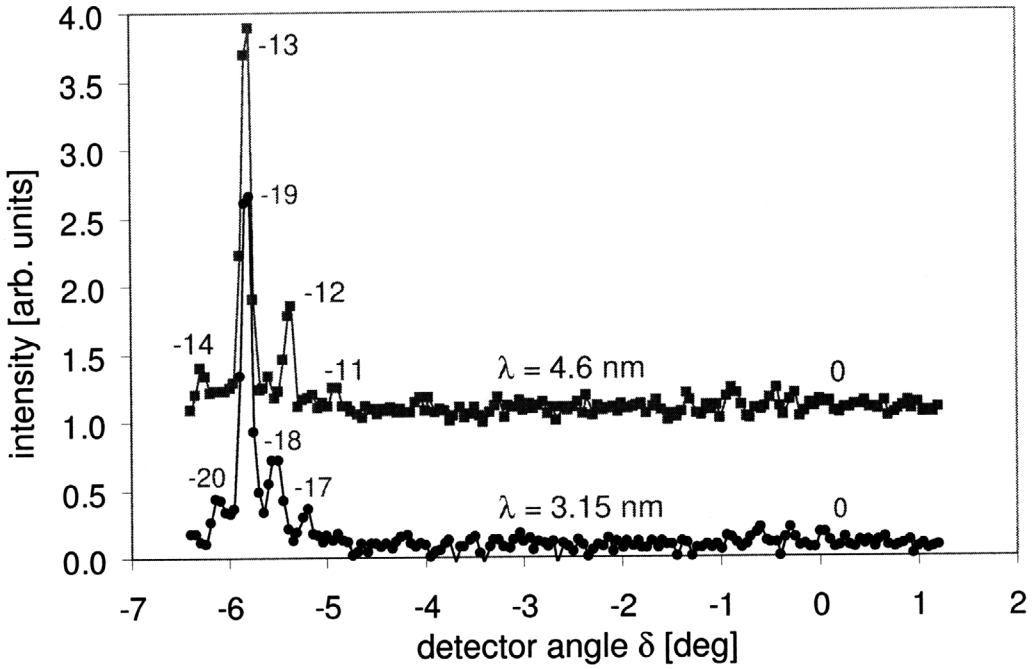


Figure 7-2: X-ray diffraction from a 574 nm-period CAT grating with synchrotron x rays with $\lambda$ =4.6 and 3.15 nm. The numbers in the plot denote the diffraction orders.

angle $\delta$ is read from the 0th transmitted order. Recalling the blaze condition described in Chapter 2, blazing is expected to occur when $\delta = 2\alpha$ assuming the grating bars are perfectly straight. The blazed order $m$ is determined by

$$|m| = \frac{2p}{\lambda} \sin \alpha, \tag{7.2}$$

where $\lambda$ is the wavelength and $p$ is the grating period. The sign of $m$ can vary depending on sign convention used. Figure 7-2 shows the measurement data of x-ray diffraction from the 574 nm-period CAT grating, where $\alpha = 2.9°$ and $\lambda = 4.6$ and 3.15 nm. A strong blazing effect is obvious around the expected angle $\delta = 2\alpha = 5.8°$, while suppressing the 0th transmitted order. Corresponding blazed orders are -13th for $\lambda = 4.6$ nm and -19th for $\lambda = 3.15$ nm. High diffraction efficiency at these high orders will increase the angular dispersion, which is one of the desired properties of a diffraction grating for x-ray spectroscopy.

The normalized efficiencies of a number of diffraction orders are plotted against

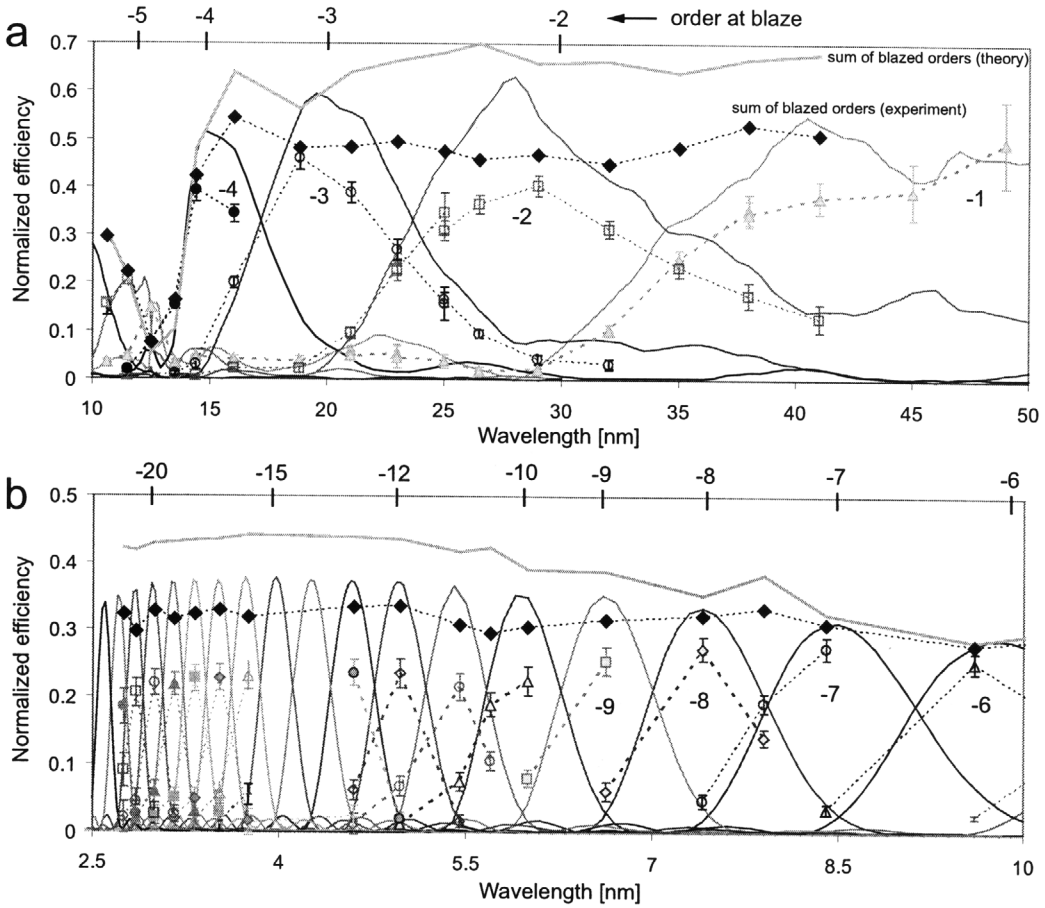


Figure 7-3: Normalized diffraction efficiency of a 574 nm-period CAT grating for (a) $\lambda$ = 10 - 50 nm and (b) $\lambda$ = 2.5 - 10 nm. The solid curves represent theoretical prediction by RCWA [43] and the dotted lines connect experimental data for each order [2].

wavelength in Fig. 7-3. The experimental data (dotted lines) agree well with theoretical predictions (solid curves) obtained by rigorous coupled wavelength analysis (RCWA) described in Chapter 2. Comparing experimental and theoretical sums of diffraction efficiencies at a fixed wavelength, we can see the data match with the theoretical prediction within 70 - 85 %. As the wavelength becomes shorter (higher photon energy), blazing occurs at higher orders, which we can also predict from Eqn. (7.2). For shorter wavelengths, the CAT grating will become more transparent (stronger 0th order) because the incident angle $\alpha = 2.9°$ is larger than the critical angle for total external reflection.

With the encouraging x-ray diffraction test results with 574 nm-period CAT grat-

ings, we fabricated 200 nm-period CAT gratings for x-ray tests with shorter wavelengths using the improved fabrication process described in Chapter 4. With the same measurement setup shown in Fig. 7-1 with $\alpha = 2.6°$, we measured diffraction efficiencies of the 200 nm-period CAT grating at wavelengths ranging from 1 to 20 nm. Figure 7-4 shows the normalized diffraction efficiencies of diffraction orders versus wavelength. We can see that diffraction efficiencies are in better agreement with the theoretical prediction than the 574 nm-period CAT grating case. This might be because the improved fabrication process for the 200 nm CAT gratings produced not only steeper sidewall slope but also fewer defects than the initial process for the 574 nm-period CAT grating prototypes.

In this chapter, I briefly summarized x-ray diffraction test results with the CAT gratings fabricated. The CAT gratings produced a strong blazing effect in the direction of specular reflection from the mirror-like grating sidewalls when the angle of incidence is equal to or smaller than the critical angle for total external reflection. The diffraction efficiencies measured with EUV and soft x rays agreed very well with predictions by the CAT grating model and RCWA simulation.

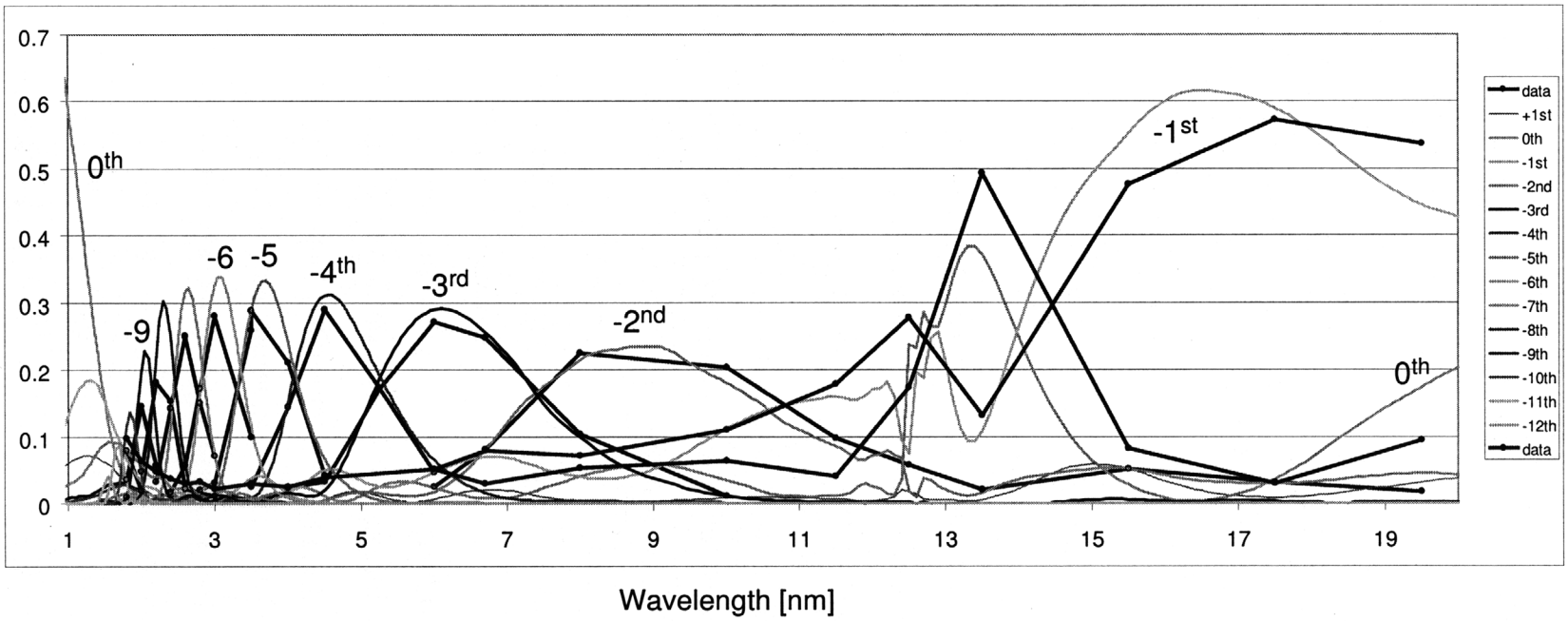


Figure 7-4: Normalized diffraction efficiency of a 200 nm-period CAT grating for $\lambda$ = 1 - 20 nm. The solid curves represent theoretical prediction by RCWA [43] and the solid lines with dots connect experimental data points for each order [98].

# Chapter 8

# Conclusion

The critical-angle transmission (CAT) grating is a new type of diffraction grating for soft x-ray* spectroscopy. The core idea of the CAT grating is to enhance diffraction efficiency of a transmission grating via reflection from the grating sidewalls. Unlike a conventional transmission grating which symmetrically spreads the diffracted orders with a central peak at zero$^{th}$ order, the CAT grating is designed to concentrate most of the diffraction energy into a particular non-zero order (blazed order) in the direction of specular reflection from the grating sidewalls. However, because of the shallow critical angle for soft x rays required to reflect from the grating sidewalls, the CAT grating requires mirror-like grating bars with an ultrahigh aspect ratio. This geometrical requirement imposes fabrication challenges. In this thesis, I covered introduction to the CAT grating concept and design, development of fabrication processes, and finally experimental proof of the concept through x-ray diffraction measurement with fabricated CAT gratings.

I have developed and demonstrated a bulk micromachining process for the fabrication of ultrahigh aspect ratio free-standing gratings with 574 nm period on silicon-on-insulator (SOI) wafers (Chapter 3). An aspect ratio of 150 was achieved by using high concentration potassium hydroxide (KOH) etching at a relatively low temperature, followed by supercritical drying. Free-standing grating bars are 10 $\mu$m tall, $\sim$40 nm wide at the top, and $\sim$100 nm wide at the bottom with 0.15° sidewall slope. The

*$\sim$ 1 to 10 nm in wavelength

sidewall roughnesses (root mean square) of test samples is less than 0.2 nm and 1 nm over 65 $\times$ 65 $nm^2$ area and 10 $\times$ 10 $\mu m^2$ area, respectively, which were measured by an atomic force microscope. This CAT grating prototype was tested with soft x rays to demonstrate the blazing effect and to determine its diffraction efficiency. Diffraction tests with low energy x rays (<0.5 keV) showed high-efficiency blazing as predicted by theory.

In order to fabricate CAT gratings with a finer period for higher energy x-ray applications, I adapted the process previously developed for the prototype grating to fabricate 200 nm-period CAT gratings with 40 nm linewidth (Chapter 4). An etching process having higher etch anisotropy is essential to realize the high aspect-ratio grating bars with finer period. The etch anisotropy of KOH etching was significantly improved by a precise grating pattern alignment with {111} silicon planes using the wagon-wheel technique. I also confirmed that a high etch anisotropy could be obtained in a highly concentrated KOH solution at a low etching temperature. However, I found there was a rapid initial undercutting during KOH etching, which impaired overall etch anisotropy. Taking into account the initial undercut amount, the slow ⟨111⟩ etch rate (<5 nm/hr) at room temperature (21°C) enabled us to control the linewidth by time. An image-reversal process solved a process latitude problem due to the narrow nitride lines formed by interference lithography and subsequent pattern transfer using RIE. In order to ameliorate etch uniformity, I tested a surfactant and ultrasonic agitation to promote hydrogen bubble detachment during KOH etching.

The last major fabrication challenge is solving a grating bar attachment problem which is not related to surface tension during the drying step. Using an analytical model, finite element analysis (FEA), and experimental proof, I revealed the stiction problem occurred during wet HF release of the CAT gratings (Chapter 5). I concluded the stiction problem originated from grating plane buckling due to compressive stress in the buried oxide layer in the SOI substrates. Based on FEA simulation, I redesigned the oxide thickness and support mesh that would not produce the stress-induced stiction problem. With the design modification, I was able to successfully fabricate 200 nm-period CAT gratings in 4 - 6 $\mu m$ thick device layers without stiction. The

line widths of a single grating bar are 35 nm at the top and 45 nm at the bottom. The aspect ratio of the grating bar is about 100 with a sidewall slope angle of 0.07°, which implies a very high etch anisotropy. To the best of my knowledge, the sidewall slope in this scale is the steepest reported angle that has been achieved by any etching technique.

The support structure needs to be engineered to reduce loss of the grating area while effectively buttressing the membrane and free-standing gratings. However, the KOH etching process has geometrical constraints in fabricating arbitrary structures because of its dependence on crystallographic orientations. In Chapter 6, I demonstrated that reactive ion etching with subsequent KOH polishing is one of several feasible techniques to engineer the support structure without geometrical limitations.

Lastly, I summarized x-ray diffraction testing with 574 and 200 nm-period CAT gratings (Chapter 7). We observed the strong blazing effect in the direction of specular reflection from the grating sidewalls, as expected. The measured and normalized diffraction efficiency was consistent with the theoretical prediction within 70 - 85%. These experimental results prove not only the CAT grating concept, but also practicality of the fabrication process.

# Appendix A

# Recipe for the 200 nm-period CAT gratings

The fabrication process for 200 nm-period CAT gratings is described with key parameters. The substrates are ⟨110⟩ SOI wafers with a 6 $\mu$m-thick device layer*, 150 nm of buried oxide, and 500 $\mu$m-thick handle layer. The wafers have two flats at the ⟨111⟩ directions with a $\pm 0.2°$ tolerance.

**Front-side patterning**

1. In ICL, deposit 35 nm of LPCVD silicon nitride using *VTR*.
   - Silicon rich nitride using the "10 : 1 recipe" (Dichlorosilane : Amonia = 10 : 1).
2. In TRL, deposit 30 nm of chromium using the ebeam evaporator *EbeamAu*.
   - With a piece of aluminium foil, cover $2 \times 1$ cm$^2$ area for the wagon-wheel pattern at the major flat.
3. In TRL, pattern the support mesh and wagon wheel using contact lithography.
   - Vapor HMDS.
   - Spin-coat 1 $\mu$m of OCG 825-34cs ($\sim$3 krpm).

*The device layer thickness can vary within $\pm 0.5$ $\mu$m

- Oven-Bake at 95 °C for 30 min.
- Expose for 2 sec (20 mJ/cm$^2$) using the aligner *EV1* with the mask "CAT front_rev5".
- Develop for 1 min in a TMAH developer OCG 934 1:1.
- Rinse with DI water for 1 min and dry with a nitrogen gun.

4. In TRL, wet etch Cr in CR-7.
   - Etch rate = ~2 nm/sec.
   - Rinse with DI water and dry.
5. In TRL, etch the wagon-wheel pattern using the *PlasmaQuest*
   - Cover the support mesh area with a piece of silicon wafer.
   - $CF_4 : O_2$ = 40 sccm: 4 sccm.
   - Pressure = 7 mTorr.
   - RF power = 20 W and ECR power = 100 W.
   - Etch rate = ~32 nm/min.
6. In SNL, remove the photoresist using an RCA clean.
   - $H_2O : NH_4OH : H_2O_2 = 5 : 1 : 1$.
   - Temperature = 75 °C.
   - Time = 10 min.
   - Rinse with DI water and dry.
7. In SNL, KOH pre-etch for the wagon-wheel pattern.
   - Dip in BHF for 15 sec and rinse with DI water.
   - KOH concentration = 25 %.
   - Temperature = 80 °C.

- Time = 30 min.
- Rinse with DI water and dry carefully not to damage the etched wagon-wheel pattern.

8. In NSL, inspect the wagon-wheel pattern using top-view SEM to find the minimum undercut direction.
9. In SNL, RCA clean the wafer before patterning the 200 nm-period grating.
10. In NSL, spin-coat ARC (XHRiC-11, Brewer Science)
    - Thickness = 102 nm (4.2 krpm).
    - Bake on a hot plate at 175 °C for 1 min.
11. In NSL, spin-coat photoresist (PFI-88a2, Sumitomo Corp.)
    - Thickness = 200 nm (3.5 krpm).
    - Bake on a hot plate at 90 °C for 1.5 min.
12. In SNL, pattern 200 nm-period grating with the Nanoruler.
    - Using the microscope mounted on the Nanoruler, align the grating direction with the true {111} plane determined in step 8.
    - Dose = 45 mJ/cm$^2$.
    - Develop in OPD 262 for 1 min.
    - Rinse with DI water and spin-dry
13. In NSL, etch ARC using RIE.
    - $O_2$ 20 sccm, pressure = 7 mTorr, power = 80 W.
    - Etch rate = ~65 nm/min.
14. In NSL, remove the photoresist on top of ARC using NMP.
    - Room temperature (21 °C).

- Time = 1 min.
- Rinse with DI water and spin-dry.

15. In NSL, spin-coat Silspin (Molecular Imprint).
    - Thickness = 200 nm (2.0 krpm).
    - Hot plate bake at 150 °C for 1 min.
16. In NSL, etch-back the Silspin layer using RIE.
    - $CF_4$ 18 sccm, pressure = 10 mTorr, power = 150 W.
    - Etch time = ~4.5 min.
17. In NSL, etch the ARC lines between the Silspin using RIE.
    - $O_2$ 20 sccm, pressure = 7 mTorr, power = 80 W.
    - Etch time = ~1.4 min.
18. In NSL, transfer the Silspin pattern into nitride using RIE.
    - $CF_4$ 18 sccm, pressure = 10 mTorr, power = 150 W.
    - Etch rate = ~25 nm/min.
19. In SNL, Piranha clean to remove the Silspin.
    - Add one part of $H_2O_2$ slowly to three parts of $H_2SO_4$.
    - Immerse the wafer carefully because the piranha solution is very hot by itself (exothermic reaction).
    - Time = 10 min.
20. In SNL, RCA clean to remove residual polymer.
    - $H_2O : NH_4OH : H_2O_2 = 5 : 1 : 1$.
    - Temperature = 75 °C.
    - Time = 10 min.
    - Rinse with DI water and dry.

### Backside patterning and TMAH etching

21. In TRL, pattern the backside using contact lithography.

    - Vapor HMDS.
    - Spin-coat 1 $\mu$m of OCG 825-34cs (~3 krpm) on both sides[†] of the wafer.
    - Oven-Bake at 95 °C for 30 min.
    - Expose on the backside for 2 sec (20 mJ/cm$^2$) using the aligner *EV1* with the mask "CAT back_rev5".
    - Develop for 1 min in a TMAH developer OCG 934 1:1.
    - Rinse with DI water for 1 min and dry with a nitrogen gun.

22. In TRL, transfer the backside pattern into nitride using the *PlasmaQuest*

    - $CF_4 : O_2$ = 40 sccm: 4 sccm.
    - Pressure = 7 mTorr.
    - RF power = 20 W and ECR power = 100 W.
    - Etch rate = ~32 nm/min.

23. In SNL, RCA clean to remove photoresist.

    - $H_2O : NH_4OH : H_2O_2 = 5 : 1 : 1$.
    - Temperature = 75 °C.
    - Time = 10 min.
    - Rinse with DI water and dry.

24. In NSL, spin-coat ProTEK B3 primer (Brewer Science).

    - Speed = 1.5 krpm for 1 min (2 - 3 nm).
    - Bake on a hot plate at 205 °C for 1 min.

[†]Front-side coating is for temporary protection of the grating pattern during backside processing.

25. In NSL, spin-coat ProTEK B3 (Brewer Science).

    - Speed = 5 krpm for 1 min (~3.5 $\mu$m).
    - Bake on hot plates at 140 °C for 2 min and then at 205 °C for 1 min.

26. In SNL, etch the backside handle layer using TMAH (Sigma-Aldrich).

    - Dip in BHF for 15 sec and rinse with DI water.
    - TMAH concentration = 25%.
    - Temperature = 90 °C.
    - Etch time = ~5.5 hr (until shiny oxide surfaces appear).
    - Rinse with DI water and dry carefully not to break the membrane.

27. In SNL, remove ProTEK B3 using solvents.

    - 40 min in Methyl Isoamyl Ketone (MIAK) and 15 min in isopropanol (IPA).
    - Rinse with DI water and dry.

28. In NSL, remove ProTEK B3 primer using $O_2$ plasma etching.

    - 3 min in the *asher* with 200 W.

**KOH etching and HF releasing**

Note that the grating sample is always immersed in liquid during the following wet processes to avoid any air exposure until supercritical drying.

29. In SNL, etch through the device layer using KOH.

    - Take off one grating device out of the wafer and insert in a teflon etch holder.
    - Using a plastic pipette, drop BHF on the backside of the device membrane to thin the oxide layer to less than 100 nm (1 min is enough).

- Dip in BHF for 15 sec and rinse with DI water.
- Immerse the grating sample horizontally in 50 wt% KOH solution with 0.02 wt% of the surfactant SDSS.
- Temperature = 21 °C.
- Etch rates: $R_{\langle 110 \rangle}$=1.4 $\mu$m/hr and $R_{\langle 111 \rangle}$=5 nm/hr.
- Optionally, try ultrasonic agitation with 20 - 30 W. With 20 W of ultrasonic agitation, 5 hours was enough to achieve a linewidth of 40 nm.
- Rinse with hot (~90 °C) DI water.

30. In SNL, etch buried oxide and nitride mask using concentrated hydrofluoric acid.
    - HF concentration = 49%.
    - Etch time = 5 min.
    - Rinse with DI water.

**Supercritical drying**

31. In SNL, dehydrate the sample with ethanol.
    - Gradually increase ethanol concentration from 50 to 100%.
    - Quickly transfer the sample from one beaker to another or use a special holder to prevent exposure to air.
    - Keep the sample in a 100% ethanol jar and bring to NSL.
32. In NSL, dry the sample using a critical point dryer (Autosamdri-815B, Tousimis) with liquid carbon dioxide ($LCO_2$).
    - Critical point of $CO_2$ = 1070 psi at 31 °C.
    - One-hour automatic drying process :

Fill the chamber with $LCO_2$ → Purge ethanol with flowing $LCO_2$ → Increase pressure and temperature → Slowly decrease pressure keeping the temperature above 31 °C → Vent.

# Appendix B

# Estimation of Resonance Frequencies and Shock Resistivity of the CAT grating

## B.1 Natural Frequencies of a Rectangular Plate

Space instrumentation requires a robust structural design which can survive harsh launch environment including high levels of vibration. Launching vibration may cause damage to the spacecraft and instruments when the vibration frequencies happen to match with their natural (resonant) frequencies. Mongrard [14] suggested the minimum natural frequency should be higher than 1 kHz based on launching vibration power spectrum data of the Pegasus launch vehicle [99]. In this chapter, I will estimate resonance frequencies of a single grating plane which is assumed to be a rectangular plate with two edges clamped. Figure B-1 illustrates the double-clamped rectangular plate to be analyzed. For a convenient calculation, I assume that the displacement in the $z$ direction is a function of $x$ and time $t$ or $z(x,t)$, which means deflection only along the $y$ axis is considered.

Neglecting internal mechanical damping, the equation of motion is given by

$$\frac{\partial^2 z}{\partial t^2} + c_q^2 \frac{\partial^4 z}{\partial x^4} = 0, \tag{B.1}$$

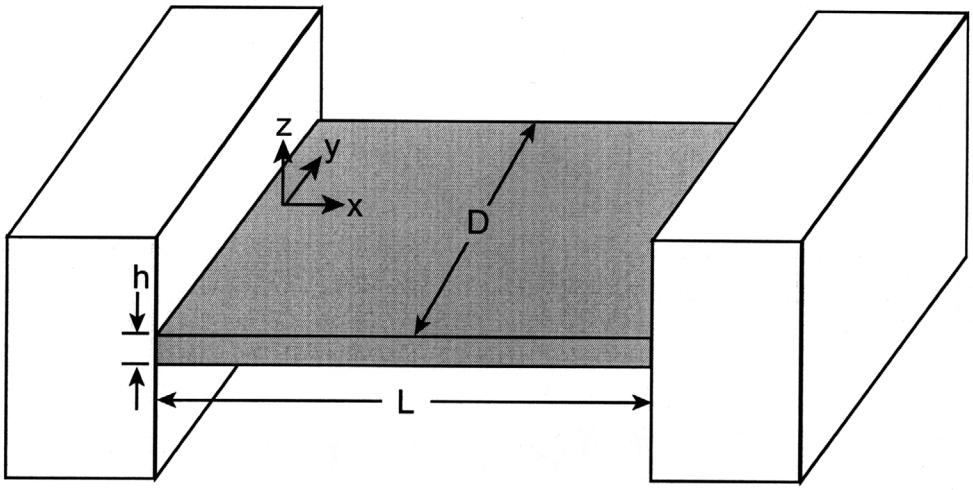


Figure B-1: Double-clamped rectangular plate.

where $c_q^2$ is defined as

$$c_q^2 \equiv \frac{Eh^2}{12\rho(1-\nu^2)}, \tag{B.2}$$

where $E$ is Young's modulus of the plate, $\nu$ is the Poisson's ratio, $\rho$ is the density, and $h$ is the thickness of the plate [100]. For the double-clamped plate, the boundary conditions are

$$\left.\begin{array}{l} z = 0 \\ \frac{\partial z}{\partial x} = 0 \end{array}\right\} \text{ at } x = 0 \text{ and } L. \tag{B.3}$$

Assuming $z(x,t)$ is separable, that is, $z(x,t) = T(t)X(x)$, the partial differential equation (PDE) Eqn. (B.1) is simplified to two ordinary differential equations (ODEs)

$$\frac{d^2T}{dt^2} + w^2T = 0 \text{ and} \tag{B.4}$$

$$\frac{d^4X}{dx^4} - \frac{w^2}{c_q^2}X = 0, \tag{B.5}$$

where $w$ is a real number. When $w \neq 0$, the general solutions for these ODEs are

$$T(t) = a\cos wt + b\sin wt, \tag{B.6}$$

$$X(x) = c\cos\beta x + d\sin\beta x + e\cosh\beta x + f\sinh\beta x, \tag{B.7}$$

where $\beta = \sqrt{w/c_q}$. Using the boundary conditions Eqn. (B.3), we obtain

$$\begin{aligned} c + e &= 0, && \text{(B.8)} \\ d\beta + f\beta &= 0, && \text{(B.9)} \\ c\cos\beta L + d\sin\beta L + e\cosh\beta L + f\sinh\beta L &= 0, && \text{(B.10)} \\ -c\beta\sin\beta L + d\beta\cos\beta L + e\beta\sinh\beta L + f\beta\cosh\beta L &= 0, && \text{(B.11)} \end{aligned}$$

which can be expressed in a matrix form

$$\begin{bmatrix} (\cos\beta L - \cosh\beta L) & (\sin\beta L - \sinh\beta L) \\ -(\sin\beta L + \sinh\beta L) & (\cos\beta L - \cosh\beta L) \end{bmatrix} \begin{Bmatrix} c \\ d \end{Bmatrix} = 0. \qquad \text{(B.12)}$$

In order for non-zero $c$ and $d$ to exist, the determinant of the coefficient matrix in Eqn. B.12 must be zero. Using trigonometric identities with this condition, we obtain

$$\cos\beta L \cosh\beta L = 1. \qquad \text{(B.13)}$$

Equation B.13 has an infinite number of solutions for $\beta$. Arranging these solutions in ascending order of their magnitudes, we define the natural frequencies $w_n = c_q\beta_n^2$, where $n = 1, 2, 3, \cdots$. The eigenfunction $X_n(x)$ corresponding to the $n^{th}$ natural frequency $w_n$ is given by

$$X_n(x) = c_n(\cos\beta_n x - \cosh\beta_n x) + d_n(\sin\beta_n x - \sinh\beta_n x), \qquad \text{(B.14)}$$

where the coefficient ratio $c_n/d_n$ is

$$\frac{c_n}{d_n} = \frac{\cos\beta_n L - \cosh\beta_n L}{\sin\beta_n L + \sinh\beta_n L}. \qquad \text{(B.15)}$$

Let us consider the lowest natural frequency ($n = 1$). From Eqn. (B.13), $\beta_1 L = 4.73$*.

*For several lowest modes, $\beta_1 L = 4.730$, $\beta_2 L = 7.853$, and $\beta_3 L = 10.996$ [100].

Therefore, the first natural frequency in Hertz is

$$f_1 = \frac{w_1}{2\pi} = \frac{c_q}{2\pi}\frac{4.73^2}{L^2} = 3.56\frac{h}{L^2}\sqrt{\frac{E}{12\rho(1-\nu^2)}}. \quad \text{(B.16)}$$

For example, assuming a single CAT grating plane[†] is a rectangular plate with $L = 25$ $\mu$m, $h = 40$ nm, we estimate the first natural frequency $f_1 = 585$ kHz, which is orders of magnitude higher than the required minimum natural frequency 1 kHz. Therefore, I conclude the CAT grating bars can survive the launching vibration.

However, we need to consider vibration of the membrane itself holding the gratings. Assuming that the membrane is a square ($L \times L$) flat plate of silicon without gratings, the first natural frequency of a square plate with all edges clamped square plate is given by

$$f_1 = \frac{36.0}{2\pi}\sqrt{\frac{E}{12\rho(1-\nu^2)}}\frac{h}{L^2}, \quad \text{(B.17)}$$

where $h$ is the plate thickness [86]. Rearranging this equation with respect to $L$, we can find the maximum length $L$ which yields the first natural frequency higher than 1 kHz. Therefore,

$$\frac{36.0}{2\pi}\sqrt{\frac{E}{12\rho(1-\nu^2)}}\frac{h}{1000} > L^2, \quad \text{(B.18)}$$

where $h = 6$ $\mu$m is used, and we obtain $L < 9.4$ mm. However, a practical value for the length $L$ should be less than 9.4 mm because the membrane with the grating would have lower stiffness unless there are additional reinforcing structures.

In this section, I estimated the natural frequencies of a single grating plane and the membrane holding the grating as well. While the grating plane has significantly higher natural frequencies than 1 kHz, the membrane would require additional support structures to hold grating areas larger than 1 cm$^2$ without a resonance problem.

[†]Assume silicon has isotropic material properties, $E = 170$ GPa , $\nu = 0.28$, and $\rho = 2330$ kg/m$^3$.

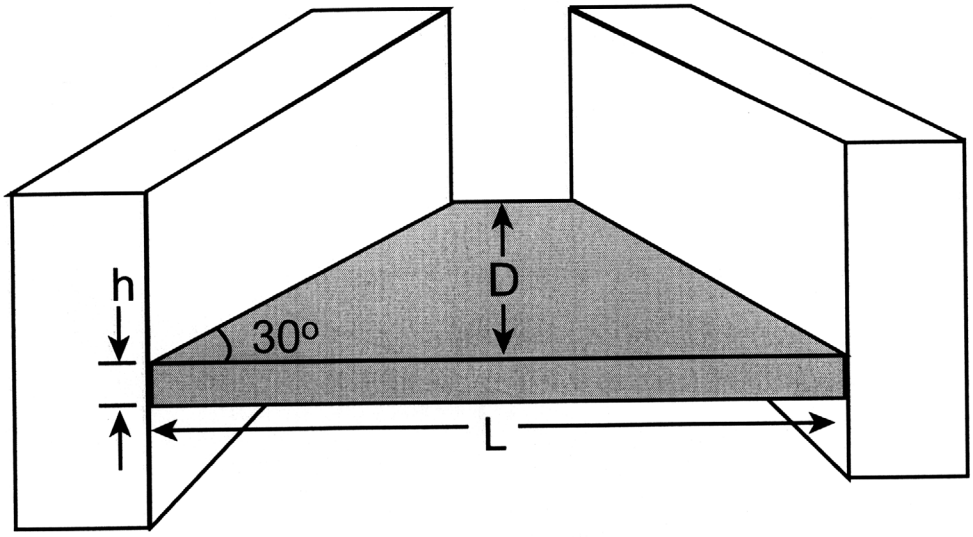


Figure B-2: Double-clamped trapezoidal plate.

## B.2 Finite Element Analysis for Natural Frequencies of a Trapezoidal Plate

For more accurate modeling closer to reality, I used a FEM software, *COMSOL* [87], with the actual trapezoidal grating plane fabricated by KOH etching. The model used is illustrated in Fig. B-2, where $L$ is the top length, $h$ is the plate thickness, and $D$ is the plate depth. Let us consider an example based on the previous fabrication results. For the 4 $\mu$m-thick CAT grating shown in Fig.4-23 in Chapter 4, we assign $L = 20$ $\mu$m, $h = 40$ nm, and $D = 4$ $\mu$m. First three natural frequencies and their mode shapes are shown in Fig. B-3. Obviously, the trapezoidal plate has even higher natural frequencies than a rectangular plate with the same top length $L$, because the length between the fixed edge in the trapezoidal case decreases linearly with depth and the natural frequency is inversely proportional to the square of length.

This finite element analysis with an actual CAT grating confirms that the fabricated CAT gratings have high natural frequencies not causing a low frequency resonance problem in the launching environment.

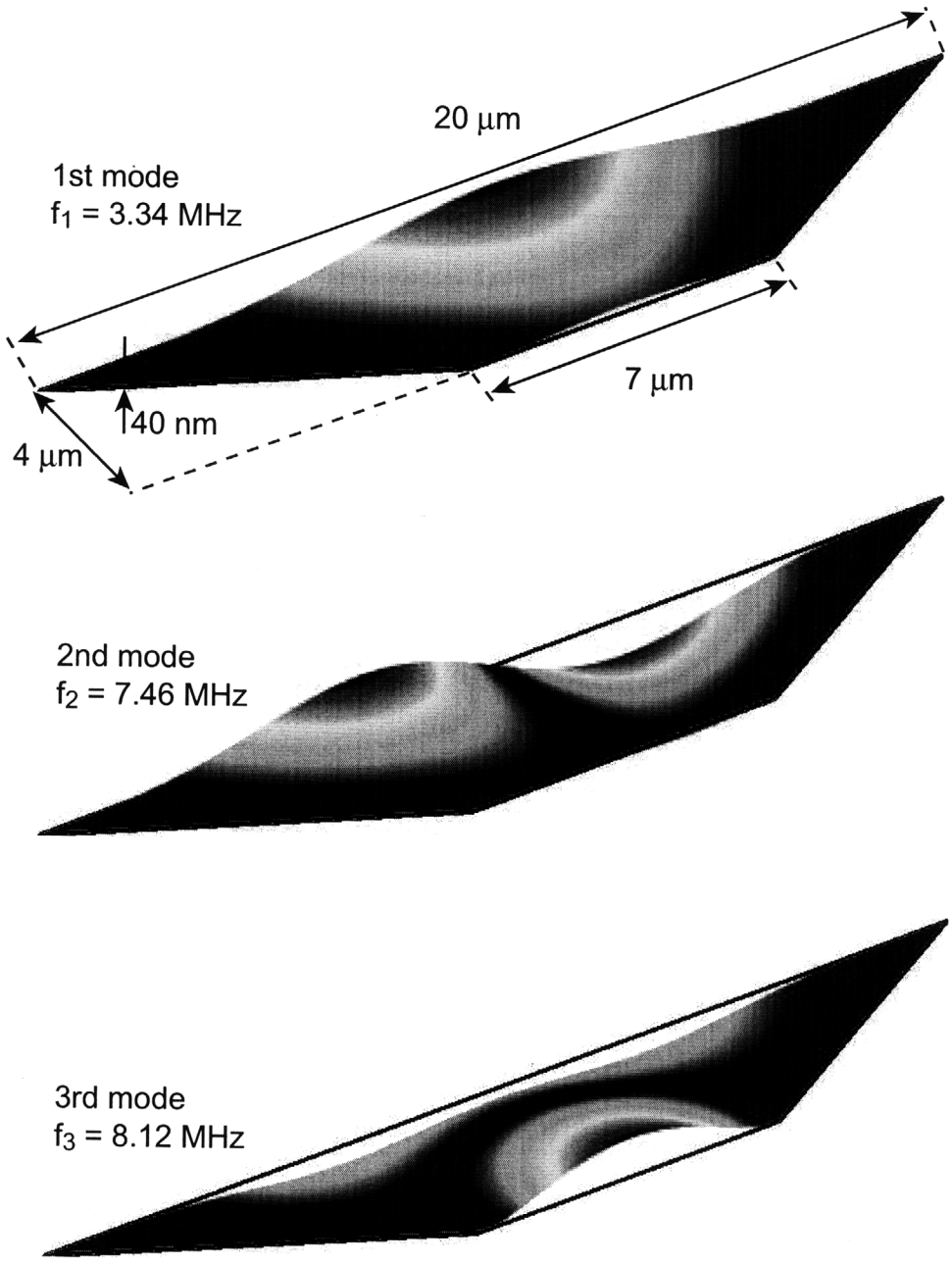


Figure B-3: Several resonant modes and their frequencies of a trapezoidal plate.

## B.3 Shock Resistivity

The launch environment also entails mechanical shocks or abrupt acceleration surges in a few milliseconds [101]. Therefore, when designing space instruments, their shock resistivity should be considered. For example, the *Ariane 5*[‡] rocket system of ESA has a design requirement to survive $10^4$g, where g = 9.8 m/s$^2$ [101]. In this section, I will perform rough estimation of shock resistivity of a rectangular silicon grating plane with two opposite edges clamped [Fig. B-1]. To further simplify the calculation, I assume the plate to be a double-clamped beam. The inertial force due to acceleration $a$ is given by

$$F = \rho LDha, \tag{B.19}$$

where $\rho$ is density of silicon. Assuming this force applied at $x = L/2$, the maximum bending stress $\sigma_{max}$ is

$$\begin{aligned} \sigma_{max} &= \frac{M_{max}(h/2)}{I} \\ &= \frac{(FL/8)(h/2)}{Dh^3/12} \\ &= \frac{3}{4}\frac{L^2}{h}\rho a, \end{aligned} \tag{B.20}$$

where $M_{max}$ is the maximum bending moment and $I$ is the moment of inertia [86]. Therefore, the maximum sustainable acceleration $a_{max}$ is

$$a_{max} = \frac{4}{3}\frac{h}{L^2}\frac{\sigma_f}{\rho}, \tag{B.21}$$

where $\sigma_f$ is the fracture stress of silicon and typically $\sigma_f \sim 4$ GPa [50]. For example, when $L = 25$ $\mu$m, $h = 40$ nm, and $\rho = 2330$ kg/m$^3$, the maximum acceleration or shock resistivity $a_{max} \simeq 1.5 \times 10^7$g. From this estimation, we confirm the silicon CAT grating has a very high shock resistivity which comes from great mechanical properties of silicon. This is also one of the main reasons why silicon has been chosen for a popular MEMS material.

[‡]Ariane 5 was used to launch the XMM-Newton payload with a reflection grating spectrometer.

# Bibliography

[1] Christopher Palmer. *Diffraction Grating Handbook.* Thermo RGL, 5th edition, 2002.

[2] Ralf K. Heilmann, Minseung Ahn, Eric M. Gullikson, and Mark L. Schattenburg. Blazed high-efficiency x-ray diffraction via transmission through arrays of nanometer-scale mirrors. *Opt. Express*, 16(12):8658–8669, 2008.

[3] Joseph W. Goodman. *Introduction to Fourier Optics.* McGraw-Hill Company, 2nd edition, 1996.

[4] Mark L. Schattenburg, Claude R. Canizares, Daniel Dewey, Kathryn A. Flanagan, Margaret A. Hamnett, Alan M. Levine, Kenneth S. K. Lum, Ramanujam Manikkalingam, Thomas H. Markert, and Henry I. Smith. Transmission grating spectroscopy and the advanced x-ray astrophysics facility. *Optical Engineering*, 30(10):1590–1600, 1991.

[5] Ralf K. Heilmann, Minseung Ahn, and Mark L. Schattenburg. Fabrication and performance of blazed transmission gratings for x-ray astronomy. volume 7011, page 701106. SPIE, 2008.

[6] Leonid I. Goray. Rigorous efficiency calculations for blazed gratings working in in- and off-plane mountings in the 5-50-[angstrom] wavelengths range. volume 5168, pages 260–270. SPIE, 2004.

[7] Andrew P. Rasmussen, Andrew Aquila, Jay Bookbinder, Chih-Hao Chang, Eric M. Gullikson, Ralf K. Heilmann, Steven M. Kahn, Frits Paerels, and

Mark L. Schattenburg. Grating arrays for high-throughput soft x-ray spectrometers. volume 5168, pages 248–259. SPIE, 2004.

[8] Ralf K. Heilmann, Mireille Akilian, Chih-Hao Chang, Carl G. Chen, Craig R. Forest, Chulmin Joo, Paul T. Konkola, Juan C. Montoya, Yanxia Sun, Jenny You, and Mark L. Schattenburg. Advances in reflection grating technology for constellation-x. volume 5168, pages 271–282. SPIE, 2004.

[9] Randall L. McEntaffer, Steve N. Osterman, Webster C. Cash, John Gilchrist, Jean Flamand, Bruno Touzet, Fransis Bonnemason, and Christian Brach. X-ray performance of gratings in the extreme off-plane mount. volume 5168, pages 492–498. SPIE, 2004.

[10] Chih-Hao Chang, J. C. Montoya, M. Akilian, A. Lapsa, R. K. Heilmann, M. L. Schattenburg, M. Li, K. A. Flanagan, A. P. Rasmussen, J. F. Seely, J. M. Laming, B. Kjornrattanawanich, and L. I. Goray. High fidelity blazed grating replication using nanoimprint lithography. *Journal of Vacuum Science and Technology B: Microelectronics and Nanometer Structures*, 22(6):3260–3264, 2004.

[11] J. F. Seely, L. I. Goray, Benjawan Kjornrattanawanich, J. M. Laming, G. E. Holland, K. A. Flanagan, R. K. Heilmann, C.-H. Chang, M. L. Schattenburg, and A. P. Rasmussen. Efficiency of a grazing-incidence off-plane grating in the soft-x-ray region. *Appl. Opt.*, 45(8):1680–1687, 2006.

[12] Kathryn Flanagan, Minseung Ahn, John Davis, Ralf Heilmann, David Huenemoerder, Alan Levine, Herman Marshall, Gregory Prigozhin, Andrew Rasmussen, George Ricker, Mark Schattenburg, Norbert Schulz, and Yong Zhao. Spectrometer concept and design for x-ray astronomy using a blazed transmission grating. volume 6688, page 66880Y. SPIE, 2007.

[13] M. W. Hutley. *Diffraction Gratings.* Academic Press, 1st edition, 1982.

[14] Olivier Mongrard. High-accuracy foil optics for x-ray astronomy. Master's thesis, Massachusetts Institute of Technology, Cambridge, Massachusetts, September 2001.

[15] Mark L. Schattenburg. From nanometers to gigaparsecs: The role of nanostructures in unraveling the mysteries of the cosmos. *Journal of Vacuum Science and Technology B: Microelectronics and Nanometer Structures*, 19(6):2319–2328, 2001.

[16] R. Giacconi, G. Branduardi, U. Briel, A. Epstein, D. Fabricant, E. Feigelson, W. Forman, P. Gorenstein, J. Grindlay, H. Gursky, F. R. Harnden, J. P. Henry, C. Jones, E. Kellogg, D. Koch, S. Murray, E. Schreier, F. Seward, H. Tananbaum, K. Topka, L. Van Speybroeck, S. S. Holt, R. H. Becker, E. A. Boldt, P. J. Serlemitsos, G. Clark, C. Canizares, T. Markert, R. Novick, D. Helfand, and K. Long. The Einstein /HEAO 2/ X-ray Observatory. *The Astrophysical Journal*, 230:540–550, June 1979.

[17] J. W. den Herder, A. C. Brinkman, S. M. Kahn, G. Branduardi-Raymont, K. Thomsen, H. Aarts, M. Audard, J. V. Bixler, A. J. den Boggende, J. Cottam, T. Decker, L. Dubbeldam, C. Erd, H. Goulooze, M. Güdel, P. Guttridge, C. J. Hailey, K. A. Janabi, J. S. Kaastra, P. A. J. de Korte, B. J. van Leeuwen, C. Mauche, A. J. McCalden, R. Mewe, A. Naber, F. B. Paerels, J. R. Peterson, A. P. Rasmussen, K. Rees, I. Sakelliou, M. Sako, J. Spodek, M. Stern, T. Tamura, J. Tandy, C. P. de Vries, S. Welch, and A. Zehnder. The Reflection Grating Spectrometer on board XMM-Newton. *Astronomy and Astrophysics*, 365:L7–L17, January 2001.

[18] Martin C. Weisskopf. Five years of operation of the chandra x-ray observatory. volume 5488, pages 25–39. SPIE, 2004.

[19] C. R. Canizares, J. E. Davis, D. Dewey, K. A. Flanagan, E. B. Galton, D. P. Huenemoerder, K. Ishibashi, T. H. Markert, H. L. Marshall, M. McGuirk, M. L. Schattenburg, N. S. Schulz, H. I. Smith, and M. Wise. The chandra high-energy

transmission grating: Design, fabrication, ground calibration, and 5 years in flight. *Publications of the Astronomical Society of the Pacific*, 117(836):1144–1171, 2005.

[20] Thomas H. Markert, Claude R. Canizares, Daniel Dewey, Michael McGuirk, Chris S. Pak, and Mark L. Schattenburg. High-energy transmission grating spectrometer for the advanced x-ray astrophysics facility (axaf). volume 2280, pages 168–180. SPIE, 1994.

[21] P. J. Serlemitsos, Y. Soong, K.-W. Chan, T. Okajima, J. P. Lehan, Y. Maeda, K. Itoh, H. Mori, R. Iizuka, A. Itoh, H. Inoue, S. Okada, Y. Yokoyama, Y. Itoh, M. Ebara, R. Nakamura, K. Suzuki, M. Ishida, A. Hayakawa, C. Inoue, S. Okuma, R. Kubota, M. Suzuki, T. Osawa, K. Yamashita, H. Kunieda, Y. Tawara, Y. Ogasaka, A. Furuzawa, K. Tamura, R. Shibata, Y. Haba, M. Naitou, and K. Misaki. The X-Ray Telescope onboard Suzaku. *Publ. Astron. Soc. Japan*, 59:9–21, January 2007.

[22] R. L. Kelley. X-ray microcalorimeters for Astro-E2 and high-energy astrophysics. *Nuclear Instruments and Methods in Physics Research A*, 559:341–344, April 2006.

[23] `http://imagine.gsfc.nasa.gov/docs/sats_n_data/xray_missions.html`.

[24] Carl Gang Chen. *Beam alignment and image metrology for scanning beam interference lithography : fabricating gratings with nanometer phase accuracy.* PhD thesis, Massachusetts Institute of Technology, Cambridge, Massachusetts, June 2003.

[25] Paul Thomas Konkola. *Design and analysis of a scanning beam interference lithography system for patterning gratings with nanometer-level distortions.* PhD thesis, Massachusetts Institute of Technology, Cambridge, Massachusetts, June 2003.

[26] Chih-Hao Chang. *Multilevel interference lithography-fabricating sub-wavelength periodic nanostructures.* PhD thesis, Massachusetts Institute of Technology, Cambridge, Massachusetts, September 2008.

[27] Chih-Hao Chang, Y. Zhao, R. K. Heilmann, and M. L. Schattenburg. Fabrication of 50 nm period gratings with multilevel interference lithography. *Opt. Lett.*, 33(14):1572–1574, 2008.

[28] Marc J. Madou. *Fundamentals of Microfabrication: The Science of Miniaturization.* CRC Press, 2nd edition, 2002.

[29] K. Biswas and S. Kal. Etch characteristics of koh, tmah and dual doped tmah for bulk micromachining of silicon. *Microelectronics Journal*, 37(6):519–525, 2006.

[30] Mitsuhiro Shikida, Kazuo Sato, Kenji Tokoro, and Daisuke Uchikawa. Differences in anisotropic etching properties of koh and tmah solutions. *Sensors and Actuators A: Physical*, 80(2):179–188, 2000.

[31] J. Laconte, D. Flandre, and J.-P. Raskin. *Micromachined Thin-Film Sensors for SOI-CMOS Co-Integration.* Springer, 2006.

[32] D. L. Kendall. Vertical etching of silicon at very high aspect ratios. *Annual Review of Materials Science*, 9(1):373–403, 1979.

[33] Y. Uenishi, M. Tsugai, and M. Mehregany. Micro-opto-mechanical devices fabricated by anisotropic etching of (110) silicon. *Journal of Micromechanics and Microengineering*, 5(4):305, 1995.

[34] P. Krause, E. Obermeier, and W. Wehl. A micromachined single-chip inkjet printhead. *Sensors and Actuators A: Physical*, 53(1-3):405–409, 1996.

[35] Yuichiro Ezoe, Masaki Koshiishi, Makoto Mita, Kazuhisa Mitsuda, Akio Hoshino, Yoshitaka Ishisaki, Zhen Yang, Takayuki Takano, and Ryutaro Maeda.

Micropore x-ray optics using anisotropic wet etching of (110) silicon wafers. *Appl. Opt.*, 45(35):8932–8938, 2006.

[36] Minseung Ahn, Ralf K. Heilmann, and Mark L. Schattenburg. Fabrication of ultrahigh aspect ratio freestanding gratings on silicon-on-insulator wafers. *Journal of Vacuum Science and Technology B: Microelectronics and Nanometer Structures*, 25(6):2593–2597, 2007.

[37] H. Seidel, L. Csepregi, A. Heuberger, and H. Baumgartel. Anisotropic etching of crystalline silicon in alkaline solutions. *Journal of the Electrochemical Society*, 137(11):3626–3632, 1990.

[38] M. Elwenspoek. On the mechanism of anisotropic etching of silicon. *Journal of The Electrochemical Society*, 140(7):2075–2080, 1993.

[39] Alexander Hölke and H.T. Henderson. Ultra-deep anisotropic etching of (110) silicon. *Journal of Micromechanics and Microengineering*, 9:51–57(7), 1999.

[40] Kazuo Sato, Mitsuhiro Shikida, Yoshihiro Matsushima, Takashi Yamashiro, Kazuo Asaumi, Yasuroh Iriye, and Masaharu Yamamoto. Characterization of orientation-dependent etching properties of single-crystal silicon: effects of koh concentration. *Sensors and Actuators A: Physical*, 64(1):87–93, 1998.

[41] P. Krause and E. Obermeier. Etch rate and surface roughness of deep narrow u-grooves in (110)-oriented silicon. *Journal of Micromechanics and Microengineering*, 5(2):112, 1995.

[42] M. G. Moharam, Drew A. Pommet, Eric B. Grann, and T. K. Gaylord. Stable implementation of the rigorous coupled-wave analysis for surface-relief gratings: enhanced transmittance matrix approach. *J. Opt. Soc. Am. A*, 12(5):1077–1086, 1995.

[43] `http://www.gsolver.com`.

[44] David Attwood. *Soft X-rays and Extream Ultraviolet Radiation: Principles and Applications.* Cambridge University Press, 1st edition, 1999.

[45] Microcomb fabrication for high accuracy foil x-ray telescope assembly and vector gaussian beam modeling. Master's thesis, Massachusetts Institute of Technology, Cambridge, Massachusetts, June 2000.

[46] Max Born and Emil Wolf. *Principles of Optics.* Pergamon Press, 5th edition, 1975.

[47] Francis A. Jenkins and Harvey E. White. *Fundamentals of Optics.* McGraw-Hill, 4th edition, 1976.

[48] Eugene Hecht. *Optics.* Addison Wesley, 4th edition, 2002.

[49] B. L. Henke, E. M. Gullikson, and J. C. Davis. X-ray interactions: Photoabsorption, scattering, transmission, and reflection at e = 50-30,000 ev, z = 1-92. *Atomic Data and Nuclear Data Tables*, 54(2):181–342, 1993.

[50] Michael Ashby. *Materials selection in mechanical design.* Butterworth-Heinemann, 3rd edition, 2005.

[51] A. A. Ayon, R. Braff, C. C. Lin, H. H. Sawin, and M. A. Schmidt. Characterization of a time multiplexed inductively coupled plasma etcher. *Journal of The Electrochemical Society*, 146(1):339–349, 1999.

[52] Yanxia Sun, Ralf K. Heilmann, Carl G. Chen, Craig R. Forest, and Mark L. Schattenburg. Precision microcomb design and fabrication for x-ray optics assembly. *Journal of Vacuum Science and Technology B: Microelectronics and Nanometer Structures*, 21(6):2970–2974, 2003.

[53] Chih-Hao Chang, R. K. Heilmann, R. C. Fleming, J. Carter, E. Murphy, M. L. Schattenburg, T. C. Bailey, J. G. Ekerdt, R. D. Frankel, and R. Voisin. Fabrication of sawtooth diffraction gratings using nanoimprint lithography. *Journal of*

*Vacuum Science and Technology B: Microelectronics and Nanometer Structures*, 21(6):2755–2759, 2003.

[54] Paul T. Konkola, Carl G. Chen, Ralf K. Heilmann, Chulmin Joo, Juan C. Montoya, Chih-Hao Chang, and Mark L. Schattenburg. Nanometer-level repeatable metrology using the nanoruler. *Journal of Vacuum Science and Technology B: Microelectronics and Nanometer Structures*, 21(6):3097–3101, 2003.

[55] R. K. Heilmann, C. G. Chen, P. T. Konkola, and M. L. Schattenburg. Dimensional metrology for nanometre-scale science and engineering: towards sub-nanometre accurate encoders. *Nanotechnology*, 15(10):S504–S511.

[56] G. Kaminsky. Micromachining of silicon mechanical structures. *Journal of Vacuum Science and Technology B: Microelectronics and Nanometer Structures*, 3(4):1015–1024, 1985.

[57] Seong-Hyok Kim, Sang-Hun Lee, Hyung-Taek Lim, Yong-Kweon Kim, and Seung-Ki Lee. (110) silicon etching for high aspect ratio comb structures. In *Sixth International Connference on Emerging Technologies and Factory Automation Proceedings*, pages 248–252, ,CA,USA, 1997. IEEE.

[58] Chii-Rong Yang, Po-Ying Chen, Yuang-Cherng Chiou, and Rong-Tsong Lee. Effects of mechanical agitation and surfactant additive on silicon anisotropic etching in alkaline koh solution. *Sensors and Actuators A: Physical*, 119(1):263–270, 2005.

[59] Chih-Hao Chang. Fabrication of extremely smooth blazed diffraction gratings. Master's thesis, Massachusetts Institute of Technology, Cambridge, Massachusetts, June 2004.

[60] D. L. Kendall and G. R. de Guel. Orientations of the third kind: the coming of age of (110) silicon. In Clifford D. Fung, Peter W. Cheung, Wen H. Ko, and David G. Fleming, editors, *Micromachining and micropackaging of transducers*, chapter 3, pages 107–124. Elsevier Science Publishers, 1985.

[61] V. K. Dwivedi, R. Gopal, and S. Ahmad. Fabrication of very smooth walls and bottoms of silicon microchannels for heat dissipation of semiconductor devices. *Microelectronics Journal*, 31(6):405–410, 2000.

[62] Simon P. Garcia, Hailing Bao, and Melissa A. Hines. Etchant anisotropy controls the step bunching instability in koh etching of silicon. *Phys. Rev. Lett.*, 93(16):166102, Oct 2004.

[63] Chii-Rong Yang, Cheng-Hao Yang, and Po-Ying Chen. Study on anisotropic silicon etching characteristics in various surfactant-added tetramethyl ammonium hydroxide water solutions. *Journal of Micromechanics and Microengineering*, 15(11):2028–2037, 2005.

[64] Theo Baum and David J Schiffrin. Afm study of surface finish improvement by ultrasound in the anisotropic etching of si in koh for micromachining applications. *Journal of Micromechanics and Microengineering*, 7(4):338–342, 1997.

[65] D. Nüsse, M. Hoffmann, and E. Voges. Megasonic enhanced KOH etching for {110} silicon bulk micromachining. In K. S. Moon, editor, *Society of Photo-Optical Instrumentation Engineers (SPIE) Conference Series*, volume 5602 of *Presented at the Society of Photo-Optical Instrumentation Engineers (SPIE) Conference*, pages 27–34, September 2004.

[66] Thomas Young. An essay on the cohesion of fluids. *Philosophical Transactions of the Royal Society of London (1776-1886)*, 95(-1):65–87, 1805. 10.1098/rstl.1805.0005.

[67] Arthur W. Adamson and Alice P. Gast. *Physical chemistry of surfaces.* Wiley-Interscience publication, 6th edition, 1997.

[68] I. Zubel and M. Kramkowska. Etch rates and morphology of silicon (h k l) surfaces etched in koh and koh saturated with isopropanol solutions. *Sensors and Actuators A: Physical*, 115(2-3):549–556, 2004.

[69] Jing Chen, Litian Liu, Zhijian Li, Zhimin Tan, Qianshao Jiang, Huajun Fang, Yang Xu, and Yanxiang Liu. Study of anisotropic etching of (1 0 0) si with ultrasonic agitation. *Sensors and Actuators A: Physical*, 96(2-3):152–156, 2002.

[70] C.H. Mastrangelo and C.H. Hsu. Mechanical stability and adhesion of microstructures under capillary forces. i. basic theory. *Microelectromechanical Systems, Journal of*, 2(1):33–43, Mar 1993.

[71] C.H. Mastrangelo and C.H. Hsu. Mechanical stability and adhesion of microstructures under capillary forces. ii. experiments. *Microelectromechanical Systems, Journal of*, 2(1):44–55, Mar 1993.

[72] Toshihiko Tanaka, Mitsuaki Morigami, and Nobufumi Atoda. Mechanism of resist pattern collapse during development process. *Japanese Journal of Applied Physics*, 32(Part 1, No. 12B):6059–6064, 1993.

[73] Hideo Namatsu, Kenji Kurihara, Masao Nagase, Kazumi Iwadate, and Katsumi Murase. Dimensional limitations of silicon nanolines resulting from pattern distortion due to surface tension of rinse water. *Applied Physics Letters*, 66(20):2655–2657, 1995.

[74] Yoshio Yamashita. Sub-1 $\mu$m patterning with high aspect ratio of 5 achieved by preventing pattern collapse. *Japanese Journal of Applied Physics*, 35(Part 1, No. 4A):2385–2386, 1996.

[75] Mark Robertson-Tessi, Robert J. Wild, Alexander D. Cronin, and Tim Savas. Cleaning silicon nitride gratings with liquid immersion. *Journal of Vacuum Science and Technology B:Microelectronics and Nanometer Structures*, 24(3):1409–1412, 2006.

[76] Stephen D. Senturia. *Microsystem design.* Springer, 2nd edition, 2004.

[77] Youngjoo Yee, Kukjin Chun, and Jong Duk Lee. Polysilicon surface modification technique to reduce sticking of microstructures. *Solid-State Sensors and*

*Actuators, 1995 and Eurosensors IX.. Transducers '95. The 8th International Conference on*, 1:206–209, Jun 1995.

[78] P.F. Man, B.P. Gogoi, and C.H. Mastrangelo. Elimination of post-release adhesion in microstructures using conformal fluorocarbon coatings. *Microelectromechanical Systems, Journal of*, 6(1):25–34, Mar 1997.

[79] Roya Maboudian, W. Robert Ashurst, and Carlo Carraro. Self-assembled monolayers as anti-stiction coatings for mems: characteristics and recent developments. *Sensors and Actuators A: Physical*, 82(1-3):219 – 223, 2000.

[80] N. Takeshima, K.J. Gabriel, M. Ozaki, J. Takahashi, H. Horiguchi, and H. Fujita. Electrostatic parallelogram actuators. *Solid-State Sensors and Actuators, 1991. Digest of Technical Papers, TRANSDUCERS '91., 1991 International Conference on*, pages 63–66, Jun 1991.

[81] Dai Kobayashi, Chang-Jin Kim, and Hiroyuki Fujita. Photoresist-assisted release of movable microstructures. *Japanese Journal of Applied Physics*, 32(Part 2, No. 11A):L1642–L1644, 1993.

[82] E. Kobeda and E. A. Irene. A measurement of intrinsic sio[sub 2] film stress resulting from low temperature thermal oxidation of si. *Journal of Vacuum Science and Technology B: Microelectronics and Nanometer Structures*, 4(3):720–722, 1986.

[83] E. Kobeda and E. A. Irene. Sio[sub 2] film stress distribution during thermal oxidation of si. *Journal of Vacuum Science and Technology B: Microelectronics and Nanometer Structures*, 6(2):574–578, 1988.

[84] Yamato Fukuta, Hiroyuki Fujita, and Hiroshi Toshiyoshi. Vapor hydrofluoric acid sacrificial release technique for micro electro mechanical systems using labware. *Japanese Journal of Applied Physics*, 42(Part 1, No. 6A):3690–3694, 2003.

[85] Stephen H. Crandall, Norman C. Dahl, and Thomas J. Lardner. *An introduction to the mechanics of solids.* McGRAW-HILL, 2nd edition, 1978.

[86] Warren C. Young and Richard G. Budynas. *Roark's formulas for stress and strain.* McGRAW-HILL, 7th edition, 2002.

[87] `http://www.comsol.com`.

[88] A Szekeres and P Danesh. Mechanical stress in structures formed by thermal oxidation of amorphous and crystalline silicon. *Semiconductor Science and Technology*, 11(8):1225–1230, 1996.

[89] Pran Mukherjee, Myung-Gyu Kang, Thomas H. Zurbuchen, L. Jay Guo, and Fred A. Herrero. Fabrication of high aspect ratio si nanogratings with smooth sidewalls for a deep uv-blocking particle filter. *Journal of Vacuum Science and Technology B: Microelectronics and Nanometer Structures*, 25(6):2645–2648, 2007.

[90] R Agarwal, S Samson, and S Bhansali. Fabrication of vertical mirrors using plasma etch and koh:ipa polishing. *Journal of Micromechanics and Microengineering*, 17(1):26–35, 2007.

[91] Keith J Morton, Gregory Nieberg, Shufeng Bai, and Stephen Y Chou. Wafer-scale patterning of sub-40 nm diameter and high aspect ratio (>50:1) silicon pillar arrays by nanoimprint and etching. *Nanotechnology*, 19(34):345301 (6pp), 2008.

[92] John C. Wolfe, Sandeep V. Pendharkar, Paul Ruchhoeft, Sudipto Sen, Mark D. Morgan, W. E. Horne, R. C. Tiberio, and John N. Randall. A proximity ion beam lithography process for high density nanostructures. *Journal of Vacuum Science and Technology B: Microelectronics and Nanometer Structures*, 14(6):3896–3899, 1996.

[93] C.C. Welch, A.L. Goodyear, T. Wahlbrink, M.C. Lemme, and T. Mollenhauer. Silicon etch process options for micro- and nanotechnology using in-

ductively coupled plasmas. *Microelectronic Engineering*, 83(4-9):1170 – 1173, 2006. Micro- and Nano-Engineering MNE 2005.

[94] Y. F. Chang, Q. R. Chou, J. Y. Lin, and C. H. Lee. Fabrication of high-aspect-ratio silicon nanopillar arrays with the conventional reactive ion etching technique. *Applied Physics A: Materials Science and Processing*, 86(2):193–196, 2007. 10.1007/s00339-006-3748-0.

[95] C. C. Cheng, K. V. Guinn, I. P. Herman, and V. M. Donnelly. Competitive halogenation of silicon surfaces in $HBr/Cl_2$ plasmas studied with x-ray photoelectron spectroscopy and in situ, real-time, pulsed laser-induced thermal desorption. *Journal of Vacuum Science and Technology A: Vacuum, Surfaces, and Films*, 13(4):1970–1976, 1995.

[96] M. L. Schattenburg, R. J. Aucoin, and R. C. Fleming. Optically matched trilevel resist process for nanostructure fabrication. *Journal of Vacuum Science and Technology B: Microelectronics and Nanometer Structures*, 13(6):3007–3011, 1995.

[97] James D. Plummer, Michael Deal, and Peter B. Griffin. *Silicon VLSI technology : fundamentals, practice and modeling.* Prentice Hall, Upper Saddle River, NJ, 2000.

[98] Ralf Heilmann, Minseung Ahn, and Mark Schattenburg. Critical angle transmission gratings for the international x-ray observatory. Con-X/IXO Facility Science Team Meeting, NASA GSFC, Greenbenlt, MD, Aug. 2008.

[99] `http://www.orbital.com/NewsInfo/Publications/peg-user-guide.pdf`. Pegasus user's guide.

[100] James H. Williams. *Fundamentals of applied dynamics.* J. Wiley, New York, 1996.

[101] Peter W. Fortescue, John Stark, and Graham Swinerd. *Spacecraft systems engineering.* J. Wiley, Chichester, England ; Hoboken, NJ, 3 edition, 2003.